Faculty of Applied Sciences

Detailed efficiency characterisation of $Lu_2O_3:Eu^{3+}$ thin film luminescent solar concentrators: an analytic and experimental light transport study

by

Jan Willem E. Wiegman
1266918

Master Thesis Project, Applied Physics
January 2012

Delft University of Technology
Department of RRR – Radiation detection and Medical imaging

Supervising tutor: dr. E. van der Kolk
Second reviewer: Prof.dr. P. Dorenbos
Third reviewer: dr.ir. M. Wagemaker

Detailed efficiency characterisation of Lu_2O_3:Eu^{3+} thin film luminescent solar concentrators: an analytic and experimental light transport study

Master thesis project

J.W.E. Wiegman

January 2012

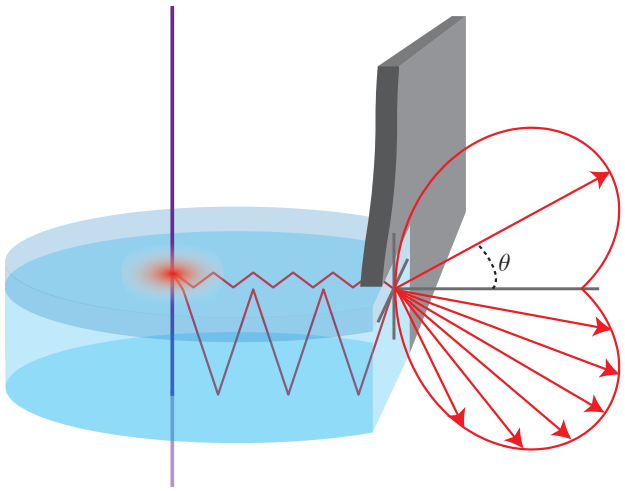

Delft University of Technology
Faculty of Applied Sciences
R^3 – Radiation Detection and Medical Imaging
Supervised by dr. E. van der Kolk

TU Delft Delft University of Technology

Abstract

The worldwide struggle to renew the human energy supply to high environmental friendly standards has led to creative and innovative solutions for the supply of 'green' energy. The financial benefits of conventional energy sources restrain the widespread use of renewable energy sources, like wind or solar energy. This competition requires ingenuity and sometimes the reinvestigation of possibly prematurely dismissed solutions, such as the luminescent solar concentrator (LSC).

In this research an inorganic thin film LSC is characterized experimentally in detail in terms of all the separate light transport steps that result in the concentration of sunlight. A 3 μm thin film of Eu^{3+} doped Lu_2O_3 was chosen for of its large Stokes' shift, which excludes all transport losses due to self-absorption and allowed to study losses caused by scattering at interfaces of the LSC.

A model is presented which can be used to calculate the LSC light transport efficiency as a function of LSC surface area. This model needs the easily measured linear attenuation as input, which characterizes the transport efficiency. A second more elaborate analytic model is developed to separate the losses in the film and in the substrate. This model also considers the non-uniformity of the attenuation length.

The quantum efficiencies of our LSCs following from the measurements are in the order of 15%, which is less than ideal, mainly due to a poor $34 - 44\%$ luminescence quantum efficiency and a $53 - 65\%$ waveguide efficiency.

Measurements have shown some discrepancies. Both the absorption spectrum and the time resolved luminescence spectrum did not show the expected behaviour upon change of europium concentration. The directional output measurements did not show the expected relative intensities of the film and the substrate. Qualitatively, however, the model and measurements are similar. Complimentary measurements could reveal the causes of these quantitative differences. A possible reason could be that some waveguide modes are not supported by the film.

The modelling reveals that, in order to have building integrated LSCs simultaneously acting as windows, the linear attenuation length in the LSC should be longer than one meter. This is in contrast to the values in the order of tens of millimetres, which have been measured for the LSCs in this work.

If such attenuation lengths are realised, power efficiency calculations reveal power efficiencies of up to 16% for the appropriate combination of luminescent material and solar cell.

Contents

Chapter 1

Introduction

One of the big aims in photovoltaic (PV) research is to make photovoltaic energy competitive in prize with conventional energy resources. Beside making the PV-cells more efficient, there is a second option, namely concentration of the sunlight onto the PV-cells. This decreases the surface area solar cell needed, which in turn lowers the costs of a PV-module.

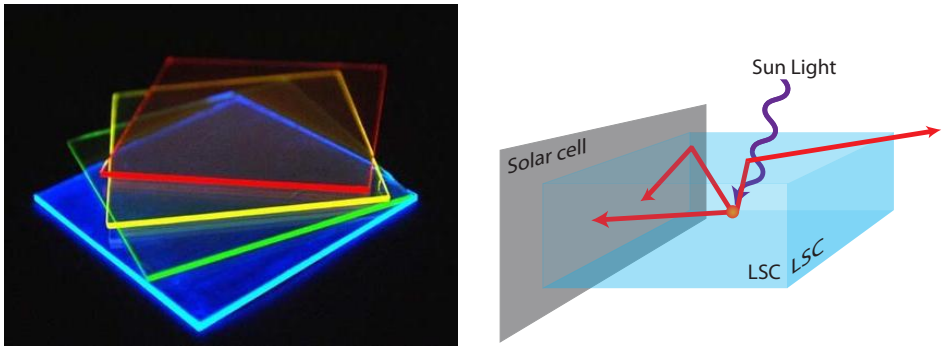

(a) (b)

Figure 1.1: (a) [1] shows some differently coloured LSCs, with the bright concentrated light at the outcoupling surface. (b) shows schematically the working of an LSC. The sun light (purple) is absorbed by a luminescent centre. The centre emits the red light isotropically, of which a substantial part is guided towards the solar cells at the perimeter.

This work is all about luminescent solar concentrators (LSCs), of which a few are shown in figure 1.1(a). LSCs concentrate solar light by means of luminescence, hence their name.

Luminescent solar concentrators, date back from the 1970s [2, 3]. LSCs are a very attractive concept for a concentrating PV-module for numerous reasons: low cost production opportunities, the LSC can operate in diffuse light, therefore not needing expensive solar tracking devises, and finally, due to the luminescence, only light matched to the solar cell's bandgap will be collected by the PV-cells, resulting in higher PV efficiencies. In recent years there has been a renewed interest in LSCs due to the urgency of development of sustainable technology combined with new ideas on light trapping and new

photostable luminescent (nano) materials and dye molecules with broader absorption and less self-absorption. [4–7]

In general LSCs consist of a slab of dielectric material containing a luminescent material (organic dyes, quantum dots, or Rare-earth complexes), with PV-cells connected to the perimeter of the slab. The luminescent centres absorb the sunlight incident on the face of the LSC, and isotropically emit light at a slightly lower energy. The major part of the emitted light is trapped inside the slab, and is guided to the solar cells at the perimeter, see figure 1.1(b).

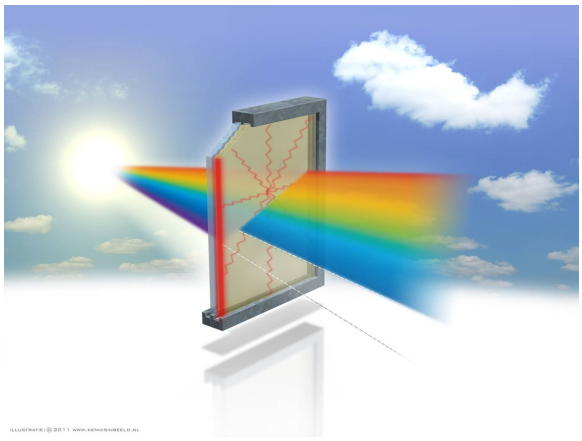

Figure 1.2: Artist impression of a building integrated LSC, absorbing the UV-spectrum and emitting in the red. The window is still transparent for the visible light.

Two main types of LSC can be identified. The first is the single plate concentrator, in which the luminescent centres are homogeneously distributed throughout the plate. The second type, which is considered in this paper, is the thin film LSC. Such LSC consists of an optically passive glass- or polymer-based substrate coated with one or more luminescent layers.

Though the concept of LSCs is very promising, problems like photo-degradation [8–10], limited spectral sensitivity [11], or self-absorption losses [12], have so far prevented large scale use of LSCs.

All problems have been addressed individually, like Wu et al. [13], who reported rare earth complexes showing absorption in de VIS-spectrum and IR emission with zero self-absorption loss. Earp et al. [14] reported in 2004 an LSC with a light transport half-length of 1.2 m (corresponding to a waveguide attenuation length of about 1.7 m). Kennedy et al. [15] presented an LSC based on quantum dots, overcoming the problem of photo stability at the cost of lower luminescent quantum yield. Such limitations of the total LSC PV-module cause the application of LSCs to still remain a castle in the air.

An interesting application would be building integrated (BI) LSCs [16], in which the windows of e.g. office buildings are coated with an UV absorbing luminescent thin film, and can therefore act as (additional) power supplies for such buildings. As office buildings often have shaded glass, par-

tial absorption in the visible part of the solar spectrum would be acceptable as well, yielding better usage of the available sunlight and increasing feasibility of the BI LSC, of which an artist impression is shown in figure 1.2.

In the first part of this work the basics of the theory of luminescence is explained, section 2.1 covers in short energy levels , phonons, various types of luminescent materials and selection rules. In section 2.2 the principles behind two layer LSCs are explained, mainly covering the theory of waveguiding in planar waveguides. Next, in section 2.3 all loss processes concerning LSCs are treated. As this is of most importance for this research, this section is quite elaborate. It is in this section that two complementary light transport models are presented, allowing for the calculation of the light transport efficiency.

In the next chapter, chapter 3, the experimental approach is written down, following the order of the losses described before. This chapter is followed by chapter 4, in which the production processes and treatments of the samples and their physical properties are discussed. Chapter 5 shows, again in the order of section 2.3, the results of the different measurements. The results of chapter 5 are discussed in the context of building integrated application in chapter 6, revealing necessary followup experiments, given in chapter 7.

Chapter 2

Theory

In this chapter three main topics will be covered. First, in section 2.1, the basics of luminescence are explained, which is an essential part of luminescent solar concentrators (LSC). Second, in section 2.2, the principles of a two layer LSC are covered. Last, in section 2.3, all limiting contributions to the efficiency of the LSC are explained. With these contributions an estimation is made of the achievable power efficiencies of LSCs.

2.1 Luminescence

Luminescence is the emission of light by a material, which is not caused by its temperature. There are many types of luminescence, e.g. chemiluminescence, electroluminescence, or photoluminescence. In these types the luminescence is due to energy freed by respectively a chemical reaction, an electric potential or absorbed photons.

The last, photoluminescence, is the luminescence a luminescent solar concentrator works with. Photoluminescence can be divided into two subcatagories, i.e. fluorescence and phosphorescence. The difference between these two is mainly the decay time. Fluorescent light is emitted almost instantly after absorption, whereas phosphorescent light is radiated significantly after illumination. The reason behind this is that phosphorescence is caused by spin-forbidden transitions, and fluorescence is caused by spin-allowed transitions [17]. In this work, however, I will not use this distinction, and will refer to it by the general name luminescence.

For a good understanding of luminescence one should know the basic physics behind the atomic structure. One of the first useful descriptions of the atom was a positively charged nucleus build out of protons surrounded by negatively charged electrons. This system was described as a linear harmonic oscillator (HO). [18] The harmonic oscillator can be described by its electric dipole moment with a characteristic angular frequency ω_0. The higher the frequency the higher the energy of the harmonic oscillator. As light is an electromagnetic wave it interacts with this oscillating charge. It can in fact be absorbed by the HO, upon excitation of the HO to a higher energy. In a similar way this harmonic oscillator can emit radiation at an energy decay

rate of A_0, given by equation 2.1.

$$A_0 = \frac{e^2\omega_0^2}{6\pi\epsilon_0 m_e c^3} \tag{2.1}$$

In this equation e is the electron charge, ϵ_0 the permittivity of vacuum, m_e the electron mass and c the speed of light.

One of the biggest problems is that in this atomic model the atom loses more and more energy, until finally the electron is no longer oscillating. This was solved by the introduction by Bohr of the quantized model, which stated that the electrons are allowed to be in a discrete set of orbitals only. The addition of Pauli's exclusion principle prevents from all electrons being in the same lowest energy orbital, as electrons are Fermions and no two Fermions can be together in the exact same state.

Figure 2.1 schematically shows a few energy levels of a three electron atom. The electrons are depicted as an upward or a downward black arrow, respectively spin up or down. In the left picture the atom is in its ground state, i.e. all electrons are in the lowest possible energy level. The electron in the 2s level cannot go to the 1s level, because that level is already occupied and Pauli's exclusion principle dictates that at most one electron is in one particular state. If a photon with energy equal to the energy difference 2p-2s is incident, the atom can be excited, i.e. the electron is transferred from the 2s level to the higher energy 2p level. As nature strives for the lowest energy occupation, i.e. the ground state, the electron will fall back to its original state under emission of a photon again with energy 2p-2s, see the rightmost picture in figure 2.1. This shows roughly one luminescent cycle of absorption and emission.

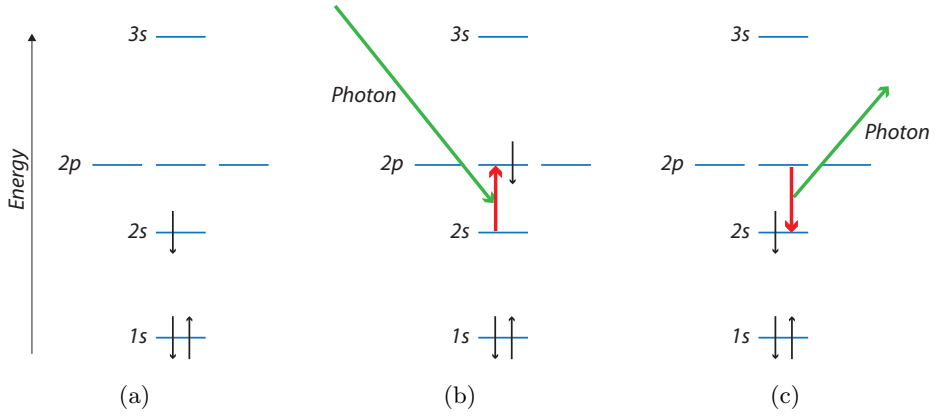

Figure 2.1: Schematic drawing of a three electron atom. The electrons are depicted as black arrows, upward for spin up and downward for spin down. (a) the atom is in its ground state, i.e. all electrons occupy the lowest possible states. (b) the atom is excited under absorption of a photon. (c) The atom relaxes under emission of a photon.

The moment of emission of the photon is determined by the radiative lifetime, τ_{rad}, which is related to Einstein's equation [18] for the rate of

spontaneous emission A_{mn}, between states m and n: [19]

$$A_{mn} = \frac{\omega_{mn}^3}{3\pi\epsilon_0\hbar c^3} \mid M_{mn} \mid^2 \tag{2.2}$$

M_{mn} is the mechanical dipole moment, containing terms related to the electrical dipole, the magnetic dipole and higher order perturbations like the electric quadrupole.

In reality the excited state m relaxes to several states n, resulting in a radiative lifetime according equation 2.3. [19]

$$\tau_{rad} = \frac{1}{\sum_n A_{mn}} \tag{2.3}$$

Next to Einstein's equation for the rate of spontaneous emission exists a second Einstein equation describing the transition probability for absorption. [18]

2.1.1 Phonons

So far atoms were treated as if they were on their own. In reality they are often part of a crystal lattice. In the lattice the atoms feel each others presence. One way of describing this interaction is to consider them connected to each other by springs. [20, 21] Now one can imagine these atoms do not stand still, but are vibrating. Due to the interconnections between the atoms these vibrations behave like waves in the lattice. These lattice waves are called phonons.

Considering a 1-D chain of atoms connected by Hookean springs with periodic boundary conditions, one can fairly easy derive the dispersion relation for this chain, equation 2.4.

$$\omega^2 M = 4K \sin^2(\frac{1}{2}ka) \tag{2.4}$$

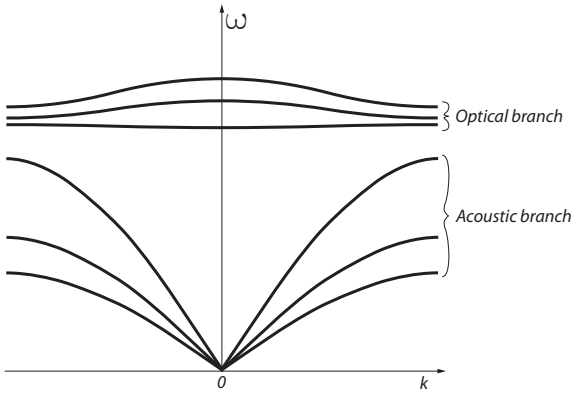

Figure 2.2: Dispersion relation of a three dimensional crystal with two different atoms, leading to an acoustic and an optical branch divided into three levels.

In this equation ω is the angular frequency, M is the mass of the atoms, K is the spring constant connecting the atoms, k is the wave number and a is the distance between two atoms in equilibrium. Equation 2.4 dictates which angular frequencies are allowed inside the crystal. Though this is a very simplified model, after all it is a 1-D chain with only one type of atoms, it gives a insight in the behaviour of bulk material. The behaviour in 3-D is quite similar; in figure 2.2 the dispersion relation is given for a 3-D crystal with two different atoms. The two types of atom cause a splitting in an optical and an acoustic branch, where as the multi-dimensionality causes the splitting of these branches. The vibrations described by equation 2.4 behave like ordinary harmonic oscillator, and is therefore restricted to the following energies, in which n represents the number of phonon quanta:

$$\epsilon_n = (n + \frac{1}{2})\hbar\omega \tag{2.5}$$

The phonons can act parasitic on the luminescence in the sense that phonon relaxation could be more likely than relaxation by emission of a photon. The phonon relaxation can be understood by the configurational model, which qualitatively describes multiple luminescent characteristics.

2.1.2 Configurational model

[17, 18] A simplified model of luminescence, the configurational model, gives relatively easy insight in a number of luminescent processes, like phonon relaxation and the Stokes' shift[1]. The configurational model considers the luminescent ion connected to its neighbours by Hooke's law, which is quadratic in distance. For both the excited state and the ground state the model has a spring constant, K_e and K_g respectively. In figure 2.3, this quadratic behaviour is shown for both states. One also observes a shift in the equilibrium positions of the ground state and the excited state, Q_0, which is the interatomic distance at the equilibrium of the ground state.

Due to this shift there is a difference in energy between the absorbed photon, dashed arrow $A \rightarrow B$, and the emitted photon, dashed arrow $C \rightarrow D$, the Stokes' shift U_{Stokes}, equation 2.6. One should notice that after excitation, the luminescent centre relaxes by phonon relaxation from point B to point C, causing the actual shift.

$$U_{Stokes} = \frac{1}{2}(K_e + K_g)Q_0^2 \tag{2.6}$$

Next to the Stokes' shift the configurational model explains phonon relaxation from the excited state to the ground state. One observes in figure 2.3 there is overlap between the excited state and the ground state, point E. From this point multiple phonon quanta can be emitted to bring the electron from the excited to the ground state. So if the atom is excited, thermal energy can cause the electron to reach point E, whereupon it makes

[1] the Stokes' shift is the difference in energy between the absorbed and emitted photons.

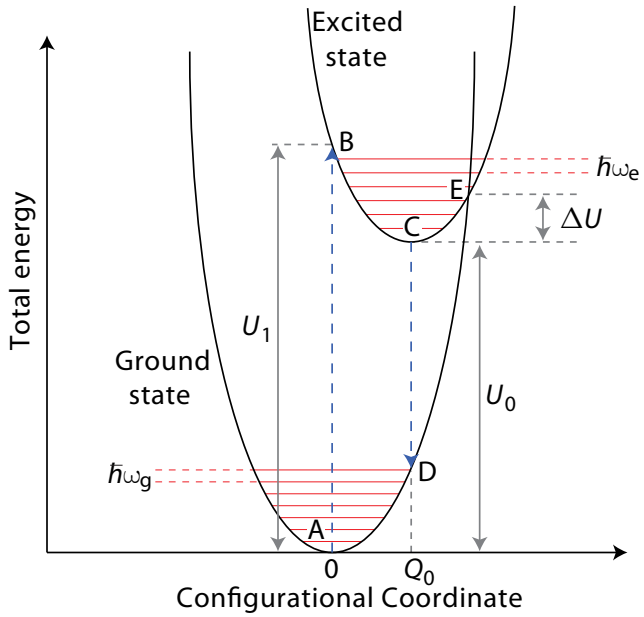

Figure 2.3: [17, 18] **Schematic representation of the configurational model. Dashed arrows represent excitation under absorption or relaxation under emission of a photon. The horizontal lines represent quantized phonon energies, $\hbar\omega$. The excited state is shifted to Q_0 in comparison to the ground state, causing the Stokes' shift.**

the transition to the ground state without emission of a photon. This will occur with a transition probability per unit time N, given by equation 2.7.

$$N = s \exp \frac{-\Delta U}{kT} \tag{2.7}$$

s is a product of the transition probability between the ground and excited states and a frequency with which the excited state reaches the intersection E. This quantity s can be treated as a constant, since it is only weakly dependent on temperature. It is called the frequency factor and is typically of the order of 10^{13} s^{-1}.

If the luminescence probability is defined W, related to the Einstein coefficient A, equation 2.2, an expression for the luminescence efficiency can be derived:

$$\begin{aligned} \eta &= \frac{W}{W+N} \\ &= \left[1 + \frac{s}{W} \exp \frac{-\Delta U}{kT}\right]^{-1} \end{aligned} \tag{2.8}$$

From this equation it is seen that the luminescence is quenched only if the thermal energy is in the order of ΔU.

2.1.3 Types of luminescent materials in relation to LSCs

Basically there exist two types of luminescent materials: organic and inorganic. The major inorganic luminescent materials are the quantum dots (QD's) and Rare-earth (RE) based luminescents. All types have their own benefits and and drawbacks, making none of them the ideal LSC candidate. The four main requirements [22] for good LSC performance are:

1. absorption of all wavelengths smaller than 950 nm and emission at about $1,000$ nm, as silicon solar cells have their optimum at $1,100$ nm.
2. minimum reabsorption losses due to overlap between emission and absorption.
3. luminescent quantum efficiency (LQE) approaching unity, i.e. every absorbed photon should result in an emitted photon.
4. Long-term stability, in the order of decades, to assure an equal lifetime as the solar cells attached.

Organic luminescents, like perylene-based materials, are shown to be stable for long enough periods and have LQE's of near-unity. Problems regard mostly the absorption and emission requirements (1), which are not as required [23]. Besides, organic luminescents exhibit significant reabsorption (2).

QD's, like PbS, show reabsorption, LQE's much smaller than unity and are unstable, [23]. Nevertheless, the absorption and emission of QD's is tunable over a wide range of absorption and emission.

Last, the one this research is based on, RE luminescents are stable, exhibit high LQE's, e.g. reported by Quirino et al. [24] and show minimal reabsorption due to a large Stokes' shift, see section 2.3.5. One should know that mainly inorganic materials are applied on a large scale. The main challenge for RE based materials is to absorb a large part of the solar spectrum. The very narrow and weak absorption peaks due to f-f transitions, see section 2.1.4, cause that only a small part of the sunlight is absorbed, see section 2.3.1. The charge transfer (CT) band on the other hand absorbs over a wide energy spectrum, but most of the time at energies higher than typically available in the sunlight. This CT band energy can be decreased, which is shown by Ten Kate et al. [25].

2.1.4 Rare-earth metals

Rare-earth (RE) metals are widely used for their peculiar luminescent properties. For instance in LEDs, LCD screens, lasers, and in lots of other applications. The reason is twofold; the 4f orbital is only partly filled and is screened from its environment by the filled $5s^2p^6$ orbitals. [17, 19] These screening orbitals prevent the RE atom to strongly interact with any host crystal. The partially filled 4f orbital provides numerous empty energy levels, and therefore even more possible transitions between 4f states. Those transitions are mainly in the visible and infrared part of the spectrum, which

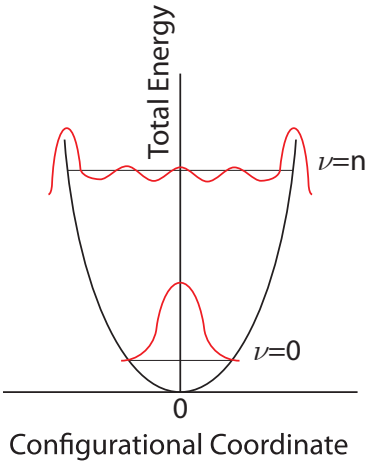

Figure 2.4: [17] Vibrational levels in the configurational model.

explains the optical applications of the rare-earths. Besides the 4f-4f transitions, two other transitions concerning RE metals can cause luminescence, namely charge transfer and 4f↔5d transitions. All three processes are explained in a bit more detail in the following parts.

Charge transfer transition CT transitions are transitions of an electron from the 4f shell to a ligand, often an atom of the host crystal, or vice versa. $4f^n \rightarrow 4f^{n+1}L^{-1}$ or $4f^n \rightarrow 4f^{n-1}L^{+1}$, where L is the ligand. [17, 19] Though both transitions, the ligand-to-metal (LMCT) and the metal-to-ligand (MLCT), are allowed [19], it depends on the energies of the CT transition and the other available transitions whether the CT transitions are observed. The CT transitions occur with associative energies starting from the near-UV region.

4f→5d transitions 4f→ 5d transitions ($4f^n \rightarrow 4f^{n-1}5d$) are not shielded from its environment, thus varying with host crystal. [19] The typical energies associated with these transitions are similar to the energies associated with CT transitions. Though this might need some nuance; in most materials the divalent ions (e.g. Sm^{2+}, Eu^{2+}, Yb^{2+}) show transitions with energies starting in the visible region, whereas the trivalent ions (e.g. Ce^{3+}, Pr^{3+}, Tb^{3+}) have their 4f→ 5d transitions higher in the UV. [17] A final remark is that the energies of both the CT and the 4f→5d strongly depend on the type of host lattice, as these energy levels are not shielded by the $5s^2p^6$ orbitals.

4f-4f transitions The 4f-4f transitions produce narrow and weak absorption peaks compared to the CT and 4f→5d transitions. This can be explained by looking back at the configurational model, section 2.1.2. Q_0 is zero in this case [17]. The lowest energy level of the ground state has a wave function with a maximum amplitude around zero Q. The only energy level in the excited state with its maximum around zero is the lowest energy

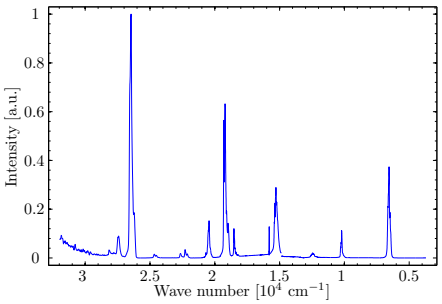

Figure 2.5: Absorption spectrum of $NaLaF_4$:2%Er^{3+} showing the distinctive narrow f-f absorption peaks of Rare-earths. [26]

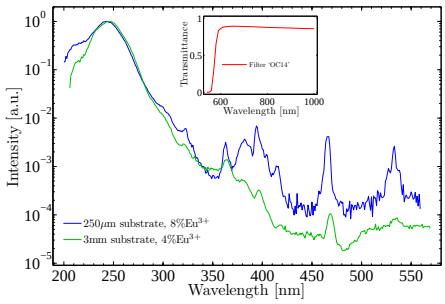

Figure 2.6: Around 250 nm the strong absorbing CT-band of Lu_2O_3:Eu^{3+} is visible. The intensity of for example the $^7F_0 \rightarrow ^5D_2$ transition (466 nm) can be easily compared to the intensity of the CT-band.

level of the excited state. All other states have their maxima off-centered. Such probability wavefunction can be seen in figure 2.4, where the low energy level is located around zero and all higher energy levels off-centered. If Q_0 would be non-zero, overlap would exist with all higher energy levels, as their maxima would shift over the maximum of the low energy level of the ground state. This would result in a broad absorption peak, as the vertical difference between the parabolas changes as function of configurational coordinate, see figure 2.3. The fact that the absorption is weak is due to the parity forbidden character of the 4f-4f transition, which is explained in section 2.1.5. Due to the shielding by the $5s^2p^6$ orbitals, the location of the energy levels is hardly influenced by the host crystal. Dieke has reported the energy levels of the trivalent rare-earths in $LaCl_3$, which is shown in the Dieke diagram, figure 2.7. Due to the shielding by the filled outer electron shells, this diagram stays more or less the same for other host crystals doped with the rare-earths.

2.1.5 Selection rules

As mentioned in the previous section, transitions can be forbidden. Whether a transition is forbidden depends on the selection rules. The two most important are [17], the spin selection rule, and the parity selection rule. The former forbids electronic transitions between two different spin states: $\Delta S \neq 0$. The latter forbids transitions between two states with the same parity, e.g. transitions within the d- or f-shell, or transitions between d- and s-shells. A more detailed explanation of such transitions can be found in references [18] or [27].

The forbidden transitions might still occur; we clearly observed the f-f transitions in the Erbium absorption spectrum, figure 2.5. The symmetry involved with the parity can be broken by the surrounding crystal. If this is the case the forbidden transition can still take place. In the case of the rare-earth ions this effect is small, as the 4f shell is shielded from the

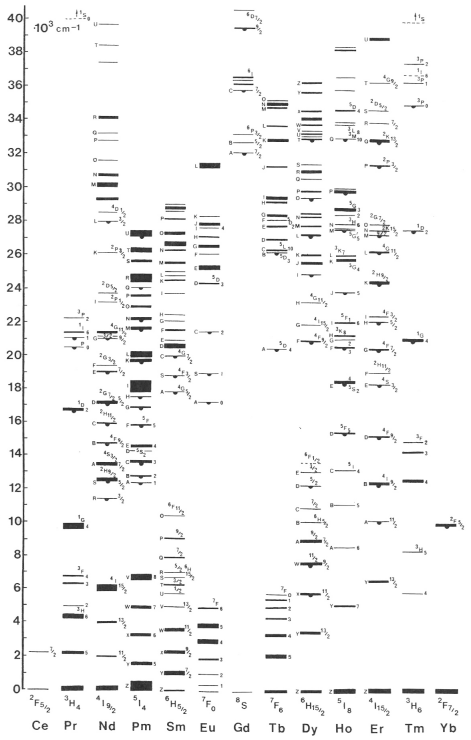

Figure 2.7: Dieke diagram showing the energy levels of the Rare-earth metals in $LaCl_3$.

environment by the outer filled shells. Therefore the absorption is weak at these transitions. An extensive description of such transition, involving Judd-Ovelt theory, can be found in [27]. As we now have a feeling for luminescence (with a focus on RE based luminescence), lets now explore the LSC itself.

2.2 Two layer Luminescent Solar Concentrator

A two layer luminescent solar concentrator (LSC), or previously reported as a planar solar concentrator [28] (PSC), in principle consists of one thin luminescent top layer (the film) and an optically passive thicker sub layer (the substrate). The LSC is designed to collect sunlight from a large area, trap it, and send it to the sides, where it is absorbed by a photovoltaic cell. The workings of such LSC start with the illuminance of the film by for example the sun, the blue arrows in figure 2.8. Part of the incident light is reflected on the top surface (or face), part is transmitted into the film.

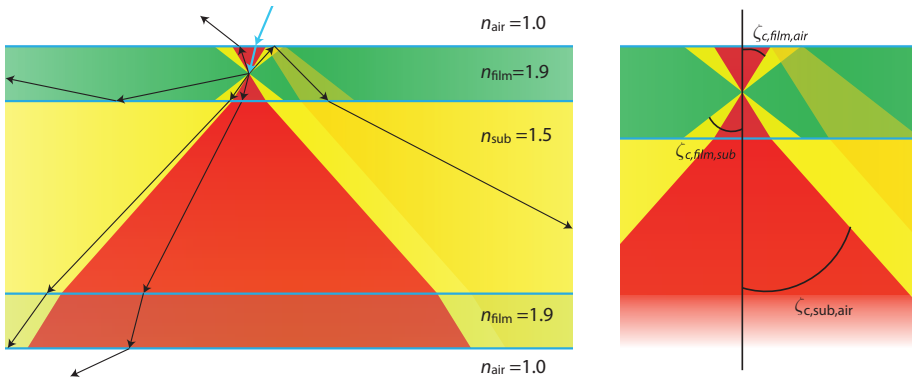

(a) (b)

Figure 2.8: Schematic representation of a two layer LSC. The film represents the luminescent layer, in which a luminescent centre is located at the origin of the cones. For certain angles, emitted photons will escape from the film, as well from the substrate, the red cone. The critical angle for which the photon cannot escape is called $\zeta_{c,film,air}$. For other angles, depicted in yellow, the photons are trapped in the film and substrate combined (the film-substrate-complex). The last part is trapped only in the film, for angles more than $\zeta_{c,film,sub}$.

In this layer, or thin film, the light is absorbed by luminescent centers, which re-emit the light at a longer wavelength, due to the Stokes' shift, as explained in section 2.1.2. The light emitted by the luminescent center is radiated spherically, as the center is assumed to be a point source. Now things get interesting. Due to the fact that the refractive indices of the LSC are higher than its surrounding medium, it is possible to have total internal reflection of the light, see section 2.2.1.1. This means that the light, when incident on the boundary between the LSC and surrounding air, is totally reflected, and therefore is trapped inside the LSC.

2.2.1 Light trapping

Two different cases are possible, first the light is trapped only in the film, second the light is trapped in the combined system of the film and the substrate, the film-substrate-complex, respectively the green parts and the yellow parts in figures 2.8 and 2.9.

Using equation 2.10, one sees that there exists a so called "escape cone" from which the the light can escape the luminescent layer. This is depicted in figure 2.9(a), which is a three dimensional version of figure 2.8. One should notice that the escape cone of the film corresponds, after refraction according Snell's law, equation 2.9, exactly to the escape cone of the substrate, this is not directly obvious, but is derived in Appendix B. This property ensures that for the film there is only one critical angle for both the escape cones, upward and downward.

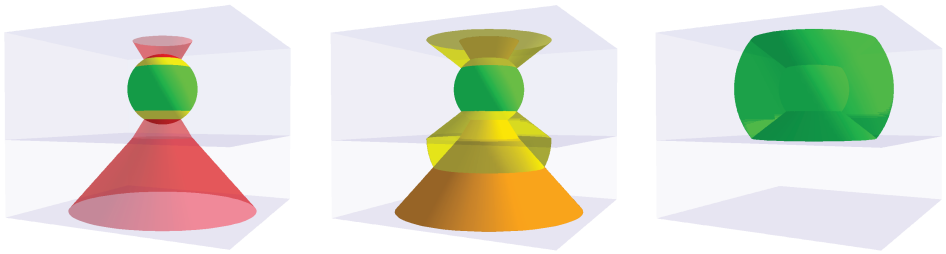

(a) (b) (c)

Figure 2.9: (a) Escape cone of the luminescent layer into the surrounding air. (b) Trapped light in both the film and the substrate. (c) Trapped light only in the film.

The part of the light that is trapped travels to the sides of the LSC, where it is collected by a photovoltaic cell.

2.2.1.1 Total internal reflection

The angle at which total reflection occurs is described by Snell's law, equation 2.9, which in general describes refraction of light when traveling through a change in refractive index. [29]

$$n_i \sin \zeta_i = n_t \sin \zeta_t \tag{2.9}$$

If ζ_t, the transmitted angle, reaches ninety degrees, there is no transmitted wave, and $\sin \zeta_t$ becomes unity. So the critical angle at which total internal reflection occurs is given by equation 2.10.[2]

$$\zeta_{c,i,t} = \arcsin\left(\frac{n_t}{n_i}\right) \tag{2.10}$$

2.2.1.2 Waveguiding

Though total internal reflection is the basic principle behind waveguiding, some additional boundary conditions have to be satisfied. In a thin film the wave character of light can become an issue, as the light can interfere with itself, and could die out by destructive interference. There are

[2]Often these angles are labeled θ. Throughout this work I have tried to be as consistent as possible with all angles, therefore I have reserved θ for another angle..

nevertheless angles under which the light can travel through the waveguide without dieing out, the so called propagating modes. The eigenvalue problem describing such modes for plane waves in an infinite slab waveguide can be derived easily, and is done in many textbooks, e.g. [30, 31].

This analysis can give us, to some extend, insight in the behaviour of slab waveguides used as LSCs; the LSC can often be approximated to be of infinite extend, as the propagating directions are orders of magnitude bigger than the thickness of the film. The source in an LSC, however, is not producing plane waves, as the luminescent centres are assumed to be point dipole oscillators.

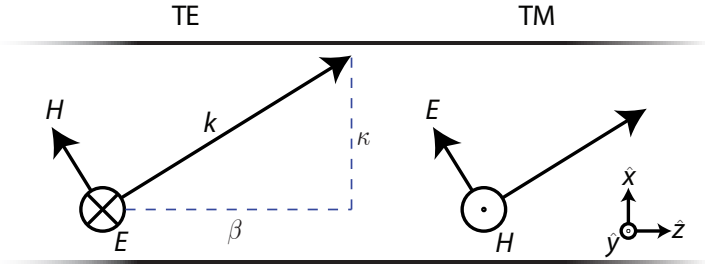

Figure 2.10: Graphic representation of the transfers electric (TE) and the transfers magnetic (TM) polarizations. In the TE figure the wave vector k is displayed along with the relation to κ and the propagation constant β.

A sketch of the procedure of the derivation is given here, a more extensive description of obtaining the eigenvalue problem can be found in e.g. [30, 31]. First of all, one should note that every polarization of light can be obtained by the linear combination of two orthogonal linear polarizations. A complete description of the slab waveguide can therefore be obtained by the separate description of transverse electric (TE) and transverse magnetic (TM) polarization, see figure 2.10. The description of the propagating modes starts with Maxwell's equations in the form of equations 2.11 and 2.14.

$$\nabla \times \mathbb{E} = -\mu_0 \frac{\partial \mathbb{H}}{\partial t} \tag{2.11}$$

$$\nabla \times \mathbb{H} = n_i^2 \epsilon_0 \frac{\partial \mathbb{E}}{\partial t} \tag{2.12}$$

$$\nabla \cdot \mathbb{E} = 0 \tag{2.13}$$

$$\nabla \cdot \mathbb{H} = 0 \tag{2.14}$$

Taking the curl of Faraday's law, equation 2.11, and eliminating $\mathbb{H}$ using Ampère's law, equation 2.12, results in the wave equation 2.15.

$$\nabla^2 \mathbb{E} + k_0^2 n_i^2 \mathbb{E} = 0 \tag{2.15}$$

In this equation k_0 is the free-space wave number, i.e. the modulus of the wave vector k, and n_i is the refractive index. We assume $\mathbb{E}$ extends to infinity in the y-direction, and is also uniform in that direction. In the z-direction we assume a dependancy of the form $e^{i\beta z}$. With these assumptions the Helmholtz equation, equation 2.16, is obtained from equation 2.15.

$$\frac{d^2\mathbb{E}}{dx^2} + \left(k_0^2 n_i^2 - \beta^2\right)\mathbb{E} = 0 \tag{2.16}$$

The Helmholtz equation can be solved for the three-layer system assuming exponential decay of the electric field in the substrate and the cladding, the air, in the x-direction, and an oscillatory solution in the film. β is the propagation constant. β appears as the z-component of the wave vector.

$$E_{film}(x) = E\cos\left(\kappa x - \phi\right) \tag{2.17}$$

$$E_{sub}(x) = E'\exp\left(\gamma x\right) \tag{2.18}$$

$$E_{air}(x) = E''\exp\left(-\delta\left[x - h\right]\right) \tag{2.19}$$

In these equations κ, γ and δ are given by equations 2.20-2.22.

$$\kappa = \sqrt{n_{film}^2 k_0^2 - \beta^2} \tag{2.20}$$

$$\gamma = \sqrt{\beta^2 - n_{sub}^2 k_0^2} \tag{2.21}$$

$$\delta = \sqrt{\beta^2 - n_{air}^2 k_0^2} \tag{2.22}$$

The relation between for instance κ, β and $k_0 \equiv |k|$ is shown in figure 2.10. β is just the z-component of the wave vector.

To solve this system one needs to oppose the boundary conditions that both $\mathbb{E}$ and its gradient with respect to x are continuous at the interfaces. This will result in the final eigenequation for the transverse electric modes, equation 2.23.

$$\tan\kappa h = \frac{\kappa\left(\gamma + \delta\right)}{\kappa^2 - \gamma\delta} \tag{2.23}$$

The eigenequation for the TE modes is a transcendental function of β, and can be solved numerically. A similar eigenequation can be obtained for the TM modes, and is given by equation 2.24.

$$\tan\kappa h = \frac{\kappa n_{film}^2\left(n_{air}^2\gamma + n_{sub}^2\delta\right)}{n_{sub}^2 n_{air}^2\kappa^2 - n_{film}^4\gamma\delta} \tag{2.24}$$

To give an example we assume an LSC of which the film functions as a waveguide, with refractive indices of 1, 1.77 and 1.93 for respectively the air, the substrate and the film. The thickness of the film is 3 μm. And we

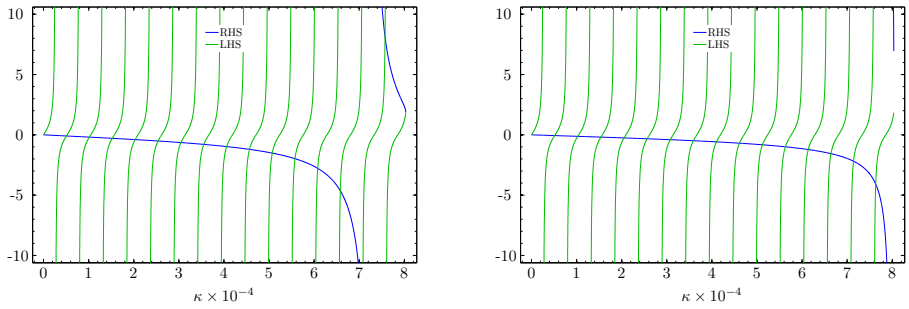

(a) (b)

Figure 2.11: The propagating TE modes (a), and TM modes (b) for an LSC, with refractive indices of 1, 1.77 and 1.93 for respectively the air, the substrate and the film, a film thickness of 3 μm and a vacuum wavelength of 611 nm. The modes are given by the crossings of the left hand side and right hand side of equation 2.23 and equation 2.24, which are plotted as a function of κ.

assume a vacuum wavelength of 611 nm. Both sides of eigenequation 2.23 can be plotted as function of κ, as is done in figure 2.11(a).

The crossings of the right hand side and left hand side in figure 2.11 give the values for κ for which there exist propagating modes. Those modes do clearly not from a continuum. The amount of propagating modes supported by a waveguide increases with increasing film thickness and decreasing vacuum wavelength. To validly apply rayopticts it is therefore important to have a film thickness much larger than the wavelength inside the film. To satisfy this requirement, the film thickness should be typically in the order of tens of micrometers when visible light is considered.

Above the Helmholtz equation 2.16 was solved for $k_0 n_{film} > \beta > k_0 n_{sub}$, which resulted in a discrete number of guided modes, varying sinusoidally inside the film and decay exponentially outside the film. Besides these guided modes, there exists a second form of guided modes, the so called substrate modes. These modes occur for $k_0 n_{sub} > \beta > k_0 n_{air}$, varying sinusoidally inside both the film and the substrate, and decaying exponentially outside. All values of β are allowed between the given boundaries[3], forming a continuum.

2.3 LSC performance

Though theory predicts total internal reflection inside the waveguide for part of the light, a significant amount of light is still lost. For example the first loss occurs at the face of the LSC, where part of the incident light is just reflected. Once the light is inside the luminescent layer, the light might not be absorbed or, if absorbed, might not be emitted again. These are just a pick at random from the various possible loss factors in LSCs.

[3]The boundaries given here are a direct result of equations 2.17-2.22. If the oscillatory mode has to be only in the film, κ, γ and δ have to be real. For an oscillatory solution in both the film and the substrate, κ and δ should be real, whereas γ should be imaginary.

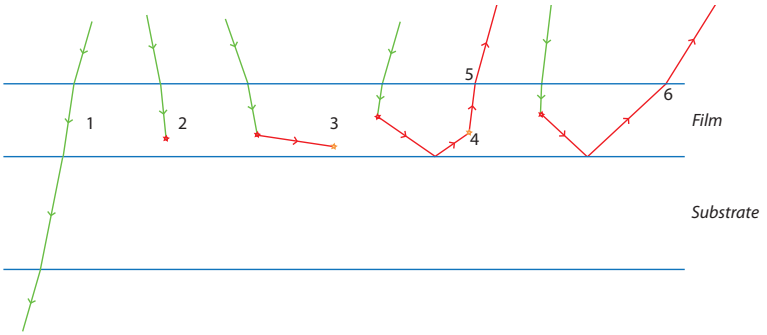

Figure 2.12: Losses in waveguides: no photon absorption, no emission, self-absorption, scattering, escape cone losses and surface impurity losses, respectively numbers 1 to 6.

In figure 2.12 a few loss mechanisms are depicted. These losses are described by equation 2.26, resulting in an optical efficiency η_{opt}.

$$\eta_{opt} = \eta_{LHE}\eta_{LQE}\eta_{Stokes}\eta_{trap}\eta_{SA}\eta_{WG}(1-R) \tag{2.25}$$

$$= \eta_{QE}\eta_{Stokes} \tag{2.26}$$

In this equation η_{LHE} is the light harvesting efficiency, described in section 2.3.1, which is the efficiency at which the incoming photons are absorbed, e.g. in figure 2.12 ray 1 is not absorbed at all. η_{LQE} is the luminescent quantum efficiency, which is the number of photons emitted per photon absorbed; in the figure ray 2 is absorbed, but not re-emitted. η_{SA} is the self-absorption, which quenches the photon output by overlap between the emission spectrum and the absorption spectrum, ray 3 in the figure. η_{Stokes} accounts for the energy loss caused by the Stokes' shift. This efficiency is the ratio between the emitted photon energy and the absorbed photon energy. η_{trap} is the trapping efficiency; part of the light absorbed is emitted inside the escape cone, whereupon it leaves the LSC, see figure 2.9 number 5. η_{WG} accounts for all losses due to waveguide imperfections, e.g. scattering inside the waveguide or at the surfaces, rays 4 and 6 respectively in figure 2.3.5. The waveguide efficiency and the self-absorption can be combined in a transport efficiency $\eta_t = \eta_{SA}\eta_{WG}$, as both factors decrease the trapped light during transport to the edge.

The part of the light that is reflected upon incidence on the face is described by Fresnel's equations [29]. The part that is reflected is a function of the incident angle, ζ_i, and is given by equation 2.27. ζ_t, the transmitted angle, can be obtained using Snell's law.

$$R = \frac{1}{2}\left\{\left[\frac{n_i \cos\zeta_i - n_t \cos\zeta_t}{n_i \cos\zeta_i + n_t \cos\zeta_t}\right]^2 + \left[\frac{n_t \cos\zeta_i - n_i \cos\zeta_t}{n_t \cos\zeta_i + n_i \cos\zeta_t}\right]^2\right\} \tag{2.27}$$

Given η_{opt}, the power efficiency gain Φ_{opt} is given by equation 2.28 [11], which takes both the geometrical gain and the efficiency of the photovoltaic (PV) cell into account. Φ_{opt} gives the ratio of power from a PV cell attached to an LSC to the power from that same PV cell exposed directly to the solar radiation. If Φ_{opt} exceeds unity, the combination of the PV cell with LSC attached delivers more power than the same PV cell without LSC. The contrary is true for a power efficiency gain below unity.

$$\Phi_{opt} = \frac{A_{face}}{A_{edge}}\eta_{opt}\frac{\eta_{PV}(\lambda_{lum})}{\eta_{PV}(solar)} \tag{2.28}$$

The geometrical gain A_{face}/A_{edge} is effectively the real concentrating part. As the face surface, A_{face}, is bigger than the edge surface, A_{edge}, on which the PV cell is mounted, the light is concentrated on the edge surface. $\eta_{PV}(\lambda_{lum})$ is the efficiency of the PV cell at a wavelength λ_{lum}, and $\eta_{PV}(solar)$ is the efficiency of the PV cell in respect to the total solar spectrum. [32] λ_{lum} represents the emission wavelength. [12]

In the next subsections all efficiencies of equation 2.26 will be discussed seperately.

2.3.1 η_{LHE} - Light harvesting efficiency

To develop a highly efficient luminescent solar concentrator one of the four main requirements is to absorb as much sunlight with wavelengths shorter than 950 nm[4], see section 2.1.3. This is quantified by the light harvesting efficiency, η_{LHE}. This quantity is described by equation 2.29. [12]

$$\eta_{LHE} = \frac{\int_0^\infty S_{SO}(\lambda)\left[1 - 10^{-A(\lambda)}\right]\,\mathrm{d}\lambda}{\int_0^\infty S_{SO}(\lambda)\,\mathrm{d}\lambda} \tag{2.29}$$

S_{SO} is the source emission spectrum, and A is the absorbance of the luminescent film as a function of wavelength λ. The absorbance is dependent on the concentration of the luminescent centers in the film and the maximum path length in the film of an incident photon. Equation 2.29 just integrates the absorbed light of the source, and divides it by the total incoming light. Note the difference between the absorbance and the absorptance: the first is defined as the the logarithm of the ratio between the incident flux and

[4]This applies of course to silicon solar cells, as the bandgap of silicon lies at about 1100 nm. When other cells are used the requirement shifts with the bandgap.

the transmitted flux, the latter is defined as the flux absorbed divided by the incident flux. This results in the property that the absorbance scales linearly with concentration and material thickness, whereas the absorptance varies exponential with concentration and thickness.

Rare-earth (RE) metals have weak absorption peaks, due to their forbidden f-f transitions, see section 2.1.4, which is displayed in figure 2.5. One way to improve the absorption is to add a sensitizer (either organic or inorganic), which absorbs the light and transfers the energy to the emitting RE luminescent centre. [19] Another solution could be the use absorption bands caused by charge transfer transitions, see section 2.1.4, recognizing that these transitions mainly occur outside the solar energy spectrum. However, as indicated before, the CT band can be lowered in energy [25].

2.3.2 η_{LQE} - Luminescent quantum efficiency

The ideal luminescent material emits at least one photon per absorbed photon. In reality however this is generally not the case. The ratio between the number of emitted photons per absorbed photon is called the luminescent quantum efficiency (LQE). LQEs of nearly 1 have been reported for organic dyes in LSCs. [33] Rare-earth based luminescent materials can have quantum efficiencies exceeding 0.9, quantum dots will not have such high LQEs. [22] The luminescence is quenched due to non-radiative relaxation processes, such as phonon relaxation. A simple competing non-radiative relaxation process would result in a faster exponential decay. This directly follows from the differential equation 2.30, in which the decay rates R_r and R_n are radiative and non-radiative respectively. $I(t)$ is the measurable intensity of the luminescence as a function of time.

$$\frac{\mathrm{d}I}{\mathrm{d}t} = -\left(R_r + R_n\right) I(t) \tag{2.30}$$

What non-radiative processes are we talking about? Lets first consider an single isolated luminescent centre. In this case there are basically two different relaxation processes: one associated with thermal quenching and the other with multi-phonon relaxation. The former is already discussed in section 2.1.2 in relation with the configurational model. Thermal quenching uses the thermal energy to lift the electron present in the excited state (ES) to the crossing between the excited state and the ground state (GS). At that point the electron can make the transition to the ground state and will relax to the bottom of the ground state by the emission of heat to the crystal lattice.

If there is no crossing between the states, or the energy difference ΔU between the bottom of the ES and the crossing of the ES and the GS is much larger than the thermal energy it is still possible to non-radiatively relax. This can occur through the emission of multiple phonons into the crystal. Such a transition has only significant probability when the energy between the ES and the GS is less than $4-5$ times the highest vibrational mode of the host crystal [17].

Again the emission intensity from a particular excited state depends on the proportions between the quenching rates and the radiative rates.

If we go even further we can consider the presence of other luminescent centres close to each other (high doping percentage). Now it is possible for the excitation energy to migrate from one centre to another. Lets consider the case with a donor (D) and an acceptor (A). The donor is excited upon absorption of a photon (D^*) and can resonantly transfer its energy to the acceptor ($D^*+A \rightarrow D+A^*$). If the acceptor now relaxes, either radiatively or non-radiatively, the luminescence for the donor is quenched. As the resonant transfer of energy strongly depends on distance, this effect becomes more noticable for higher concentrations, hence the name concentration quenching.

Even when there is just one luminescent centre, i.e. just donors, concentration quenching can be an issue. Consider the weakly coupled Rare-earths (the outer filled shells screen the 4f-shell making the coupling weak). Due to low radiative rates, caused by the parity forbidden f-f transitions, and high spectral overlap between the absorption and emission of two neighboring centres, the $D^*+D \rightarrow D+D^*$ transition can occur in the order of 10^4 [17] more often than a radiative transition. This makes energy migration possible over large distances, increasing the chance of ending in a quenching site, where it relaxes non-radiatively.

2.3.3 η_{Stokes} - Stokes' efficiency

As mentioned in section 2.1.2 the emitted photons will have a lower energy than the excitation photons. This is due to the Stokes' shift. The energy difference concerned with this shift is lost to lattice vibrations, and is therefore not longer useful. The Stokes' efficiency η_{Stokes} accounts for this loss, and is defined as the ratio between the energy of the emitted photon and the excitation photon. One should note that the energy lost due to the Stokes' shift in an LSC would normally be thermal loss in a PV cell, as the associated photons would excite an electron high into the conduction band of the PV cell.

2.3.4 η_{trap} - Trapping efficiency

To determine the parts of the light which are lost directly through the top (the red part of the sphere in figure 2.9), the part which is trapped in the film-substrate-complex (yellow in the figure) and the part that is trapped in the film only (green), the fractions of the respective parts of the surface of the sphere have to be determined.

To start with the fraction that escapes (and therefore is lost), $\eta_{tr,esc}$, is defined as the surface area of the red part, A_{red}, divided by the total surface area of the sphere, A_{sphere}. The red area is given by the integral in equation 2.31, in which R is the radius and $\zeta_{c,film,air}$ is the critical angle of the film-air interface. For the last step equation 2.10 is used with the appropriate refractive indices.

$$\begin{aligned}\eta_{tr,esc} &= \frac{A_{red}}{A_{sphere}} \\ &= \frac{2\int_0^{\zeta_{c,film,air}}\int_0^{2\pi} R^2 \sin\theta \,\mathrm{d}\phi \,\mathrm{d}\theta}{4\pi R^2} \\ &= 1 - \cos\zeta_{c,film,air} \\ &= 1 - \sqrt{\frac{n_{film}^2 - n_{air}^2}{n_{film}^2}}\end{aligned} \tag{2.31}$$

In the same way the fractions trapped in both layers and in only the film, $\eta_{tr,sub}$ and $\eta_{tr,film}$ respectively, are determined and given in equations 2.32 and 2.33.

$$\eta_{tr,sub} = \frac{1}{n_{film}}\left\{\sqrt{n_{film}^2 - n_{air}^2} - \sqrt{n_{film}^2 - n_{sub}^2}\right\} \tag{2.32}$$

$$\eta_{tr,film} = \sqrt{\frac{n_{film}^2 - n_{sub}^2}{n_{film}^2}} \tag{2.33}$$

Though the yellow part is trapped in the film-substrate-complex, the efficiency label is 'sub'. This has as primary reasons that it is a clear notation and it clearly refers to the substrate modes, which were described in section 2.2.1.2. Furthermore, in Appendix D is explained that the light trapped in the two layers combined is almost totally directed to the substrate.

η_{trap} is now given by the sum of $\eta_{tr,film}$ and $\eta_{tr,sub}$. In literature [12, 22, 32] there is no distinction made between $\eta_{tr,film}$ and $\eta_{tr,sub}$, but is only η_{trap} concerned. This is a logic consideration when the refractive indices of the film and the substrate are (nearly) equal. In the case of differing indices this distinction has to be made, as the part trapped in the film encounters lots of reflections on the surface and travels through the optically active luminescent material, thereby increasing the chance of being lost. The part trapped in the film-substrate-complex in contrary has less interaction, thereby encountering a different loss rate during propagation through the LSC.

When a silicon solar cell is attached to the sides, all vertically trapped radiation will be transmitted through the sides of the LSC, as the refractive index of the solar cell is much higher than that of the LSC. Though, if measurements are performed on the LSC surrounded by air, the light can be trapped as well in the horizontal direction, as made clear in figure 2.13. Both in the film and the substrate the escape cones do not cover the whole radiating sphere. E.g. the green parts in figure 2.13 will therefore not escape the LSC or only after for instance being scattered.

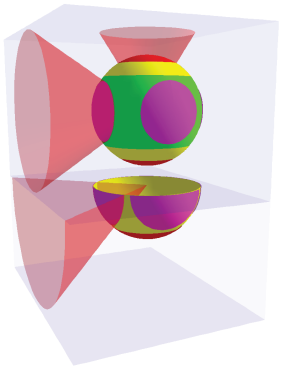

Figure 2.13: Horizontal trapping in the LSC. Horizontal escape cones are depicted with the pink circles on the sphere.

2.3.5 η_{SA} - Self-absorption

Self-absorption is the absorption of a luminescence photon by the luminescent centres self. This occurs when overlap exists between the emission spectrum and the absorption spectrum, of which an example is given in figure 2.14. In such a situation one luminescent centre can emit a photon which can be absorbed by another luminescent centre. When this occurs, again losses due to a luminescent quantum efficiency, escape cone and Stokes' shift occur. Self-absorption can therefore be considered highly undesirable.

If the Stokes' shift however is big enough, no emitted luminescence will have the energy to re-excite a luminescent centre. For more information about self-absorption I will refer to articles covering self-absorption in detail, e.g. [12, 34], as in this research self-absorption is not an important factor.

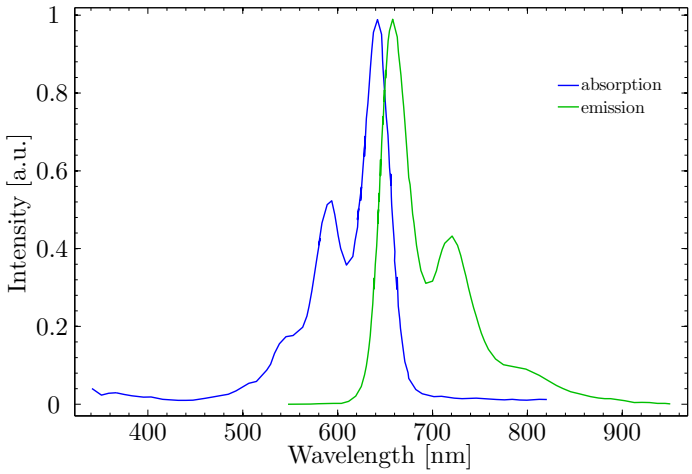

Figure 2.14: [22] Absorption and emission spectra of Lumogen red dye, clearly showing overlap between both spectra. This results in the possibility for reabsorption of an already emitted photon

2.3.6 η_{WG} - Waveguide efficiency

Idealy, once the light has been trapped inside the solar concentrator, the light is transported without further losses to the perimeter of the LSC. Aside self-absorption, see section 2.3.5, there is an intrinsic loss mechanism caused by the LSC itself. Though theory predicts total internal reflection inside the LSC, see section 2.2.1.1, light is lost through the surface due to scattering. This scattering appears in limited extend in the materials (film and substrate) self, but to a higher degree on the interfaces between the air and the substrate, the film and the substrate, and last between the film and the air. Measuring the loss caused by scattering is always done by measuring the intensity of the scattered light under normal incidence from the LSC. [35] This light is assumed to be proportional to the intensity of the light inside the waveguide. A typical measurement uses a laser beam coupled in to the waveguide and measuring the attenuation length, i.e. the typical length in the exponential decay of the intensity caused by scattering, see equation 2.34. [35–37]

$$I \propto \exp\left(-\frac{r}{\mu}\right) \tag{2.34}$$

In which μ is the attenuation length. The waveguide efficiency can be calculated as follows. Assume an LSC as depicted in figure 2.15 of size $W \times H$.

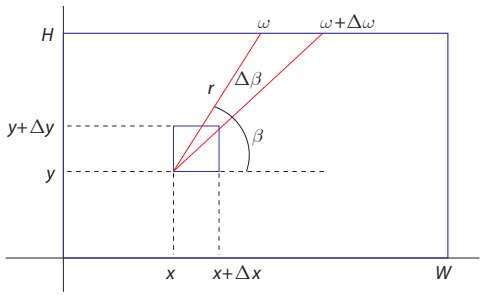

Figure 2.15: Schematic drawing of an LSC of size $W \times H$. The fraction $\Delta x \Delta y$ radiates in the direction of β over an angle $\Delta\beta$. This luminescence will decrease in intensity over distance r to the edge of the LSC.

Take the surface area $S = \Delta x \Delta y$, with both Δx and Δy small. This part radiates energy ρS, where ρ is the power radiated per unit area. The power impinging upon the boundary section $\Delta\omega$ radiated by S is given by equation 2.35.

$$P_{\Delta\omega,S} \simeq \rho S \frac{\Delta\beta}{2\pi} \exp\left\{-\frac{r}{\mu}\right\} \tag{2.35}$$

The exponent appears due to the exponential decay given in equation 2.34. One should note that, when there is self-absorption, μ contains the decay to self-absorption as well. In that situation η_{WG} changes to $\eta_t = \eta_{SA}\eta_{WG}$, with η_t the light transport efficiency. Letting $\Delta\beta$ become very small and

summing over the edge $y = H$ results in the integral for the power radiated by S incident on the the side $y = H$ of the LSC given by equation 2.36.

$$P_{y=H,S} = \frac{\rho S}{2\pi} \int_{\arctan\left[\frac{H-y}{W-x}\right]}^{\arctan\left[\frac{x}{H-y}\right]+\frac{\pi}{2}} \exp\left\{-\frac{r(y,\beta)}{\mu}\right\} \mathrm{d}\beta \tag{2.36}$$

Now, making Δx and Δy very small, summation over them results in an integral for the total power impinging upon the side $y = H$. This integral is given by equation 2.37.

$$P_{y=H} = \frac{\rho}{2\pi} \int_0^H \int_0^W \int_{\arctan\left[\frac{H-y}{W-x}\right]}^{\arctan\left[\frac{x}{H-y}\right]+\frac{\pi}{2}} \exp\left\{-\frac{r(y,\beta)}{\mu}\right\} \mathrm{d}\beta\, \mathrm{d}x\, \mathrm{d}y \tag{2.37}$$

In this equation $r(y, \beta) = (H - y)/\sin\beta$. The waveguide efficiency for a rectangular LSC is obtained after multiplication by $1/(\rho W H)$ and the summation of the four contributing sides of the LSC, and is given by equation 2.38. As the sides are equal pairwise, the sum of two tripple integrals remains.

$$\begin{aligned}\eta_{WG,rectangle} = &\frac{1}{WH\pi} \int_0^H \int_0^W \int_{\arctan\left[\frac{H-y}{W-x}\right]}^{\arctan\left[\frac{x}{H-y}\right]+\frac{\pi}{2}} \exp\left\{-\frac{H-y}{\mu\sin\beta}\right\} \mathrm{d}\beta\, \mathrm{d}x\, \mathrm{d}y \\ &+\frac{1}{WH\pi} \int_0^W \int_0^H \int_{\arctan\left[\frac{W-x}{H-y}\right]}^{\arctan\left[\frac{y}{W-x}\right]+\frac{\pi}{2}} \exp\left\{-\frac{W-x}{\mu\sin\beta}\right\} \mathrm{d}\beta\, \mathrm{d}y\, \mathrm{d}x\end{aligned} \tag{2.38}$$

Equation 2.39, the waveguide efficiency of a square LSC, is obtained when the special case where $H = W$ is considered.

$$\eta_{WG,square} = \frac{2}{W^2\pi} \int_0^W \int_0^W \int_{\arctan\left[\frac{W-y}{W-x}\right]}^{\arctan\left[\frac{x}{W-y}\right]+\frac{\pi}{2}} \exp\left\{-\frac{W-y}{\mu\sin\beta}\right\} \mathrm{d}\beta\, \mathrm{d}x\, \mathrm{d}y \tag{2.39}$$

A similar derivation can be done for a circular concentrator, figure 2.16, resulting in equation 2.40.

$$\eta_{WG,circle} = \frac{2}{(D\pi)^2} \int_0^{2\pi} \int_0^{\frac{D}{2}} \int_0^{2\pi} \tilde{r} \exp\left\{-\frac{d(\tilde{r},\beta,\xi)}{\mu}\right\} \mathrm{d}\xi\, \mathrm{d}\tilde{r}\, \mathrm{d}\beta \tag{2.40}$$

With $d(\tilde{r}, \beta, \xi)$ given by equation 2.41.

$$\begin{aligned}d(\tilde{r},\beta,\xi) = &\sqrt{\frac{D^2}{4} + r^2\left\{(\cos\xi\ cos\beta + \sin\xi\sin\beta)^2 - 1\right\}} \\ &-r\left(\cos\xi\cos\beta + \sin\xi\sin\beta\right)\end{aligned} \tag{2.41}$$

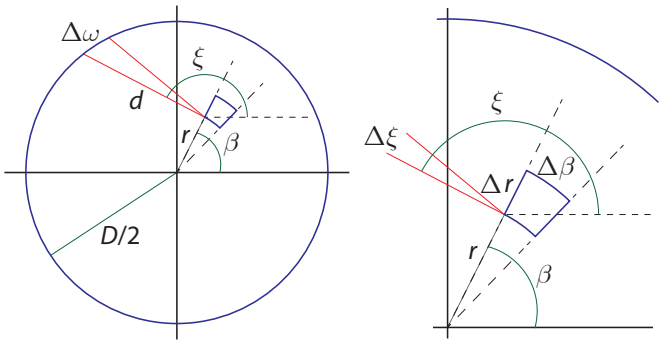

Figure 2.16: Schematic drawing of a circular LSC with diameter D. d is the distance from luminescent area $\sin\beta\Delta\beta\Delta r$. β and ξ give respectively the angles between the horizontal axis and $\vec{r}$ and the horizontal axis and $\vec{d}$. The luminescence attenuates over distance d to the edge of the LSC.

Let us now consider the meaning of the mathematics of the transport efficiency. Remember that the transport efficiency η_t is just the more general case which is given by $\eta_{SA}\eta_{WG}$. The mathematics stays the same, as μ will contain some extra information about the self-absorption loss. The analysis will be done using the square LSC, which is just a special case of the rectangular LSC (equation 2.38).

To get a fast insight in the integrals, the transport efficiencies have been represented graphically in figure 2.17. Figure 2.17 (a) shows the light transport efficiency, or in the case of zero self-absorption the waveguide efficiency, as a function of the size of the LSC (or the size of the window) for various linear attenuation lengths μ. Figure 2.17 (b) shows the light transport efficiency as a function of the linear attenuation length for various window sizes. Figure 2.17 (a) correctly shows that for small waveguide dimensions, the transport efficiency approaches 100%. This is expected, as for small waveguides, light does not have to travel far to reach the perimeters of the LSC. The figure shows that for a typical window size of 2 m^2, a linear attenuation length μ of more than 1000 mm is needed in order to have a light transport efficiency of more than 50%. Interestingly, figure 2.17 (a) shows that the efficiencies become more and more constant towards larger LSC sizes. We conclude that for larger LSC sizes only a certain edge region, close to the perimeter, contributes to the total of emitted light that reaches the perimeters. The LSC regions to the centre of the waveguide do contribute much less, as most luminescence emitted in the centre does not reach the perimeter anymore. In figure 2.17 (b) it is clearly visible that the transport efficiency goes to zero for very small attenuation lengths. This is exactly what we expect as the light is lost before it reaches the perimeter of the LSC.[5]

Though these figures are informative, both pictures can be combined into a single graph by defining an dimensionless attenuation length $\text{La} \equiv \mu/W$. W is chosen to be the shortest side of the LSC with dimensions $W \times H$. Now

[5]It is comforting to observe that the efficiency becomes high when μ is close to the window size.

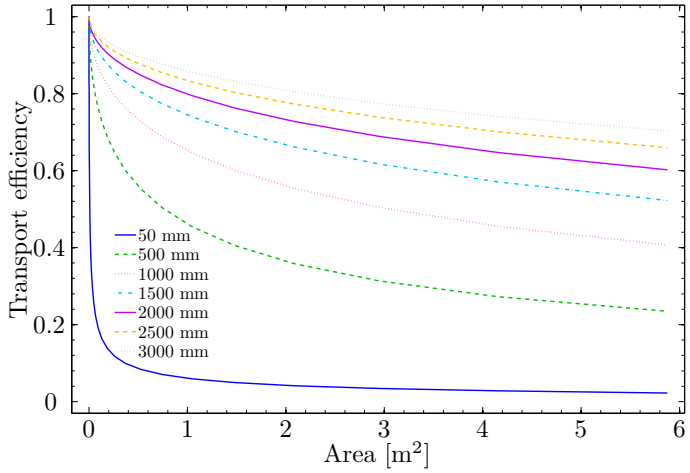

(a)

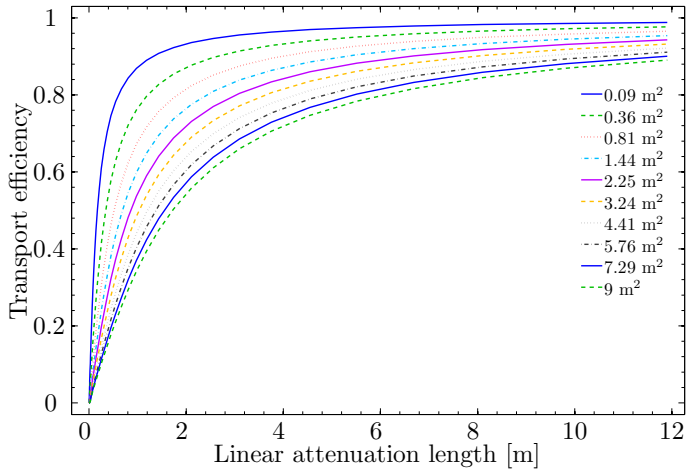

(b)

Figure 2.17: The transport efficiencies of different square LSCs as function of LSC size (a) or linear attenuation length (b).

the transport efficiency can be plotted as a function of this dimensionless attenuation length, which is done in figure 2.18. The transport efficiency is plotted for three differently proportioned LSCs. Again the transport efficiency goes to zero for small μ compared to the size W, and to unity for large μ compared to W.

The transport efficiency of figure 2.18 can be fitted with the empirical formula given by equation 2.42.

$$\eta_t \simeq \frac{\mathrm{La}^n}{K + \mathrm{La}^n} \tag{2.42}$$

In this equation $\mathrm{La} = \mu/W$ is the dimensionless attenuation length, and n and K are two fitting parameters. Table 2.1 gives for the three plotted

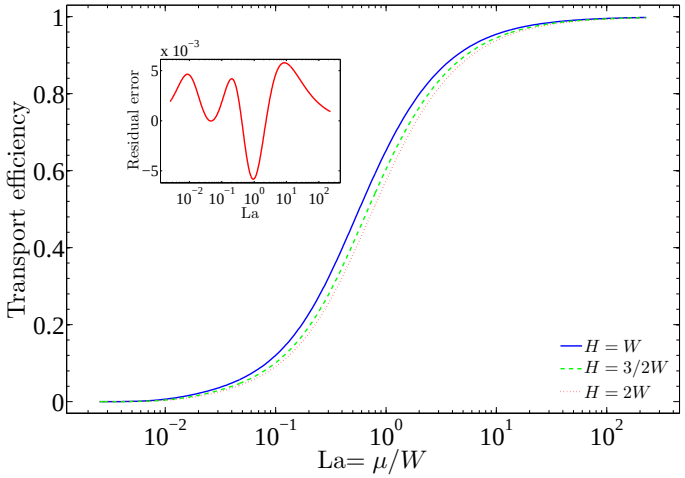

Figure 2.18: Transport efficiency of LSCs as a function of the dimensionless attenuation length, $\mathrm{La} = \mu/W$**.** $W \leq H$ **for an LSC with dimensions** $W \times H$

curves in figure 2.18 the values of the fitting parameters. The inset of figure 2.18 shows the residual error for the square LSC. It can be observed that the error never exceeds a deviation greater than 0.6 percentage point.

Table 2.1: Values of the fitting parameters of equation 2.42 for LSCs with different proportions.

W:H	K	n
1:1	0.547	1.117
2:3	0.673	1.113
1:2	0.760	1.106

As the two layer LSC consists of two transport guides, i.e. the film and the substrate, two different transport efficiencies are expected. The transport efficiency can then be given by equation 2.43. Here, both transport efficiencies are scaled with the relative amount of light trapped in the film and the substrate, assuring the total transport efficiency will not exceed unity.

$$\eta_t = \frac{1}{\eta_{tr,film} + \eta_{tr,sub}} \left[\eta_{tr,film}\eta_{t,film} + \eta_{tr,sub}\eta_{t,sub}\right] \tag{2.43}$$

2.3.7 η_{power} - Power efficiency

With all separate efficiencies of equation 2.26 identified it is possible to calculate the power efficiency of an LSC with solar cells attached to its perimeter. This is given by the optical efficiency, η_{opt}, times the power efficiency of the solar cell. The fictitious luminescent material has an absorptance of 0.8 for light with an energy exceeding the absorption edge. For

light with lower energies the luminescent material is fully transparent. As source an AM1.5[6] spectrum [38] is used, which is displayed in figure 2.19.

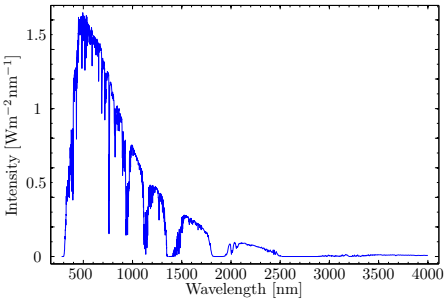

Figure 2.19: ASolar AM 1.5 spectrum, direct with circumsolar.

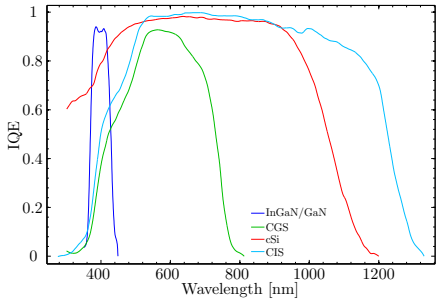

Figure 2.20: The IQE curves of InGaN/GaN [39], CGS [40], cSi [41] and CIS [42]

Now the luminescent harvesting efficiency can be calculated as a function of absorption edge using equation 2.29. The material has a realistic luminescent quantum efficiency of 0.8 and no self-absorption, i.e. the luminescent light is outside the absorption spectrum of the material. The Stokes efficiency has been calculated using the average absorbed photon energy of the AM1.5 spectrum and the energy of the luminescence photons, which was taken 10 nm longer than the absorption edge to avoid self-absorption. The trapping efficiency was based on the refractive index of Lu_2O_3:Eu^{3+}, which is 1.933. Seven waveguide efficiencies have been used, based on different dimensions of the LSC and different attenuation lengths. It is chosen to use only one type of solar cell at a time, but different solar cells for different absorption edges of the luminescent material. The following solar cell materials are used: InGaN/GaN [39], CGS [40], cSi [41] and CIS [42]. The power efficiency of the solar cells was calculated as function of absorption edge using the internal quantum efficiencies, shown in figure 2.20. A second energy shift was added to discard the excess energy of the luminescence photons compared to the band gap energy of the solar cells.

In figure 2.21 one finds the resulting power efficiencies for different sized LSCs and for different attenuation lengths. In figure 2.21 (a) one finds the power efficiency, which is the power delivered by the solar cell divided by the illumination power incident on the LSC. Figure 2.21 (a) gives the power delivered per area solar cell.[7] This is where the concentrating effect really becomes apparent. The sun delivers a power of about 1 kWm^{-2}, whereas the the solar cells deliver a power in the order of tens of kWm^{-2}.

[6] AM1.5 indicates that the sunlight is considered which had a path length through the atmosphere of 1.5 the atmosphere thickness. AM is short for air mass.

[7] The area of solar cell is based on an LSC thickness of 3 mm

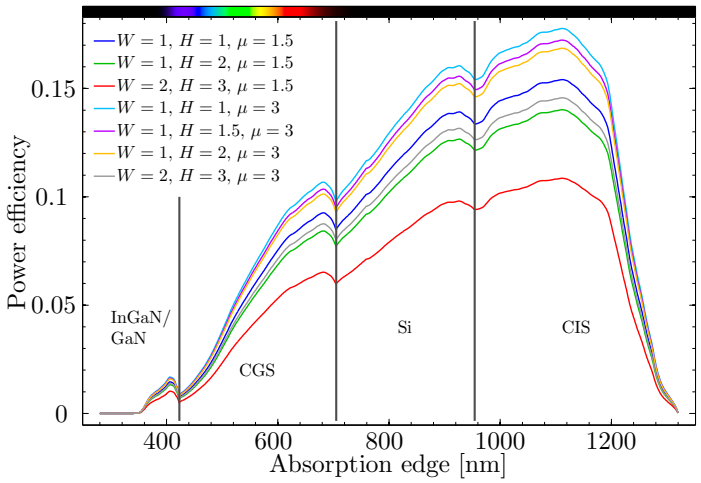

(a)

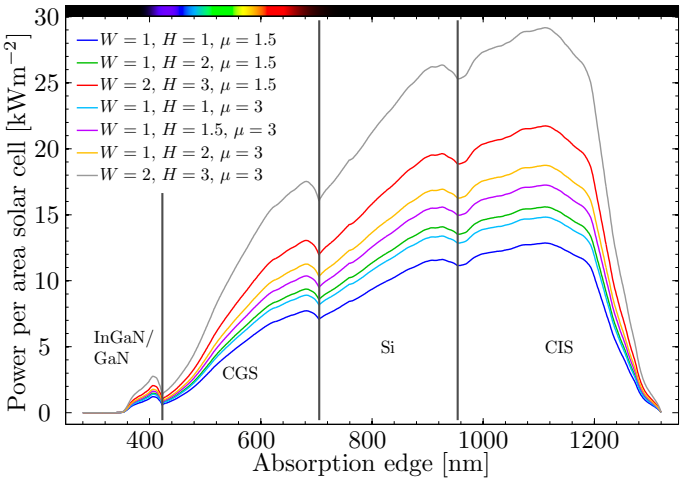

(b)

Figure 2.21: The power efficiencies of complete PV devices as a function of absorption edge of the luminescent material. In (a) the power efficiencies are shown for different sized LSCs and different attenuation lengths. In (b) the output power per area solar cell is given. The IQEs of the different solar cells used in the calculations are given in figure 2.20.

2.3.8 Directional intensity profile

Though the ability to give some quantitative scale on the transport losses using a single attenuation length has been suggested before [14], this might need to be reconsidered. As the angle under which the light travels through the waveguide changes, the interaction with the interfaces and path length change. The more interaction, the more loss, which suggests an angle dependent attenuation length. This dependency must become apparent when looking at the output profile, as for such a profile the angles inside the waveguide vary. This is the reason to consider the output profile, of which the concept is shown in figure 2.22.

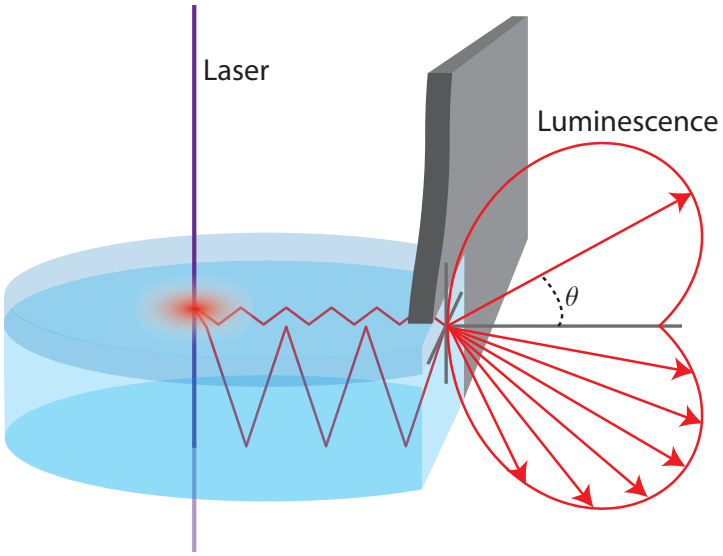

Figure 2.22: Schematic representation of the directional output profile.

When light is incident on an LSC, part of the light is absorbed, emitted, trapped and guided in the LSC. Once reaching the perimeter of the waveguide the light is either refracted out of the LSC or reflected back in. The light refracting out is interesting as it results in a potentially measurable directional intensity profile. Using ray optics an analytic expression can be derived for this intensity profile without imposing too many restrictions. As written in section 2.2.1.2 the assumption that ray optics fully applies to thin films may be the weakest link in this theory. Nevertheless, this theory can also be applied to LSCs with thicker films, or even single slab LSCs without a film.

In figure 2.23 the relevant angles are depicted for the directional intensity profile calculations. The objective is to give an expression for the intensity radiating from the perimeter (interface 1) of the LSC as a function of the two viewing angles θ and ϕ. It is assumed that the luminescent centres (the red dot) are radiating isotropically. The angles are named such that the capital characters denote angles inside the substrate, and the lower characters denote the emitting and observation angles. Besides, the angles α and A relate via Snell's law equation 2.9, through interface 2, and the angles θ

and Θ do so through interface 1.

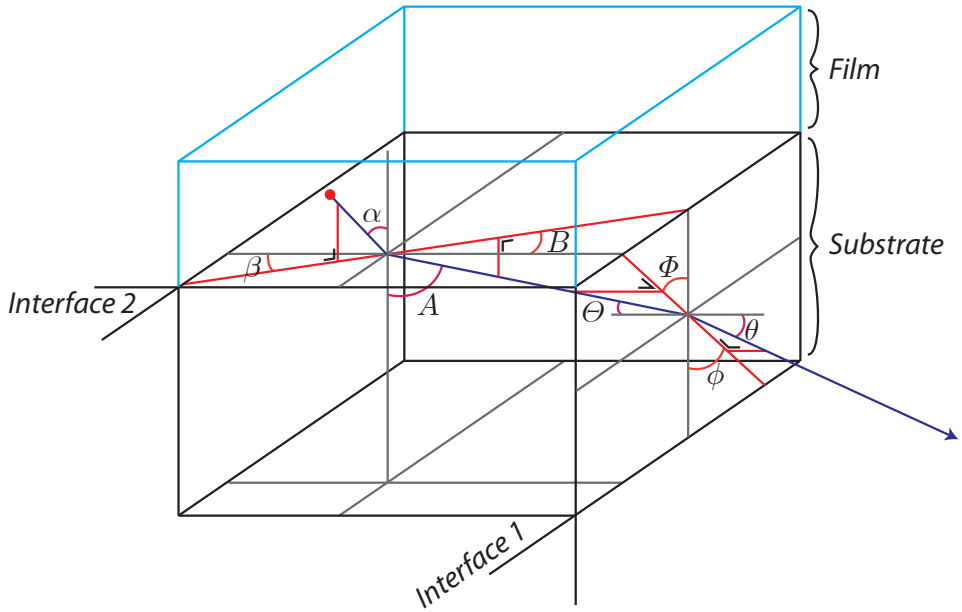

Figure 2.23: Relevant angles for the directional intensity profile calculations depicted in a schematic view of a thin film LSC. Capital characters denote angles inside the substrate, whereas lower characters denote the emitting and observation angles.

First step is to notice that the power radiated from a luminescent centre through a solid angle defined by small angles $\mathrm{d}\alpha$ and $\mathrm{d}\beta$ is given by the following expression:

$$\mathrm{d}P = \frac{P_0}{4\pi} \sin\alpha \,\mathrm{d}\alpha \,\mathrm{d}\beta \tag{2.44}$$

In this equation P_0 is the total power radiated by the luminescent centre, and α and β are the angles as defined in figure 2.23.

Now the only trick is to rewrite α and β in terms of the observation angles ϕ and θ. Which leaves us with equation 2.45.

$$\mathrm{d}P = \frac{P_0}{4\pi} \sin[\alpha(\phi,\theta)] \left[\frac{\partial\alpha}{\partial\phi}\mathrm{d}\phi + \frac{\partial\alpha}{\partial\theta}\mathrm{d}\theta\right] \left[\frac{\partial\beta}{\partial\phi}\mathrm{d}\phi + \frac{\partial\beta}{\partial\theta}\mathrm{d}\theta\right] \tag{2.45}$$

This equation can be worked out neglecting quadratic terms in $\mathrm{d}\alpha$ and $\mathrm{d}\beta$ to equation 2.46.

$$\mathrm{d}P = \frac{P_0}{4\pi} \sin[\alpha(\phi,\theta)] \left\{\left|\frac{\partial\alpha}{\partial\phi}\frac{\partial\beta}{\partial\theta}\right| + \left|\frac{\partial\alpha}{\partial\theta}\frac{\partial\beta}{\partial\phi}\right|\right\} \mathrm{d}\phi\,\mathrm{d}\theta \tag{2.46}$$

Note that the absolute values of the products of the derivatives are considered in equation 2.46, as angles flip sign when reflected at a surface. From this result one obtains the intensity as function of ϕ and θ after dividing by the infinitesimal area $\sin\theta\,\mathrm{d}\phi\,\mathrm{d}\theta$. The result is written in equation 2.47.

$$I(\phi,\theta) = \frac{P_0}{4\pi}\frac{\sin\alpha(\phi,\theta)}{\sin\theta}\left\{\left|\frac{\partial\alpha}{\partial\phi}\frac{\partial\beta}{\partial\theta}\right| + \left|\frac{\partial\alpha}{\partial\theta}\frac{\partial\beta}{\partial\phi}\right|\right\} \tag{2.47}$$

The second more laborious step is to write α and β in terms of ϕ and θ. This exercise is done for both the film and the substrate separately, but involve the exact same steps. For the substrate only an additional refraction in interface 2 is added.

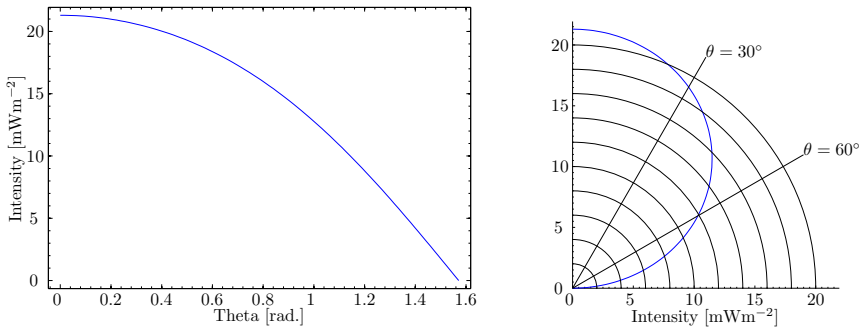

(a) (b)

Figure 2.24: The intensity emitted from the film as function of θ for $\phi = 0$ and $P_0 = 1$ W. (a) and (b) are representations in a cartesian and a polar coordinate system.

2.3.8.1 Film

First is the refraction through interface 1, giving the following relations:

$$\Phi(\phi) = \phi$$

$$\Theta(\theta) = \arcsin\left(\frac{n_{air}}{n_{film}}\sin\theta\right) \tag{2.48}$$

The expressions for A and B as function of Φ and Θ are not obvious, but can be derived with goniometry, and are given in equation 2.49.

$$A(\phi,\theta) = \arccos\left\{\cos\left[\Phi(\phi)\right]\sqrt{1-\cos^2\Theta(\theta)}\right\}$$

$$B(\phi,\theta) = \arcsin\left\{\sin\left[\Phi(\phi)\right]\frac{\sqrt{1-\cos^2\Theta(\theta)}}{\sqrt{1-\cos^2\left[\Phi(\phi)\right]\left(1-\cos^2\Theta(\theta)\right)}}\right\} \tag{2.49}$$

In the simple case of the film, the angles A and B equal the angles α and β respectively. Combining equations 2.48 and 2.49 result in the following expressions for α and β as function of ϕ and θ.

$$\alpha(\phi,\theta) = \arccos\left(\cos\phi\sqrt{\frac{n_{air}^2\sin^2\theta}{n_{film}^2}}\right)$$
$$\beta(\phi,\theta) = \arcsin\left(\frac{\sin\phi\sqrt{\frac{n_{air}^2\sin^2\theta}{n_{film}^2}}}{\sqrt{1-\frac{n_{air}^2\cos^2\phi\sin^2\theta}{n_{film}^2}}}\right) \tag{2.50}$$

Now all derivatives can be calculated. With those and equation 2.47, the directional intensity profile for the film can be determined. This exercise is best done with a mathematical program like 'Maple' or 'Mathematica', as big not informative formulas are the result. Though the expression itself is not given here the result is plotted in figure 2.24.[8]

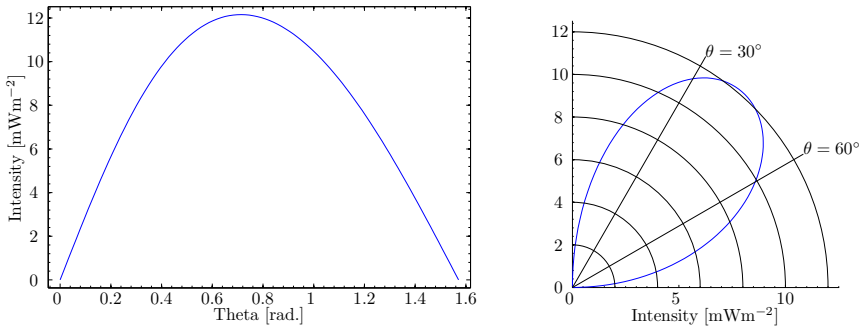

(a) (b)

Figure 2.25: The intensity emitted from the substrate as function of θ for $\phi = 0$ and $P_0 = 1$ W. (a) and (b) are representations in a cartesian and a polar coordinate system.

2.3.8.2 Substrate

The derivation for the substrate is similar to the one for the film up to equation 2.49.[9] At this point an additional refraction through surface 2 is added to go from A and B to respectively α and β, see equation 2.51.

$$\alpha(\phi,\theta) = \arcsin\left(\frac{n_{sub}}{n_{film}}\sin A(\phi,\theta)\right)$$
$$\beta(\phi,\theta) = B(\phi,\theta) \tag{2.51}$$

This results in the following equations for α and β as function of ϕ and θ:

[8] The functions of the film intensity and the substrate intensity are given though in Appendix E.

[9] Obviously the refractive index of the film in equation 2.48 will change to that of the substrate.

$$\alpha(\phi,\theta) = \arcsin\left(\frac{n_{sub}\sqrt{1-\frac{n_{air}^2\cos^2\phi\sin^2\theta}{n_{sub}^2}}}{n_{film}}\right)$$
$$\beta(\phi,\theta) = \arcsin\left(\frac{\sin\phi\sqrt{\frac{n_{air}^2\sin^2\theta}{n_{sub}^2}}}{\sqrt{1-\frac{n_{air}^2\cos^2\phi\sin^2\theta}{n_{sub}^2}}}\right) \tag{2.52}$$

Again writing out the expression for the intensity as function of ϕ and θ is best done with a mathematical program. In figure 2.25 the resulting intensity for $\phi = 0$ is plotted as function of θ.

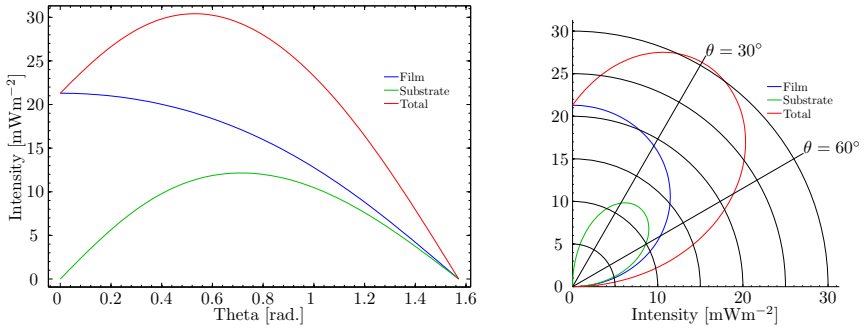

(a) (b)

Figure 2.26: The intensity emitted from the substrate, the film and the sum of both as a function of θ for $\phi = 0$ and $P_0 = 1$ W. (a) and (b) are representations in a cartesian and a polar coordinate system respectively.

2.3.8.3 Extended model

So far, no losses are introduced, giving the opportunity to define the ideal output model equation 2.53, which combines the output of the film and the substrate.

$$I_{ideal}(\phi = 0,\theta) = |AI_{sub}(\phi = 0,\theta)| + |BI_{film}(\phi = 0,\theta)| \tag{2.53}$$

I_{sub} and I_{film} are the respective output profiles of the substrate and the film. The ideal model, and the two separate intensity profiles are shown in figure 2.26.

This output profile though, is not what will be observed. Two reasons can be given. First, not all light that reaches the perimeter of the LSC is coupled out. Due to Fresnel reflections part of the light is reflected back in the LSC. As the sides are painted black, this light will never be able to reach the outcoupling surface again. Therefore, a factor T, the Fresnel

transmission has to be added, which is given by $1 - R$, with R the Fresnel reflection, given by equation 2.27. This transmission factor depends on the refractive index of the air, the refractive index of either the film or the substrate, and the viewing angles θ and ϕ. Note that ϕ is chosen zero in the experiments.

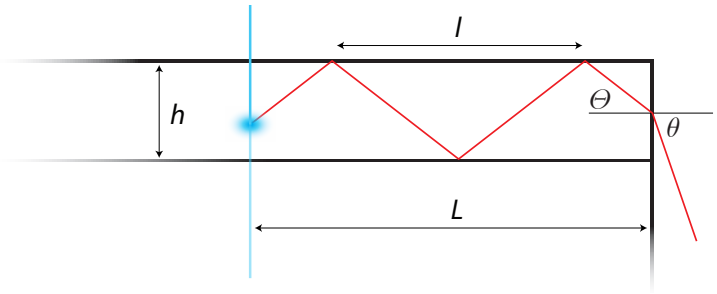

Figure 2.27: Schematic representation of the end of an thin film LSC.

Second, there is an angle dependant loss during transport. If we look at figure 2.27, we see that the larger Θ the more interaction exists with the interfaces. So we can conclude that the attenuation length μ is not constant with angle Θ. We can however define μ as equation 2.54, in which l is the distance from interface interaction to interface interaction, like shown in figure 2.27.

$$\mu = \tilde{\mu} l\left(\Theta\right) \tag{2.54}$$

The intensity drops exponentially over distance, with attenuation length μ. Furthermore, a decrease proportional to $1/L$ is expected, due to the radial spread in intensity. So, at the edge the intensity has dropped with a factor:

$$\begin{aligned} \frac{1}{r}\exp\left[-\frac{r}{\mu}\right]\Bigg|_{r=L} &= \frac{1}{L}\exp\left[-\frac{L}{l\tilde{\mu}}\right] \\ &= \frac{1}{L}\exp\left[-\frac{L\left|\tan\Theta\right|}{2h\tilde{\mu}}\right] \\ &= \frac{1}{L}\exp\left[-\frac{\Gamma}{\tilde{\mu}}\right] \end{aligned} \tag{2.55}$$

This exponential attenuation and the internal reflection are added to the ideal output model, given by equation 2.53, which results in the extended output model, given by equation 2.56.

$$\begin{aligned} I_{ext}\left(\phi=0,\theta\right) = &\left|\frac{A}{L}e^{-\frac{\Gamma\left(n_{air},n_{sub},\theta\right)}{\tilde{\mu}_{sub}}} I_{sub}\left(\phi=0,\theta\right) T\left(n_{air},n_{sub},\theta\right)\right| \\ &+\left|\frac{B}{L}e^{-\frac{\Gamma\left(n_{air},n_{film},\theta\right)}{\tilde{\mu}_{film}}} I_{film}\left(\phi=0,\theta\right) T\left(n_{air},n_{film},\theta\right)\right| \end{aligned} \tag{2.56}$$

Given $\tilde{\mu}$ can be determined using a directional measurement and the formula of the extended output model, the transport efficiency can be determined by the weighted superposition of the transport efficiencies associated with the respective propagation angles.

$$\eta_t = \frac{\int f(\Theta)\, \tilde{\eta}_t(\tilde{\mu}, h, \Theta)\, \mathrm{d}\Theta}{\int f(\Theta)\, \mathrm{d}\Theta} \tag{2.57}$$

With $f(\Theta)$ the angular distribution function. $\tilde{\eta}_t(\tilde{\mu}, h, \Theta)$ is given by equation 2.38, 2.39, 2.40 or 2.42.

Lets write down the transport efficiencies of the film and the substrate. As the angular distribution in the film is homogeneous, f is just a constant. Resulting in the simple equation 2.58 for the transport efficiency of the film.

$$\eta_{t,film} = \frac{\int_0^{\pi/2-\zeta_{c,film,sub}} \eta_t(\tilde{\mu}, h, \Theta)\, \mathrm{d}\Theta}{\pi/2 - \zeta_{c,film,sub}} \tag{2.58}$$

The angular distribution function of the substrate can be found considering the refraction in interface 2 shown in figure 2.23. If we express A in terms of α and take the derivative with respect to α, we obtain the angular distribution function.

$$\begin{aligned} f_{sub}(\Theta) &= \frac{\partial}{\partial A}\alpha(A) \\ &= \frac{\partial}{\partial A} \arcsin\left(\frac{n_{sub}}{n_{film}} \sin A\right) \\ &= \frac{n_{sub} \cos A}{n_{film}\sqrt{1 - \frac{n_{sub}^2 \sin^2 A}{n_{film}^2}}} \end{aligned} \tag{2.59}$$

A is defined as $\pi/2 - \Theta$. Using this relation the transport efficiency for the substrate is given by equation 2.60.

$$\eta_{t,sub} = \frac{\int_0^{\pi/2-\zeta_{c,sub,air}} f_{sub}(\Theta)\, \eta_t(\tilde{\mu}, h, \Theta)\, \mathrm{d}\Theta}{\int_0^{\pi/2-\zeta_{c,sub,air}} f_{sub}(\Theta)\, \mathrm{d}\Theta} \tag{2.60}$$

2.3.8.4 Validation

One obvious quick verification of the ideal output model is to calculate the amount of power radiated from one side of the perimeter of the film by integration of the intensity from the film over all angles. This value can be compared to the calculation of the loss through the escape cone, which is

given by equation 2.31 in section 2.3.4. It appears indeed that the following equality holds if $P_0 = 1$:

$$2\int_0^{2\pi}\int_0^{\pi/2} I_{film}(\phi,\theta)\,\mathrm{d}\theta\,\mathrm{d}\phi = 1 - \sqrt{\frac{n_{film}^2 - n_{air}^2}{n_{film}^2}} \tag{2.61}$$

A second easy check is to define $n_{film} = n_{sub}$. By doing so, the substrate will just act as the film, as there is no discernable interface between them anymore. What is expected is that the output profile of the substrate will equal that of the film. In a mathematical program, like Maple or Mathematica, it is easy to verify, that this is indeed the case.

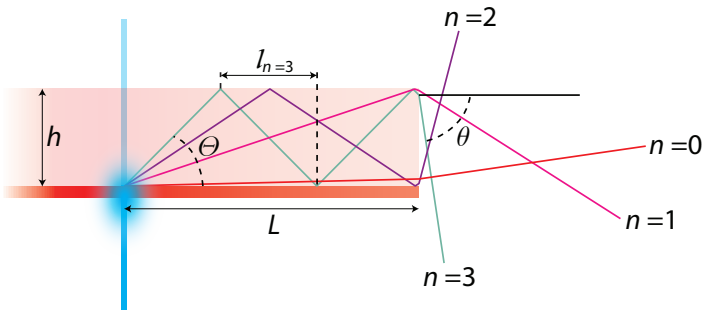

Figure 2.28: Schematic drawing of the alternating behaviour in LSCs. α, l and θ are shown for $n = 3$.

If not the whole LSC is illuminated one should be careful applying this angle dependent theory. If the illuminated area is too small, one will observe alternating behaviour in output as a function of angle. This is easy to understand if you consider the excitation spot at the downside of the LSC, see figure 2.28. Without reflections the first part will exit the LSC in upward direction. With only one reflection the light will exit in downward direction, and so on. As will be shown below, there are a few ways to overcome this effect. To see how, the effect is described mathematically first.

Consider an excitation spot at distance L from the out-coupling surface. Define a length l parallel to L, giving the distance between two reflections, which is given by equation 2.62, with n the number of reflections.

$$l = \frac{L}{n} \tag{2.62}$$

Define α to be the angle for which n reflections occur, given by equation 2.63, in which h is the thickness of the substrate. In this expression the oscillating character shows up in the last term.

$$\tan\Theta = \frac{h}{l}\,(-1)^{floor(n)} \tag{2.63}$$

Using Snell's law, equation 2.9, the exiting angle, θ can be defined as equation 2.64.

$$\theta = \arcsin\left\{n_{sub}\sin\Theta\right\} \tag{2.64}$$

Using equations 2.62 and 2.63, equation 2.64 can be rewritten as equation 2.65.

$$\theta = \arcsin\left\{n_{sub}\frac{hn}{L\sqrt{1+\frac{h^2n^2}{L^2}}}\right\}(-1)^{floor(n)} \tag{2.65}$$

Equation 2.65 clearly oscillates as function of n, as all other parameters are exclusively positive. Secondly, θ appears to be a function of the ratio h/L. The behaviour of the light distribution due to changing n or ratio h/L is shown in figure 2.29.

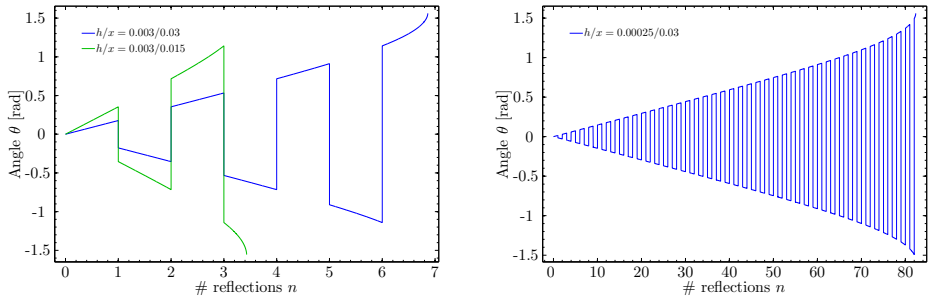

(a) (b)

Figure 2.29: The exiting angle β as a function of number of reflections inside the LSC, showing a discontinuous output profile. Figure (a) shows the exiting angles for a substrate thickness, h, of 3 mm and excitation distances, L, of 3 cm and 2.8 cm. Figure (b) shows the exiting angles for a substrate thickness, h, of 250 μm and an excitation distance, L, of 3 cm.

Figures 2.29 (a) and (b) clearly show that the thinner the substrate the more reflections occur. The discontinuities decrease in size as well, therefore it can be concluded that the thinner the substrate, the less pronounced the discontinuities are. Due to the dependence on the ratio h/L, the opposite is true for the excitation distance L, as can be seen in figure 2.29 (a).

There are a few conditions under which the discontinuities are indiscernible. First of all, when the ratio h/L becomes very small. Secondly, when the excitation is spread out over a larger area instead of a small spot. The effect of a bigger spot can be understood considering figure 2.29 (a). Assume the two lines displayed are showing the angular output of the two limits of the excitation spot, i.e. the spot extends over the area $L_{close\ limit} = 0.015$ m to $L = 0.03_{far\ limit}$ m. In this situation all values of θ in between the green and blue lines are present as well. This smears out the discontinuities. It can easily be shown[10] that full overlap starts when $L_{far\ limit} = 2L_{close\ limit}$, here $L_{far\ limit}$ is the furthest edge of the excitation spot from the outcoupling surface and $L_{close\ limit}$ the closest edge of

[10] Just solve the equality $\beta\left(h/L_{far\ limit}, n=2\right) = \beta\left(h/L_{close\ limit}, n=1\right)$.

the excitation spot to the outcoupling surface. The figure shows indeed that $\beta\,(h/L = 0.003/0.03, n = 2) = \beta\,(h/L = 0.003/0.015, n = 1)$. A last option is to add an extra film to the other side of the substrate. The output angles will be mirrored in the n-axis, forming a continuum.

Chapter 3

Experimental Approach

In this chapter the several experimental setups are discussed. Almost all measurements are linked to one of the efficiencies described in section 2.3. In total five of these efficiencies are determined experimentally, viz the light harvesting efficiency, the self-absorption, the luminescent quantum efficiency, and the light transport efficiency. An extra characterisation of the LSC is performed by measuring an excitation spectrum.

3.1 Light harvesting

The light harvesting consists out of two parts, i.e. the reflection measurement and the transmission measurement. As the reflection, transmission and absorption should add up to unity, the only unknown is the required absorption.

3.1.1 Reflection measurements

The reflection has been measured for 250nm only. A laser beam impinges upon the surface of the LSC at a small angle (about 3 degrees). With a power sensor (Thorlabs S120UV, 200-1100nm) the beam power is measured before and after the reflection. The ratio gives the reflection. Figure 3.1 shows the the setup schematically. The transparent power meter is of course removed while measuring the reflection.

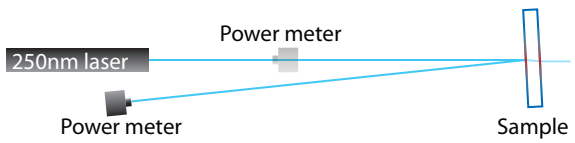

Figure 3.1: Schematic representation of reflection measurement setup. [43]

3.1.2 Transmission measurements

Transmission measurements have been performed using two different setups. One using a Bruker Vertex 80v, section 3.1.2.1, and the other using

a fiber optic spectrometer and light source of AvaSpec, section 3.1.2.2. The transmission spectrum is for both setups determined by the division of the transmission spectrum by the lamp spectrum.

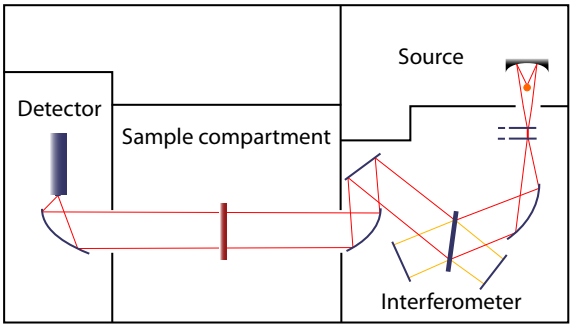

Figure 3.2: Schematic representation of an FT-IR spectrometer. [43]

3.1.2.1 Bruker Vertex 80v

The Bruker Vertex 80v consists basically out of four main components, which are the light source, the Michelson interferometer, the sample compartment and a detector, as depicted in figure 3.2. As explained above, the light travels from the light source through the interferometer, through the sample, and is collected by the detector. The principle behind is based on interference of the light with itself, caused by difference in path length after splitting of the illumination beam. The transmission signal is measured for many positions of the movable mirror of the interferometer, resulting in a set of measurements with different interference. A Fourier transform of the acquired data yields the transmission spectrum. A detailed description can be found in for instance reference [44].

Table 3.1 gives the different light sources and detectors used for the different spectral regions.

Table 3.1: Lamps and detectors with their emission and sensitivity ranges. Source Appendix C.

Lamp	**Region**	**Emission range** [10^3 cm^{-1}]
Deuterium	UV-**VIS**	40-13
Tungsten	VIS-**NIR**-MIR	25-2

Detector	**Region**	**Sensitivity range** [10^3 cm^{-1}]
GaP D520	UV	60-20
Si D510	VIS	40-10
InGaAs D424	NIR	16-5

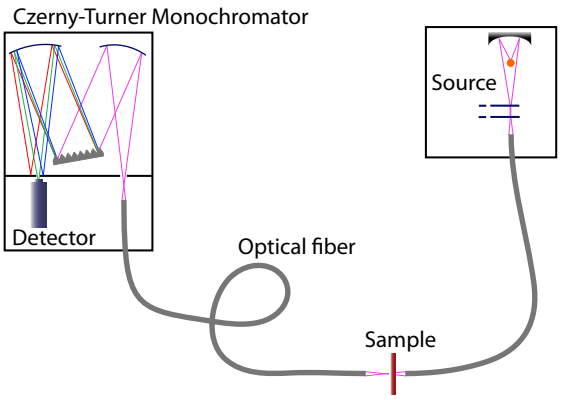

Figure 3.3: Schematic representation of the Avantes setup. The left part is a schematic representation of the detector section with the Czerny-Turner monochromator [45], the right part is the light source. The purple lines represent polychromatic light from the source, whereas the other coloured lines represent monochromatic light.

3.1.2.2 AvaSpec-3648

The transmission measurements have been performed using a AvaLight-DHc light source, emitting in the UV-NIR spectral region, and an AvaSpec-3648 Czerny-Turner spectrometer.

In figure 3.3 the Avantes setup is shown. The setup consists of two parts: one containing an AvaLight-DHc light source, emitting in the UV-NIR spectral region, the other an AvaSpec-3648 Czerny-Turner spectrometer and a detector. From the source the light is guided towards and from the sample through an optical fiber. The Czerny-Turner monochromator selects one wavelength by means of a revolving grating, shown in figure 3.3. For a more detailed discussion of such a monochromator see [46]. This single wavelength is recorded by a ccd camera. The division of the transmitted spectrum by the reference spectrum (measured respectively with and without a sample in place) yields the transmission spectrum.

3.2 Self-absorption

To determine whether there is any self-absorption or not, an emission spectrum is needed along with the absorption spectrum. The emission spectrum shows the spectrum of light emitted by a luminescent material when illuminated with monochromatic light.

The emission spectrum is obtained by excitation of a luminescent sample at one fixed wavelength and the detection of the emitted light at varying wavelength. This measurement is performed with the setup shown in figure 3.4. The source, a 450 Watt Xenon-lamp lamp, is shown at the right. With the monochromator directly left to the source the excitation wavelength is selected. Then the monochromatic light hits the sample, which emits the sought-after spectrum. To obtain this spectrum the second monochromator selects one wavelength at a time, see e.g. table 3.2,

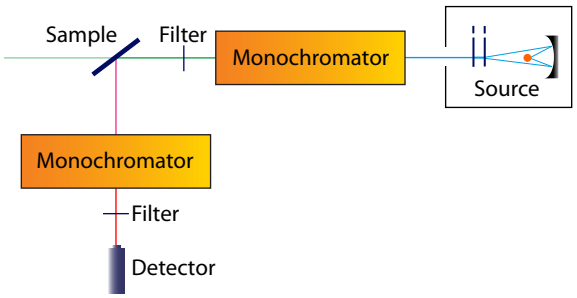

Figure 3.4: Schematic representation of the setup used for obtaining the emission and excitation spectra. On the right the source is displayed. After the source is the first monochromator, selecting the illumination wavelength. The luminescent sample is placed in the illumination bundle. From the emitted radiation one wavelength is selected by the second monochromator, after which it hits an detector.

which is recorded by the ccd camera. Additionally, a filter can be placed in front of the detector to avoid registration of higher harmonics present in the lamp spectrum. A full setup description is given by Bos et al. [47].

3.3 Excitation measurements

After having measured the emission spectrum of a sample, it is possible to measure the excitation spectrum for one of the the previously obtained emission peaks of the sample. The excitation spectrum gives the emission at one wavelength as function of excitation wavelength. The basics of the excitation measurements are very similar to these of the emission measurements, i.e. the same setup is used. Again the 450 Watt Xenon-lamp source is used, but instead of fixing the excitation wavelength, the emission wavelength is fixed at the position of the emission peak. The first monochromator selects one wavelength at a time, and illuminates the sample step by step with a different wavelength, see table 3.2. The second monochromator selects the wavelength of the emission peak.

As the spectrum of the lamp is not uniform in intensity, the obtained spectrum is corrected for the spectrum of the lamp. Additionally a filter can be placed behind the first monochromator to avoid illumination by higher harmonics present in the lamp spectrum.

Table 3.2: Example of settings for emission and excitation measurements on a Lu_2O_3:Eu^{3+} film.

	Excitation [nm]	**Emission [nm]**
Emission spectrum	250	400-800 increase by 1
Excitation spectrum	200-560 increase by 1	611

3.4 Luminescent quantum efficiency

An important factor in the quality of luminescent materials is the luminescent quantum efficiency (LQE), see section 2.3.2. The LQE is is defined as the ratio of the number of photons emitted to the number of photons absorbed.

A convenient way to estimate the LQE is by comparing the luminescent decay times of the luminescent material and a reference material. The reference should be of course of the same material, but with a low dopant concentration and at low temperature. This ensures that there is no concentration or thermal quenching in the reference measurement.

The luminescent decay time is the characteristic time in which the intensity of luminescent light decays after a pulse of illumination of the luminescent sample. It is difficult to measure this decay directly, therefore so called time-correlated single photon counting is used, which is well described by Bollinger and Thomas [48].

The basic principle is as follows. One flashes with a light source on a luminescent sample, causing the sample to emit photons, which are detected by a detector. Now the source intensity is turned down till per flash (start) only one photon is detected by the detector (stop). The time between the start and the stop is recorded by a time to digital converter (TDC). Repeating this measurement many times gives the probability curve for measuring a hit after a certain time. This principal is depicted in figure 3.5.

There is one problem at this stage, which is that if the intensity is too high there will be more fast stops. Unless the intensity is so low that per start less than one stop is registered, this results in a bias for short start-stop separation times, which results in a systematic statistical error in the measurement. results in long measuring times in order to obtain enough hits to have a statistically sound result.

A solution is to detect whether stops are detected after the first stop. If so, one can decide to reject such measurement. This is the so call single-hit method, ruling out the bias for short times.

An even better method is described by Moses [49], which is based on the multi-hit TDC. This TDC can digitize multiple stops, and thereby significantly increase the measurement speed. Next to this, the TDC can still reject measurements with $n + 1$ stops if the TDC can only digitize n stops.

Figure 3.5 schematically shows the used setup for this research. At the right bottom the Xenon flash lamp is depicted. This lamp is triggered by a 50Hz pulse generator, which also sends the start signal to the multi-hit TDC (LeCroy 4208). The flash illuminates the sample, which emits light into the monochromator (Jobin Yvon H10). The light of the selected wavelength passes through towards the channel photomultiplier (CPM), which detects the photon and sends a stop signal to the TDC. The TDC returns the timestamps of the digitized stops.

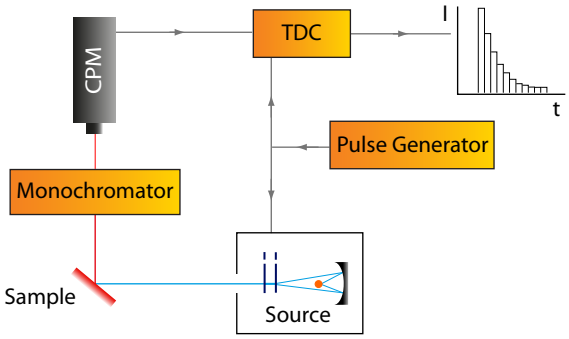

Figure 3.5: Schematic view of the time-correlated single photon counting setup. The purple line is the polychromatic light coming from the Xenon lamp, the blue line is the polychromatic light coming from the luminescent sample, the red line is the monochromatic light coming through the monochromator. The CPM is the channel photomultiplier.

3.5 Light transport efficiency

Measuring transport efficiencies in thin films has been done for many decades. Mostly this is done in the context of data signal transport. [35, 37, 50] In order to prevent dispersion of the data, single mode waveguides are used for this purpose mostly, see section 2.2.1.2. Most of the techniques used to measure the transport losses involve prism coupling[1], in which light is coupled in the film using a prism, see section 3.5.1. In the case of LSCs however, not a single mode is considered, but all plus the substrate modes. An already available way to couple the light in the LSC is to use a laser to excite the luminescent material, this method is described in section 3.5.2.

3.5.1 Prism thin film coupled waveguide loss measurements

As described in section 2.3.6 the intensity of light trapped inside a waveguide decreases exponentially as it travels along the waveguide. This is due to scattering or self-absorption. To measure this decay it is desirable to couple a laser into the waveguide. One way to do that is to use a coupling prism [35–37, 50], as depicted in figure 3.7. A laser beam is incident on the prism, in which it is refracted according Snell's law, equation 2.9. Then the beam is coupled into the LSC, again undergoing refraction. None of the angles shown in figure 3.7 exceed a critical angle, i.e. the beam will transit al interfaces. Nevertheless, angle θ_t exceeds the critical angle of the film-air interface, therefore undergoing total internal reflection, thus being trapped inside the film.

Figure 3.6 shows the total coupling setup. Now the laser light has been trapped inside the film, multiple options are available to measure the attenuation of the trapped light. Option 1 given in figure 3.6 shows the possibility of measuring along the waveguide with a CCD or a fiber bundle [37], or with

[1] Tien et al. [51] describe even more techniques including grating coupling and side coupling

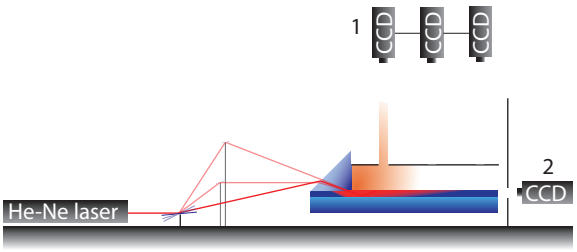

Figure 3.6: Prism coupling setup with attenuation measurements in two different ways.

a photograph [35, 50]. Option 2 shows a setup where the intensity is monitored at the end of the waveguide. In this case the position of the prism coupling has to be varied. The latter is hard to achieve as the coupling changes every time it is replaced. The light has to tunnel through the air or optical coupler between the prism and the film, the efficiency of tunneling strongly depends on the coupling pressure applied to the prism. Attenuation setups are commercially available, e.g. at Metricon Corporation [52].

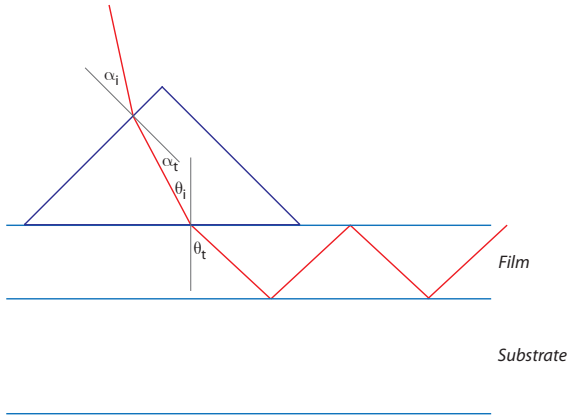

Figure 3.7: Schematic representation of the prism coupling setup. The laser beam comes from above, refracted inside the prism and refracted inside the thin film of the LSC. None of the angles α_i, α_t, θ_i, and θ_t exceed a critical angle. Whereas the θ_t exceeds the critical angle between the film and air.

With such setups however only one waveguide mode at a time is excited. In the case of LSCs it is desirable to measure the effect of all waveguide and substrate modes. This can be done using laser excitation, which is explained in section 3.5.2.

3.5.2 Laser excited waveguide loss measurements

In order to excite all modes of the LSC at once, one can make use of the principle idea behind the LSC, i.e. absorption, emission and trapping light. The principle of measuring the attenuation upon excitation has been proven to be be a working procedure by Earp et al. [14]. The setup used in this research differs little from the one used by Earp et al. Instead of a linear

source a point source is used in this research. This is done for two reasons, first, a point source is available ,and second, on a small sample as used in this research the line source is less predictable than the point source.

A schematic representation of the used setup is shown in figure 3.8. The LSC is fixed between two hollow clamps. The 250 nm excitation beam illuminates the LSC through the hollow clamp to prevent any stray light from reaching the optical probe. The optical probe is positioned very close to the surface of the LSC. The intensity of the scattered light is monitored along r. The probe is connected to a Ocean Optics QE65000 Czerny-Turner spectrometer, making it possible to measure spectrally resolved, which assures that only light from the LSC is measured.

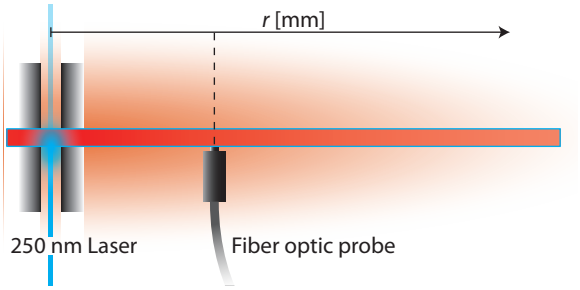

Figure 3.8: Schematic representation of the laser excited attenuation measurement. The laser beam excites the LSC through a hollow clamp. With a fiber optic probe the scattered luminescence is measured along r.

3.5.3 Directional output measurements

In order to discern between the losses in the film and the film-substrate-complex a more advanced measurement is performed, i.e. the directional output measurement.

The setup used is relatively simple and is shown in figure 3.9. The LSC is excited in one point with a 250 nm tunable laser. The LSC is positioned such that only the light emerging from the outcoupling surface can be detected by the photodiode (International Radiation Detectors Inc. model SXUV20BNC). The photodiode is placed 1.2 meters from the LSC, making the LSC a point source, as the LSC thickness is $3-4$ orders of magnitude smaller. The photodiode is placed at the end of a long tube with some apertures inside, to narrow the viewing angle of the diode.[2] The photodiode is connected to a Keithley 6517A current meter, which monitors the current while the angle θ is changed. Before every measurement a Thorlabs S120UV power meter is placed in the excitation beam to monitor the laser power. At the same time a dark measurement is performed with the photodiode without laser excitation. In the figure the output profile, which is to be determined, is plotted in red.

[2]Pravettoni et al. [53] have done similar directional measurements. They, however, did measurements close to the LSC. Then the LSC cannot be seen as a point source, excluding the possibility of describing the output analytically.

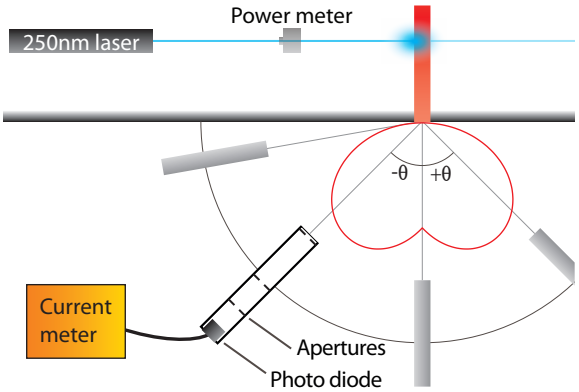

Figure 3.9: The setup for measuring the output profile. The LSC is illuminated by a 250 nm laser. The power meter monitors the laser power in between measurements. The current of the photodiode measured as a function of angle θ. The profile in red is the expected ideal output profile.

Chapter 4

Samples

During the experiments two LSCs have been used, which are displayed in figure 4.1. In this chapter the fabrication process, the further treatments and the dyeing of the samples is explained.

The material properties of the two samples of figure 4.1 are listed in table 4.1.

Table 4.1: LSC material properties.

Figure 4.1:	Left	Right
Substrate:	c-cut Al_2O_3	c-cut Al_2O_3
Thickness substrate:	3 mm	250 μm
Diameter:	5 cm	5 cm
Film:	Lu_2O_3:4%Eu^{3+}	Lu_2O_3:8%Eu^{3+}
Thickness film:	3 μm	3 μm

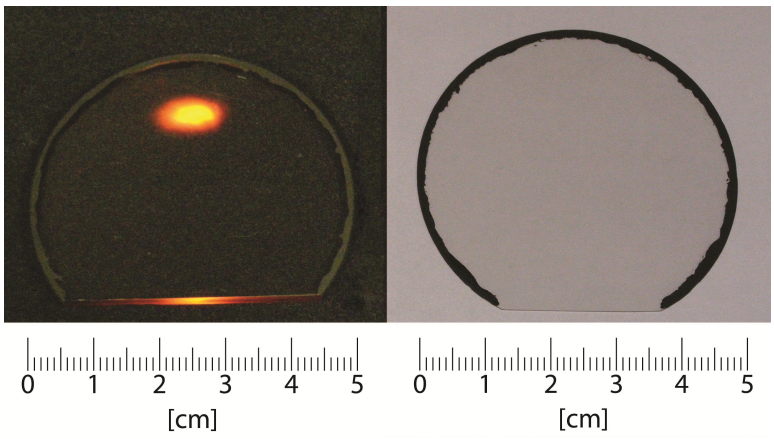

Figure 4.1: Two samples. The left sample is a 3 mm thick Al_2O_3 substrate with a 3 μm Lu_2O_3:8%Eu^{3+} film on both sides of the substrate. The right sample is a 250 μm thick Al_2O_3 substrate with a 3 μm Lu_2O_3:4%Eu^{3+} film on both sides of the substrate. The left concentrator is excited with a 250 nm laser, showing the light transport through the LSC. The round edges have been dyed black.

4.1 Fabrication & treatment

The LSC samples have been produced by Boston Applied Technologies, Inc. The substrates were made of c-cut Al_2O_3 (sapphire) with thicknesses of 3 mm and 250 μm. The Lu_2O_3:Eu^{3+} films were applied using a dip-coating technique[1]. The films have an europium concentration of 4% and 8% for the 3 mm and 250 μm thick substrates respectively. The exact procedure, of dipping coating and annealing is unknown.

Before measurements can be performed a few processing steps are taken. First, as the 3 mm sample was circular, it needed to be diamond sawn to produce one straight edge.

The edge is wet polished afterwards, using Silicon Carbide 500 grit sandpaper. The straight edge of the 250 μm LSC is polished as well, as at that edge a layer of Lu_2O_3:Eu^{3+} was deposited during the dip-coating. The Mohs hardness of Al_2O_3 is about 9[2], whereas the hardness of the Lu_2O_3:Eu^{3+} film is only about 6. [54] This has serious consequences during polishing. A thin substrate can be polished with relative ease, a thick substrate, like the 3 mm one, takes significant amounts of time. Furthermore, due to the difference in hardness between the substrate and the film, it is likely to polish away more of the film than of the substrate. This can have serious implications for the directional output profile from section 2.3.8.

Finally, the samples were cleaned with ethanol and acetone to remove any dirt ended up on the samples during the processing.

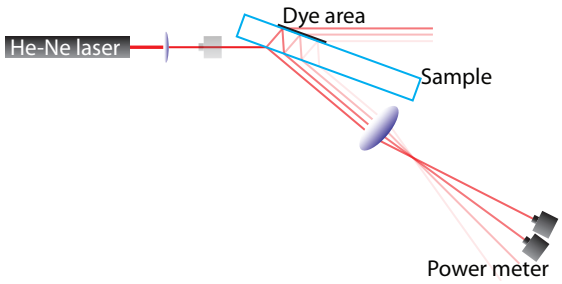

Figure 4.2: Schematic representation of the dye absorption measurement setup.

4.2 Dyeing

The edges of the LSC act as mirrors for the internally trapped light. To avoid measuring effects caused by the edges the light needs te be coupled out at the edges and be absorbed. To do so, at the edges a layer of Revell #8 matt black dye was applied. As the refractive index of the dye exceeds the refractive index of the LSC the light is able to refract into the dye and be absorbed.

[1] Though the film is deposited on both sides of the substrate, all previous theory based on a single film is still applicable due to the symmetry of the analysis.

[2] As reference diamond has a hardness of 10, Silicon Carbide about 9, and glass about 6.

To verify the effect of the dye a small experiment was performed as shown in figure 4.2. A He-Ne laser beam[3] is incident under an angle on an 3 mm Al_2O_3 substrate. Part of the light is reflected at the air-Al_2O_3 interface (zeroth order reflection), part after refraction into the substrate at the Al_2O_3-air interface (first order reflection). When a layer of the black paint is applied at the reflection spot at the Al_2O_3-air interface, the power of the first reflected bundle should stay the same, whereas the second bundle will (partially) be absorbed by the dye.

In figure 4.2 the setup is depicted schematically. The picture also shows the addition of two lenses. The first lens is to focus the bundle to be able to separate the exiting bundles. It is obvious that all reflected bundles (with and without refraction through the LSC) will leave the LSC parallel. The separation of these bundles is dependent on the thickness of the substrate and the angle of incidence. In the case of the 3 mm substrate and an angle of incidence of about 65° the separation is only in the order of a millimeter. Therefore a second lens was added to separate the bundles.

The results of this measurement are given in table 4.2. As can be seen, the power of the 1^{th} order reflection drops significantly. Where the laser power and 0^{th} order reflected power stay as good as the same, less than 4% of the power of the 1^{th} order reflection remains.

Table 4.2: Results of the dye absorption measurement.

Power:	**Laser [mW]**	0^{th} **order [mW]**	1^{th} **order [μW]**
No dye	7.46	1.14	486
Revell #8 matt black	7.44	1.13	18.0
No tape	7.67	1.49	715
Black tape	7.57	1.49	38.7

The same experiment has been performed with black tape instead of black dye. The results presented in table 4.2 show similar absorption of something less than 96%. The tape, however, reflects the light more diffuse, lowering therefore the amount of measured light at 1^{th} order reflection. The dye on the other hand does hardly reflect diffusely, but absorps the light. This effect is shown in figure 4.3, where on the left the sample with dye is shown and on the right the sample with tape. In contrast to the dyed sample a glow emerges from the tape where it is thoroughly applied to the sample.

[3]The 633 nm light of the He-Ne laser closely resembles the 611 nm emission of the Lu_2O_3:Eu^{3+} film.

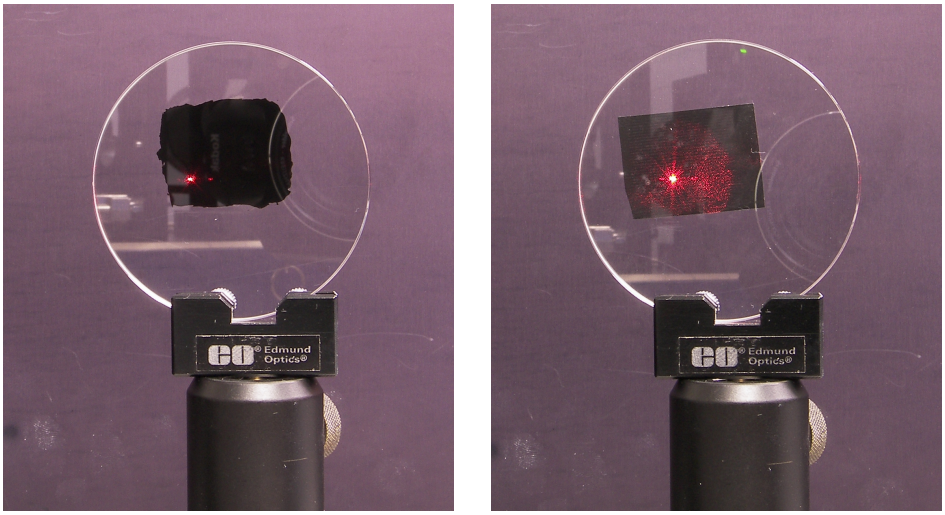

(a) (b)

Figure 4.3: The dyed (a) and taped (b) sample, clearly showing the difference between the two absorbing media. Both pictures have been taken with similar aperture, ISO value, and exposure time.

Chapter 5

Experimental results

5.1 Light harvesting

5.1.1 Reflection measurements

The relatively trivial reflection measurement has been performed using the setup described in section 3.1.1. At an angle of about three degrees a reflection of 10.0% with a readout uncertainty of 0.2 percentage point was measured. So 10.0% is lost due to reflection at the surface of the LSC.

5.1.2 Transmission measurements

The transmission spectra of the Lu_2O_3:Eu^{3+} thin films have been measured with the two setups described in section 3.1.2: first the 'Bruker Vertex V70' and second the 'AvaSpec' setup. Without going in to much detail, in both figure 5.1 and figure 5.2 the absorption by the CT-band around 250 nm is very clear. The transmission outside the CT-band is roughly $80 - 85\%$.

The measurements with the Bruker and the AvaSpec have been performed according to the measurement descriptions in sections 3.1.2.1 and 3.1.2.2. The resulting data is shown in figures 5.1 and 5.2. As at 250 nm 12% is transmitted and 10% is reflected, about 78% of the not reflected light is absorbed. This results in a luminescent harvesting efficiency, η_{LHE}, of about 87%.

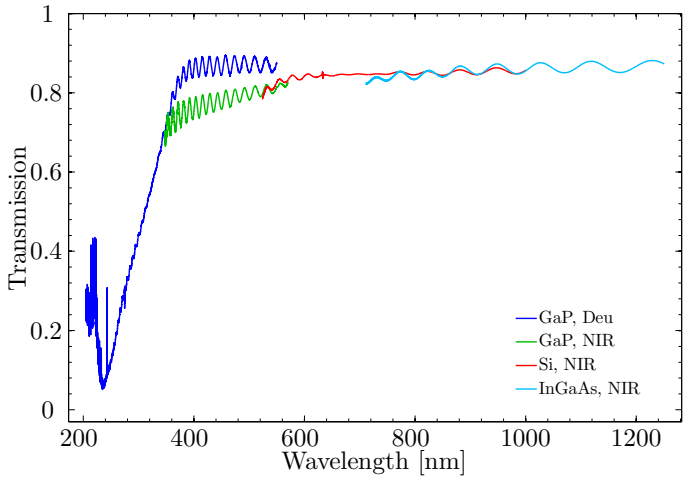

Figure 5.1: Transmission spectrum of the Lu_2O_3:Eu^{3+} thin film on the 250 μm substrate measured with the Bruker setup.

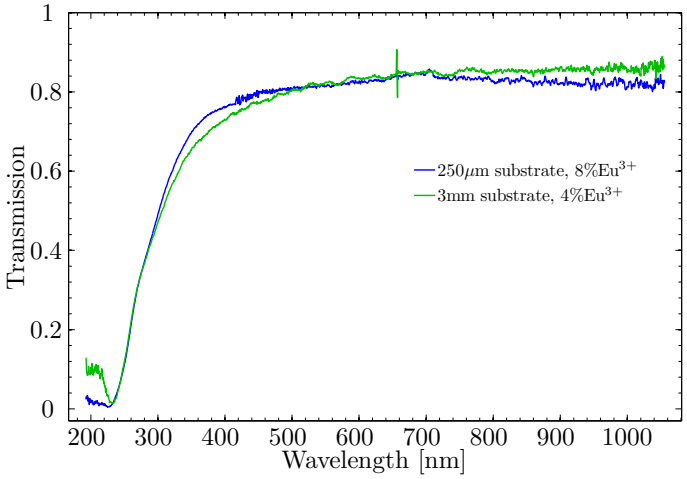

Figure 5.2: Transmission spectrum of the Lu_2O_3:Eu^{3+} thin film on the 250 μm and 3 mm substrates measured with the AvaSpec setup.

5.2 Self-absorption

The experiments for the emission spectrum were performed according the method described in section 3.2 for the wavelengths given in table 3.2. The results are shown in figure 5.3. The measurement of the 250 μm sample was obtained using the Ocean Optics QE65000 spectrometer. The spectral resolution of the setup shown in figure 3.4 is higher, therefore showing more details in the spectrum. In combination with the absorption spectrum it easily seen that there is no self-absorption.

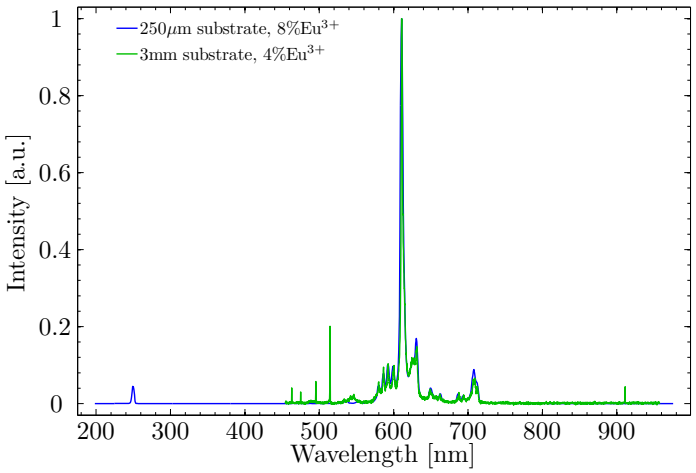

Figure 5.3: Emission spectrum of Lu_2O_3:Eu^{3+}. Excitation in the CT band at 250 nm.

5.3 Excitation measurements

According to the method described in section 3.3 the excitation spectrum of Lu_2O_3:Eu^{3+} is obtained and shown in figure 5.4. In this measurement filter 'OC14' was used, which has a cutoff wavelength around 580 nm for shorter wavelengths, see for the specification the inset in figure 5.4.

5.4 Luminescent quantum efficiency

Using the setup described in section 3.4, the decay curves of the Lu_2O_3:Eu^{3+} have been measured. The results are plotted in figure 5.5. The red dashed line is the single exponent of non-quenched Lu_2O_3:Eu^{3+}, with a decay time of 1 ms [55, 56]. The data cannot be fitted with a simple single exponent. Zych et al. [57] reported similar results, of nonexponential behaviour and short decay times. In order to fit the data properly, the fit has the form of a triple exponential decay given by equation 5.1. The resulting fit parameters are given in table 5.1.

$$f(t) = A_1 e^{-\frac{t}{\tau_1}} + A_2 e^{-\frac{t}{\tau_2}} + A_3 e^{-\frac{t}{\tau_3}} \tag{5.1}$$

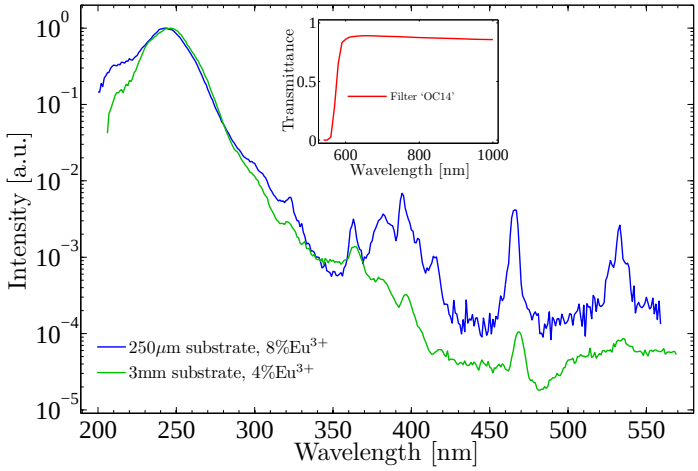

Figure 5.4: Excitation spectrum of Lu_2O_3:Eu^{3+}. Emission of the 611 nm line. Inset: Transmittance of filter 'OC14'.

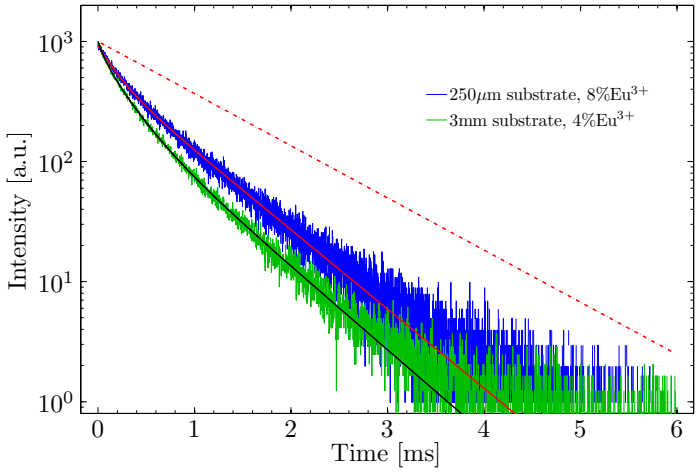

Figure 5.5: Luminescent decay curve of Lu_2O_3:Eu^{3+}. Emission of the 611 nm line.

Using the surfaces underneath the decay curves the quantum efficiencies can be determined to be 43.8% and 33.6% for the 250 μm sample and the 3 mm sample respectively.

Table 5.1: Values of the fitting parameters of equation 5.1 on the time resolved luminescence data of figure 5.5.

	A_1	τ_1 [μs]	A_2	τ_2 [μs]	A_3	τ_3 [μs]
8%Eu^3+	564	658	366	182	−−	−−
4%Eu^3+	326	626	496	245	180	59.7

5.5 Light transport efficiency

5.5.1 Linear attenuation measurements

The linear attenuation lengths have been measured two times for the 3 mm substrate sample; at two different trajectories over the LSC. The results for both samples is given in figure 5.6. As explained in section 2.3.6, the intensity will drop exponentially as a function of distance from the laser spot. But not only that, due to measuring the intensity from a point source which is spreading out, the intensity will decrease with $1/r$ as well. The single $1/r$ is fitted to the 250 μm sample, which is the dashed curve in figure 5.6.

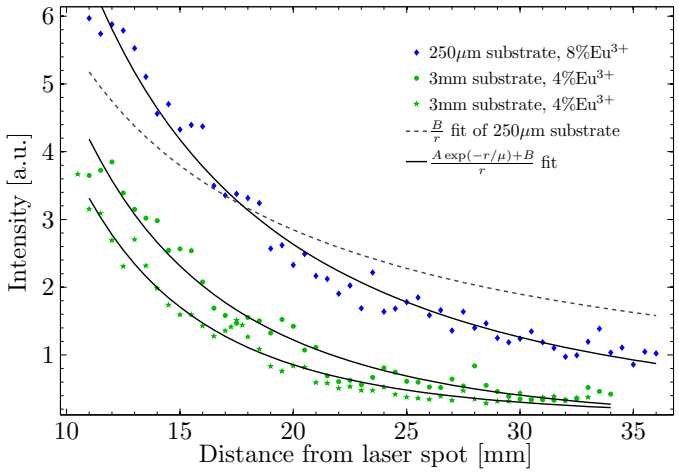

Figure 5.6: Luminescence intensity attenuation as a function of distance from the laser spot for the different samples.

All data sets have been fitted with equation 5.2, of which the fitting parameters are given in table 5.2. A is an intensity parameter of the scattered light from the film and B is the intensity parameter of the scattered light from the substrate. As it is possible to fit the data without an exponential attenuation for the substrate it is assumed that the attenuation in the substrate is longer than can be measured on the 5 cm sized sample.

$$f(t) = \frac{Ae^{-\frac{r}{\mu}} + B}{r} \tag{5.2}$$

Table 5.2: Values of the fitting parameters of equation 5.2 on the linear attenuation data of figure 5.6.

	A	μ [mm]	B
250 μm sample	100	24.6	8.38
3 mm sample	100	14.0	0.470
3 mm sample	100	9.60	4.66

5.5.2 Directional output measurements

The directional output measurements will be treated separately for the two different samples, as the results are very diverse. In the sections 5.5.2.1 and 5.5.2.2 the results of respectively the 250 μm sample and the 3 mm sample will be discussed.

5.5.2.1 250 μm sample results

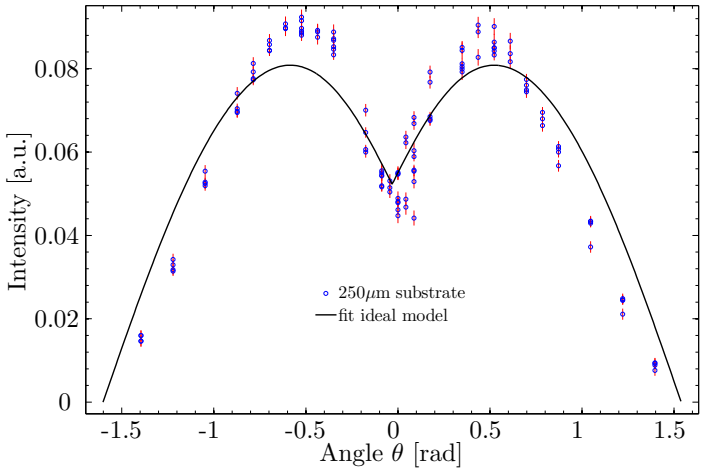

Figure 5.7: The measured directional output profile of the 250 μm sample. In black the ideal output profile is fitted to the data.

Figure 5.7 shows the results of the directional output measurement. In black the ideal output model, given by equation 2.53, is fitted. As predicted in section 2.3.8.3 the ideal model does not fit the data adequately.

Figure 5.8 shows the same data with fits using the extended model. This model takes into account that part of the light is lost due to scattering while transported to the outcoupling surface, and that part of the light is reflected back into the LSC at the outcoupling surface. Both fits, the ideal and the extended, can be found in Appendix F. The values of the fit parameters can be found in table 5.3.

As can be observed in figure 5.8, the extended model gives a good fit to the data. However, one could argue that the coefficients A and B from equation 2.56 should be the same. That can be understood by considering the intensity at the position where the laser excites the luminescent material. At that point the exponent of the extended model is unity, therefore the intensity of both the film and the substrate should be scaled by the same laser intensity dependant factor A, or P_0 from equation 2.47. If we apply the constraint that $B = A$ figure 5.8 shows that the fit becomes worse.

Even though the fit was best when B equals A, things have worked out reasonably fine. The measurements, however, were performed again to better define L, the distance between the excitation point and the outcoupling surface, during the measurements. L is schematically shown in figure 2.28.

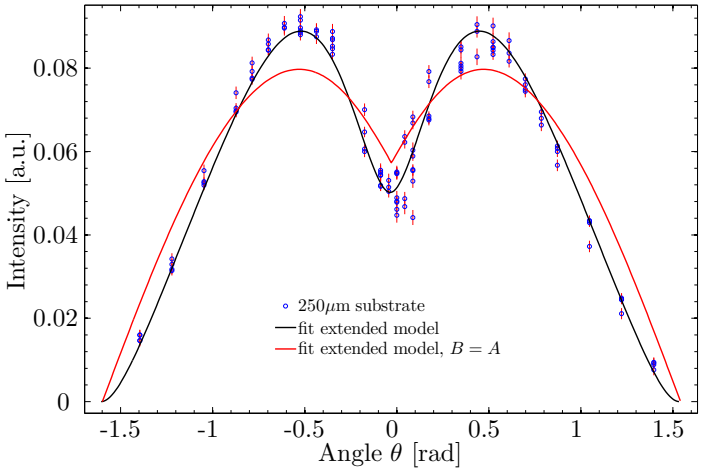

Figure 5.8: The measured directional output profile of the 250 μm sample. In blue and black the extended model with and without equal coefficients is fitted to the data.

Table 5.3: Values of the fitting parameters of equation 2.56. For the fits thicknesses h_{sub} and h_{film} of 0.003 mm and 0.125 mm are used.

	A	$\tilde{\mu}_{sub}$	B	$\tilde{\mu}_{film}$	$\Delta\theta$ [rad]
Ideal	2.99	$--$	2.45	$--$	0.031
Extended	13.5	75.1	2.62	351	0.036
Extended, $B = A$	2.69	506	2.69	∞	0.029

In the former measurements a spot size of the order of a centimeter was used, whereas in the later measurements a sub-millimeter spot size excited the luminescent material. The results are shown in figure 5.9. One observes immediately an asymmetry in figure 5.9(a) for all measurements. The asymmetry reverses when the sample is rotated 180° in the ϕ-direction, as shown by the '$L = 1.3$ cm, rotated sample' measurements. Furthermore, a measurements with $L = 1.3$ cm and $L = 3.5$ cm are shown. One would expect a change in proportion in the peak-intensity and the dip-intensity, as the dip-intensity is only dependent on the film losses. In the discussion, chapter 6, I will go into this in more detail. In figure 5.9(b) the same data is shown, but normalised at 35°, in order to see any differences in proportions.

The edges of the LSC have been inspected using a Leica Wild M3Z stereo microscope with a $40\times$/6B Wild 445303 ocular. During inspection the LSC was illuminated with the 250 nm laser. The resulting views are given in figure 5.10.

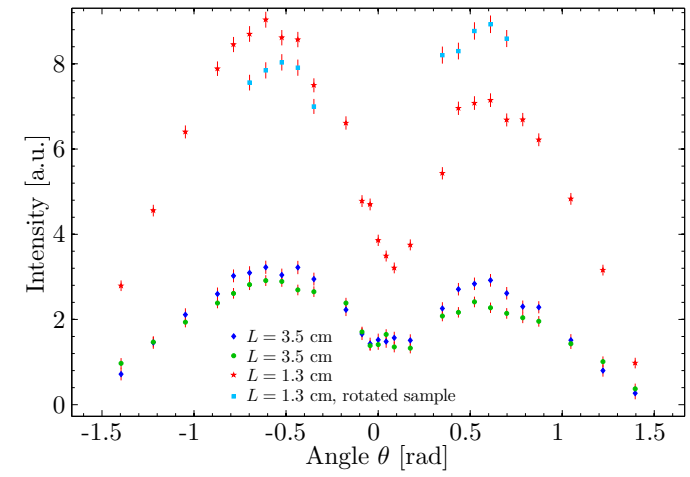

(a)

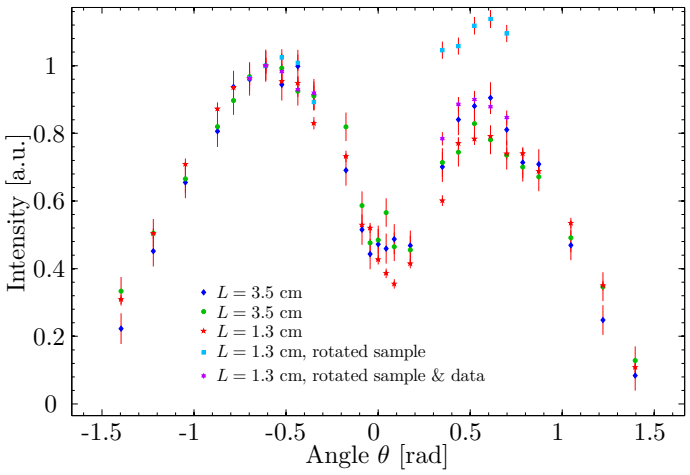

(b)

Figure 5.9: Directional output measurements for different excitation distances L, see figure 2.27. Figure (a) shows the increase in intensity for shorter L. Figure (b) shows the same data, but normalized at $35°$.

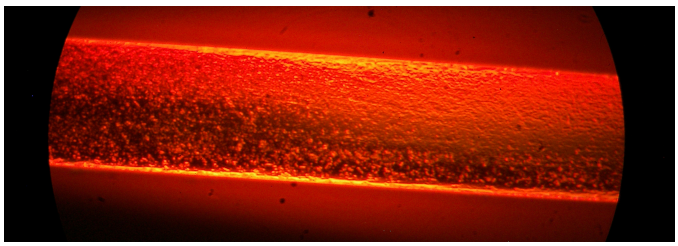

(a)

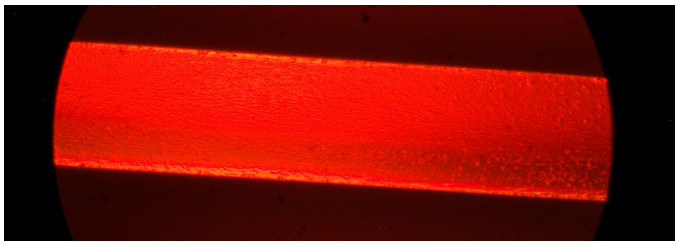

(b)

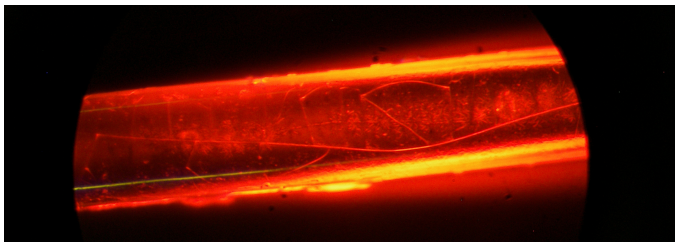

(c)

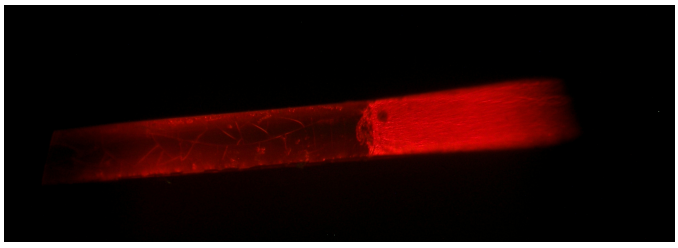

(d)

Figure 5.10: (a) shows the edge of the LSC with substrate thickness of 250 μm. L is close to zero. (b) shows the edge for larger L. (c) shows the round edge of the LSC. Here the film is not removed. (d) shows the border between the edge with the film (Left) and the polished edge (Right) of the LSC.

5.5.2.2 3 mm sample results

It was decided not to show the results of the directional output measurements of the 3 mm sample. No consistency in the output profile could be found during these measurements, which can easily be explained by visual inspection of the sample while excited by the laser.

Figure 5.11 shows a picture taken of the outcoupling surface. One clearly observes at the top right large chips missing, which is caused by the diamond sawing. At the left this effect is relatively mild, and could therefore be used for a directional measurement. The surface itself, however, is rough. The objective of the polishing, described in chapter 4, was to remove this roughness. The combination of the hardness of the substrate and the capacity of the polishing machine made it impossible to remove the irregularities on the edge of the 3 mm sample on a reasonable timescale.

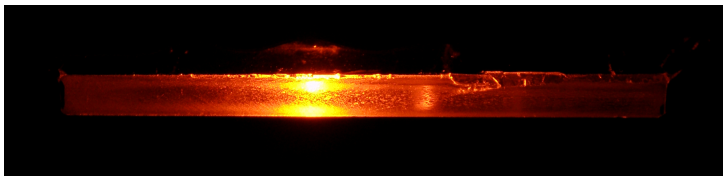

Figure 5.11: Picture taken of the outcoupling surface, during excitation of the LSC with a 250 nm laser, clearly showing the roughness of the surface.

Chapter 6

Interpretation and Discussion

In this chapter I will discuss the results presented in chapter 5 in the context of previously developed theories. At the end of this chapter I will come up with the determined optical efficiencies of the in this research used LSCs, and will discuss their meaning and relevance.

6.1 Light harvesting

To calculate the light harvesting efficiency both the transmission and the reflection are needed. The reflection was determined to be 10.0%, which is significantly lower than the calculated 13.3% using Fresnel's equations and a refractive index of Lu_2O_3 of 2.145 at 250 nm. This difference however could be due to a change of orientation of the power meter in the laser bundle.

More interesting to discuss are the transmission measurements. The two setups, the Bruker and the AvaSpec, show an interesting difference, see figures 5.1 and 5.2. In the transmission spectrum obtained with the Bruker setup clear interference patterns are observed. This interference is caused by the thin film, and is described by Vasicek [58]. The maxima are given by equation 6.1.

$$2nT\cos\theta_t = m\lambda \tag{6.1}$$

The refractive index, n, is taken to be according equation 6.2, determined by Medenbach [59], with λ the wavelength in micrometers. Then the results correspond closest to a thickness T of 3.25 μm, which is indeed in close correspondence to the 3 μm the manufacturer gave.

$$n = \sqrt{1 + \frac{\lambda^2}{0.3833\lambda^2 - 0.0066}} \tag{6.2}$$

The reason that the interference is not observed in the measurements with the AvaSpec setup is due to the geometry of the light bundle. The bundle in the Bruker is fairly parallel, whereas the bundle of the AvaSpec is not parallel per se.

Furthermore in figure 5.1 a bad line-up of the GaP detector measurements with the deuterium and the tungsten sources is observed. If we look at the transmission spectrum made with the AvaSpec setup, we should conclude that there is an offset in the deuterium source measurement. This offset could be due to warming up of the lamp. The reference spectrum (without a sample) has been made before the actual measurement. If in the mean time the lamp has warmed up the lamp‘s intensity could be increased, explaining the offset.

A stranger phenomenon is observed in the transmission spectra obtained with the AvaSpec setup, figure 5.2. As both films of the 250 μm and the 3 mm samples are equally thick, namely 3 μm. A change in transmission is expected as the concentration of the optically active material europium has decreased by a factor two. A change in concentration should inevitably appear in the transmission spectrum. Whether the concentration has been lowered as the manufacturer has reported could therefore be questioned.

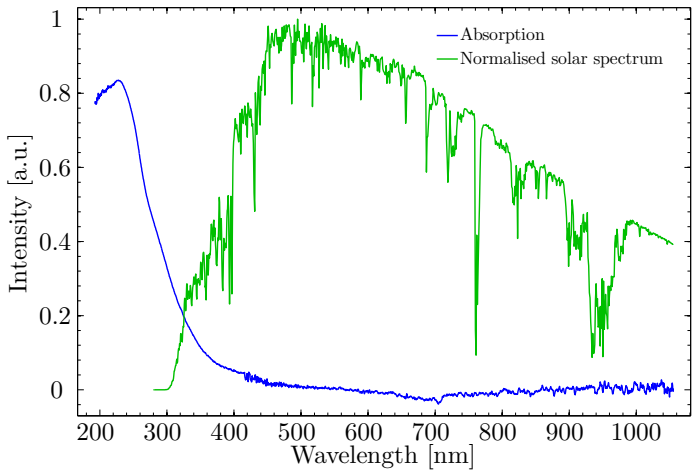

Figure 6.1: Absorption spectrum of Lu_2O_3:Eu^{3+} with the normalized solar spectrum, showing barely any overlap.

Nevertheless, the transmission measured at 250 nm is 12.0%. Combined with the reflection of 10.0%, this results in a light harvesting efficiency, η_{LHE}, of 78%. If the theoretical reflection is used, the LHE decreases slightly to 75%.

If we would like to use this LSC as a solar concentrating device, the LHE at 250 nm is not of any interest. Therefore the absorption spectrum is plotted along with a normalised solar spectrum in figure 6.1. This figure shows that there is only little absorption of the sunlight, making this very device unsuitable for solar concentration. This is exactly as expected, as the intension was to have a non-self-absorbing LSC to study the transport efficiency separated from the self-absorption.

6.2 Self-absorption

The emission spectrum of Lu_2O_3:Eu^{3+} is clearly located outside its own absorption spectrum, see respectively figure 5.3 and figure 6.1. The various absorption peaks are produced by the transitions given in table 6.1.

Table 6.1: Transitions in the emission spectrum of Lu_2O_3:Eu^{3+}.

Wavelength [nm]	Transition
580	$^5D_0 \rightarrow ^7F_0$
586	$^5D_1 \rightarrow ^7F_3$
593	$^5D_0 \rightarrow ^7F_1$
601	$^5D_0 \rightarrow ^7F_2$
611	$^5D_0 \rightarrow ^7F_2$
630	$^5D_1 \rightarrow ^7F_4$
650	$^5D_0 \rightarrow ^7F_3$
662	$^5D_1 \rightarrow ^7F_5$
688	$^5D_0 \rightarrow ^7F_4$
708	$^5D_1 \rightarrow ^7F_6$

The dominant peak in the emission spectrum is located at 611 nm resulting from the $^5D_0 \rightarrow ^7F_2$ transition. In figure 5.3 the very narrow peaks from the $^5D_2$ emission are only visible for the 3 mm sample, due to a higher spectral resolution in this measurement. However, one could also argue that, due to the lower concentration, the cross-relaxation from the $^5D_2$ level to the $^5D_0$ level is less efficient. This would result in more emission from the $^5D_2$ level to the ^7F levels. The peak at 250 nm is the laser light used for excitation. This clearly shows the large Stokes' shift from 250 nm to 611 nm, preventing self-absorption. This large shift has serious consequences for the Stokes' efficiency, η_{Stokes}, which is only 41%.

The total absorption and emission process is displayed in figure 6.2. The absorption of the UV-photon corresponds to the transition from the valence band to the Eu2+ ground state (1) by charge transfer. Next, the centre relaxes to a ^5D_n level non-radiatively (2). If in a higher ^5D level, the centre relaxes to the $^5D_0$ level either via multi-phonon relaxation[1] or via cross relaxation (3). The cross relaxation scheme [57] is $^5D_1 \rightarrow ^5D_0 \leftrightarrow ^7F_0 \rightarrow ^7F_2, ^7F_1 \rightarrow ^7F_3$. These non-radiative processes quench the emission from the $^5D_1$ level. Finally, the $^5D_0 \rightarrow ^7F_2$ transition emits the luminescent photon with a wavelength of 611 nm (4).

[1]The highest phonon energy of Lu_2O_3 is 618 cm^{-1}. [60]

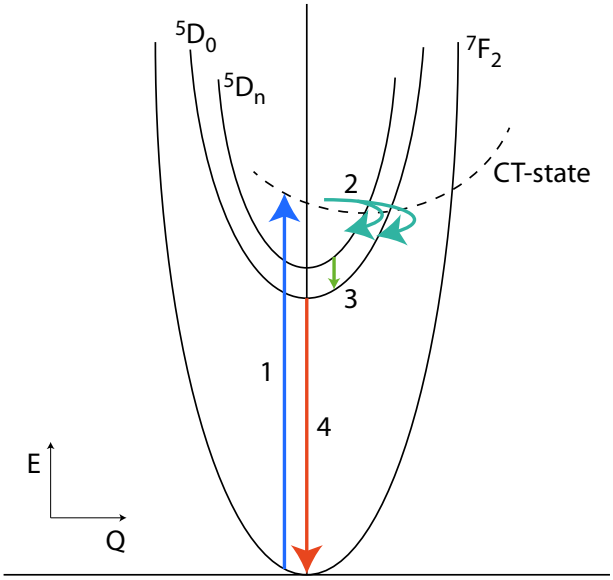

Figure 6.2: [17]**The absorption corresponds to the transition from the ground state to the CT state** (1)**. Next, the centre relaxes to a** ^5D_n **level non-radiatively** (2)**. If in a higher** ^5D **level, the centre relaxes to the** $^5D_0$ **either via multi-phonon relaxation or via cross relaxation** (3)**. Finally, the** $^5D_0 \rightarrow ^7F_2$ **transition emits the luminescent photon** (4)**.**

6.3 Excitation spectrum

The excitation measurements show the expected character of an Eu^{3+} doped material, see figure 5.4. The strong absorption in the CT-band results in strong emission of the $^5D_0$ level by the transition to the $^7F_2$ level. Furthermore, emission is observed when the Lu_2O_3:Eu^{3+} is excited in the higher energy f-levels. The transitions associated with them are enumerated in table 6.2.

Table 6.2: Transitions in the excitation spectrum of Lu_2O_3:Eu^{3+}.

Wavelength [nm]	Transition
533	$^7F_1 \rightarrow ^5D_1$
466	$^7F_0 \rightarrow ^5D_2$
414	$^7F_1 \rightarrow ^5D_3$
394	$^7F_1 \rightarrow ^5I_6$
382	$^7F_1 \rightarrow ^5G_J$
363	$^7F_1 \rightarrow ^5D_4$
323	$^7F_1 \rightarrow ^5H_J$

The ratio of the CT-band intensity and the f-f line intensity is different for the 250μm sample and tha 3 mm sample. Zych et al. [57] report similar behaviour as function of concentration. They give as explanation that for higher europium concentration energy migration between Eu^{3+} ions increases more with concentration due to the wide spread of the CT states. This migration in turn increases the chance of reaching a quenching site. It is, however, questionable to what extend energy migration occurs between Eu^{3+} ions excited in their CT state, because of its short lifetime.

Furthermore, a decreasing cross-relaxation from the higher ^5D levels to the $^5D_0$ level for lower concentrations, could lower the $^5D_0$ emission intensity. For lower concentration, however, no increase of $^5D_1$ emission is observed in the emission spectrum shown in figure 5.3. In our opinion no satisfactory explanation is given in literature.

More likely, is the possibility of a saturated absorption by the CT band. The 4% doped sample already absorbs almost all light so that increasing concentration will not result in more absorption and therefore more emission. The 4f lines on the other hand do not absorb strongly. An increase in concentration of europium will result in more absorption and therefore in more luminescence. This matches the results shown in figure 5.4.

6.4 Luminescent quantum efficiency

Figure 5.5 shows the time resolved luminescence measurements of both samples. The dotted red line shows the decay of non-quenched Lu_2O_3:Eu^{3+}, with a decay time of 1 ms [55, 56]. Both samples show serious quenching, which follows from the shorter decay times. The luminescent quantum efficiencies can be calculated by dividing the surface area under the quenched decay curve by the surface area under the non-quenched decay curve. This results in LQEs of 43.8% and 33.6%. As the concentration of the 3 mm sample is lower than the concentration of the 250 μm sample, one would expect a slower decay as concentration quenching should decrease. The fact that we do observe faster decay strengthens the possibility that the concentration is not as specified by the manufacturer, as was also suggested based on the absorption spectra. Furthermore, no single exponential behaviour is observed, which would be the case with a simple competing non-radiative relaxation process.

The non-exponential character is due to the availability of quenching sites. Therefor the LQE depends strongly on the preparation method, which was not optimised for the 3 mm sample. As the energy migrates from donor to donor ($D^*+D \rightarrow D+D^*$) it might end in a quenching site where it will relax non-radiatively. This explains in principle only the presence of a faster decay. As some donor sites are not located near to such quenching sites, after a while only non-quenched decay is observed. This results in the non-single exponential behaviour of the decay curve.

6.5 Light transport efficiency

The light transport efficiency, η_t, consists in general out of two separate efficiencies: the self-absorption efficiency η_{SA} and the waveguide efficiency η_{WG}. As concluded from the absorption and emission spectra the self-absorption efficiency is unity and can therefore be ignored. At first sight, the waveguide efficiency can be determined for the LSC based on the linear attenuation measurement.

6.5.1 Linear attenuation

Lets consider the measurements shown in figure 5.6. First of all the attenuation for the 3 mm sample is larger than the attenuation of the 250 μm sample. This could be due to the fact that, as the manufacturer has explained, the production of the film was harder on the tick substrate, as the cooling and heating processes of the sample were harder to control. This could have led to a decrease in film quality. Furthermore, it should be noted that the measurement with the thin sample was performed with a taped edge instead of a dyed edge, which could have led to a different light distribution inside the sample. Nevertheless, from the fits an attenuation length in the order of a few centimeters was determined for all measurements.

The fitting function given in equation 5.1 needs some explanation as well. Instead of the use of two exponents just a single exponent with the addition of a constant was used for the fit. Because the attenuation length of the substrate is expected to be much larger than the attenuation length of the film, one of the two exponents is set to unity. It makes sense to assume that that exponents regards the substrate. The attenuation length of the substrate apparently was too long to observe on such a short sample.

In section 2.3.8.3 it is suggested that the attenuation length is inversely proportional to $\tan\Theta$, which follows from equation 2.54. Θ is the angle between the wave vector of the trapped light and the LSC. This raises the question why a single exponential behaviour is observed. Lets consider the limit of no loss; μ is infinite. If there is no loss, no loss can and will be measured in a linear attenuation measurement. Lets slightly increase the loss. One could consider this like going from $\Theta = 0$ to $\Theta = \delta\Theta$ in figure 2.27. Now losses are weakly observed and the measured intensity is very constant over distance. The further we increase the loss the more intense the measured intensity will be. This could explain why at the first few centimeters only one exponent is observed; the loss due to the luminescence under large Θ dominates the loss due to the luminescence under small Θ. The effect of using the single μ is thus an overestimation of the waveguide losses. In table 6.3 the calculated values for the waveguide efficiency are given for a 5×5 cm^2 and a 1×1 m^2 LSC with the determined attenuation lengths.

Table 6.3: Waveguide efficiencies based on the linear attenuation measurements, calculated with equations 2.42 and 2.43.

μ [mm]	size	$\eta_{WG,film}$	$\eta_{WG,sub}$	η_{WG}
24.6	5×5 cm^2	0.453	1	0.741
24.6	1×1 m^2	0.028	1	0.540
14.0	5×5 cm^2	0.306	1	0.671
14.0	1×1 m^2	0.015	1	0.533
9.60	5×5 cm^2	0.224	1	0.632
9.60	1×1 m^2	0.010	1	0.531

6.5.2 Directional output

First of all I would like to emphasize that the results of the directional measurements were not reproducible, which most clearly followed from the fact that in the first measurement a perfectly symmetric profile was measured, whereas in the second a major asymmetry appeared for the same LSC. The most obvious explanation is that the outcoupling edge is not homogeneous. As the edges wer polished by hand, it is very well possible that some slanting has developed. It should also be noted that the Lu_2O_3 film is less hard than the Al_2O_3 substrate, which can have caused some strange,

or, at least, hard to predict behaviour in the directional output of the film.[2] Unfortunately, we have not been able to determine the exact geometry of the outcoupling surface yet. This could also explain why the extended intensity model with $B = A$ had such a poor fit on the measured data. But before going into detail on the fitting with the extended model, I would like to focus on the results presented in figure 5.9.

What is observed in that data is that the proportion between the intensity at the peaks and at the dip is the same for two different excitation distances L. This is not what is expected, and I will explain why. As the film is so much thinner than the substrate, one would expect more interaction of the luminescence with the waveguide in the film than in the substrate, which results in higher loss per distance traveled in the film than loss per distance in the substrate. If we would excite the LSC at $L = 0$ there is no distance in which loss can occur, so an ideal output profile would be observed (of course corrected for the internal Fresnel's reflections). If the LSC is excited at say $L = 1.3$ cm, the losses in the film should be relatively higher in the film than in the substrate. This would result in a relatively lower position of the dip, as the intensity at $\theta = 0$ is only caused by luminescence coupling out of the film. Exciting even further, say at $L = 3.5$ cm, the dip relatively would be lower even more. This, however, is not what is observed, as can be seen in the normalized data in figure 5.9(b). Figure 6.3 shows the calculated behaviour, where the proportions between the top and dip values indeed has changed.

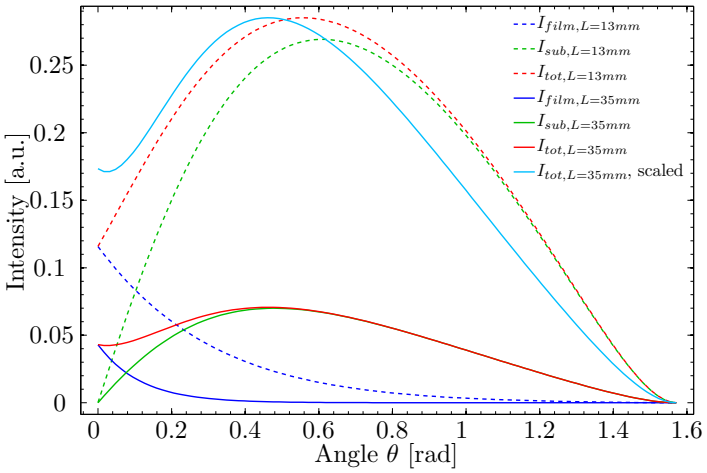

Figure 6.3: The output profiles calculated for two values of L, based on the values of fit parameters of the extended model with $B \neq A$ given in table 5.3.

This observation would either let us to conclude that the intensity at $\theta = 0$ is not coming from the film, but is the result of scattered substrate luminescence, or that both attenuations in the film and the substrate are equal. If we include the pictures taken through the microscope, figure 5.10, we ob-

[2]The picture of the 3 mm sample might be a magnification of the problems that occur, including roughness of the surfaces and edges.

serve light emerging from the films ((a) and (c)). If, however, the illumination spot is place further away from the edge, the emission becomes more homogeneous, and definately emerges from the substrate. This supports the hypothesis that there is significant scattering. If we look at figure 5.10(a), we also see the roughness of the outcoupling surface. In figure 5.10(c) the surface of the film on the edge is shown. This surface is cracked everywhere. Finaly, in (d) the the border between the edge with the film (Left) and the polished edge (Right) of the LSC is shown. Here the disastrous effect of the polishing is shown. This makes it remarkable that the output profile, though not precisely as predicted, is observed at all.

Lets now discuss the fitting with the extended model, where $B = A$. As just mentioned the first reason for the worse fit could be the geometry of the outcoupling surface. There are good reasons to believe that this geometry is not as perfect as required. This is at least confirmed by the asymmetric directional profile. A second problem could be the waveguide modes. As explained in section 2.2.1.2, there is only a finite number of modes supported by the film. This could have influence on the amount of light trapped in the film.

If A and B therefore are allowed to be different we can now calculate the transport efficiency of this LSC based on the values obtained for $\tilde{\mu}_{sub}$ and $\tilde{\mu}_{film}$, using equation 2.57. The results are given in table 6.4. $\tilde{\mu}$ is dimensionless and is related to μ via equation 6.3.

$$\mu = \frac{2h\tilde{\mu}}{|\tan\Theta|} \tag{6.3}$$

Table 6.4: Waveguide efficiencies based on the directional output measurements, calculated with equations 2.57, 2.42 and 2.43.

$\tilde{\mu}_{sub}$	$\tilde{\mu}_{film}$	size	$\eta_{WG,sub}$	$\eta_{WG,film}$	η_{WG}
75.1	351	5×5 cm^2	0.727	0.314	0.531
75.1	351	1×1 m^2	0.106	0.033	0.071

Finally it is interesting to calculate the minimum value for μ. The values of $\mu_{min,film}$ and $\mu_{min,sub}$ are 1.64 mm and 21.0 mm respectively. These lengths are calculated based on the values for $\tilde{\mu}$, h, and the largest value of Θ. The obtained minimum attenuation lengths, especially that of the substrate, are in close correspondence to the directly measured linear attenuation length of 24.6 mm for the same sample. This actually raises the question whether it was legitimate to assume that the measured attenuation length in section 5.5.1 belonged to the film in section 6.5. An attenuation length of 1.64 mm would not be observed as the measurement started at a distance of 10 mm. This explains why only a single exponent is observed. This fast attenuation might be caused by cracks in the surface, like the ones observed in figure 5.10(c). Unfortunately, the light output at the surface of the LSC was not high enough to verify this with the stereo microscope.

6.6 Optical efficiency

Finally, it is instructive to summarize the efficiencies of the various steps involved in the concentration of sunlight. In table 6.5 all determined efficiencies are summarized for both samples.

Table 6.5: Waveguide efficiencies based on the directional output measurements, calculated with equations 2.57, 2.42 and 2.43.

	3 μm Lu_2O_3:8%Eu^{3+} on 250 μm Al_2O_3	3 μm Lu_2O_3:4%Eu^{3+} on 3 mm Al_2O_3
$1 - R$	90%	90%
η_{LHE}	87%	87%
η_{LQE}	43.8%	33.6%
η_{Stokes}	41%	41%
η_{trap}	86%	86%
η_{SA}	100%	100%
η_{WG}	53%[3]	65%[4]
η_{opt}	6.4%	6.0%

The optical efficiency η_{opt} appears to be in the order of 6%. This optical efficiency value is not very useful, as the LSCs were not intended to be real solar concentrating devices, but rather LSCs in which fundamental light transport can be studied without the well-known and studied self-absorption. Though, due to low LQEs, a large Stokes' shift and low waveguide efficiencies, the optical efficiencies are fairly low, one should note that the optical gain of the LSCs are 49.4 and 4.16 for the 250 μm and 3 mm samples respectively. This first high optical gain results in an increase of the power per area solar cell by a factor 2.8. Unfortunately, this is only for illumination by 250 nm light and for an LSC size of 5×5 cm^2.

[3]Obtained with a directional output measurement
[4]Obtained with a linear attenuation measurement

Chapter 7

Conclusions and recommendations

With the aim to investigate the different loss processes in thin film luminescent solar concentrators without self-absorption, it was chosen to use a Lu_2O_3:Eu^{3+} thin film. It was verified that the trivalent europium did not show any self-absorption. In various previous studies on LSCs it was generally assumed that the losses of the trapped luminescence due to reasons other than self-absorption was negligible. Earp et al. indicated that such losses, the waveguide losses, are significant.

In this work is focussed on the waveguide losses, and is successfully tried to quantify them. Based on the attenuation length, it can be calculated how much light is lost during transport. As the attenuation length is dependent on the propagation angle a new directional measurement is developed to measure this attenuation length. With an analytic model and the directional measurement the angle dependent attenuation can be measured. Besides, losses in the film and in the substrate can be discerned as well with this model.

In order to do so an analytic model is derived for the directional outcoupling profile. It has been shown that it is possible to actually measure such a directional profile. The reproducibility proofed not to be obvious. This indicates the possible uncertainties in the geometry of the outcoupling edge, which therefore needs to be improved.

However, with the data obtained from the fit of the model, a waveguide efficiency for our LSC was determined to be 53%. If scaled to a size of 1×1 m^2 the efficiency drops to a poor 7%. This shows the need to consider this loss principle when evaluating LSCs.

With all determined efficiencies an optical efficiency in the order of 6% was determined for both investigated samples. One should note that the optical gain of 49.4 totally makes up for this low optical efficiency. Nevertheless, applicability stays low, as this particular LSC works with absorption of 250 nm and is only 5 cm in size.

Furthermore, the power efficiencies obtainable with LSCs in combination with different solar cells is calculated. For this exercise fictitious luminescent

materials were used, which absorb 80% of the incoming light with an energy higher than the absorption edge. These calculations showed that power efficiencies of up to 16% could be possible.

Though the data obtained with the directional measurements could be fitted well, arguments are given that the fitting parameters A and B do not have to be the same. An explanation given for a difference is the possible influence of a limited amount of supported propagating waveguide modes. To avoid this problem, an LSC with a film of a thickness of the order of 100 times the wavelength of the luminescence in the film could be studied, i.e. $h \geq 100\lambda_0/n_{film}$. If that requirement is satisfied the propagating modes will approximate a continuum, thereby eliminating any interference effects. LSCs with film thicknesses in the order of tens even hundreds of micrometers have already been studied previously [12, 53].

Furthermore, the behaviour of the attenuation length as function of propagation angle is derived. This, however, should be confirmed. One way to do this is by using the prism coupling technique described in section 3.5.1. The laser can be coupled in under different angles. If the attenuation length is determined for these different angles, it is possible to verify the angle dependence of the attenuation length.

Next, I would suggest to determine the exact geometry of the outcoupling edge, as this edge appeared not to be homogeneous. One way could be using SEM or maybe even simpler by fluorescence microscopy. The neat thing of the latter technique is that the luminescent character of the film could be exploited. SEM, however, is better to scan the edge of the film, which is very interesting for the prediction of the output profile caused by the film.

Finally, the use of a glass substrate would make the production a lot cheaper, allowing for larger test samples. Larger test samples would make it possible to do linear attenuation measurements over longer distances, which could reveal the non-single exponential behaviour of this attenuation. An additional pro for glass would be the ease to physically correct any irregularities on the outcoupling surface, due to the relative softness compared to Al_2O_3.

Chapter 8

Acknowledgements

First and most of all I am very thankful to Erik van der Kolk, my dedicated supervisor, for all the support during my research. Erik, not only were you of great help in discussing our new thoughts and theories, but also were you of great support by sharing the pains of endless polishing. Your input, aid and encouragement concerning the participation at the E-MRS conference and the paper we are about to submit have been the most valuable to me.

Furthermore, I would like to express my sincere gratitude towards Johan de Haas, who was always available for great technical advise.

Davy and Bastian, thank you both very much for proofreading my thesis. Your strong and constructive remarks have made a significant contribution to this work.

Next, I would like to thank all students for the entertaining discussions on physics and the mutual support on finishing our thesis projects.

In acknowledgement of making my time at RD&M a wonderful and valuable experience, I would like to thank everybody else at RD&M.

Last of all, my true gratitude to my dear family, who, while suppressing their feeling of non-understanding, have shown to be the most interested and certainly the most supportive.

Bibliography

[1] November 2011. Jetson Green, `http://www.jetsongreen.com/images/2008-small/07/13/solarcellssmall.jpg`.

[2] W.H. Weber and J. Lambe. Luminescent greenhouse collector for solar radiation. *Appl. Opt.*, 15(10):2299–2300, Oct 1976.

[3] A. Goetzberger and W. Greube. Solar energy conversion with fluorescent collectors. *Applied Physics A: Materials Science & Processing*, 14:123–139, 1977.

[4] W.G. van Sark et al. Luminescent solar concentrators – a review of recent results. *Opt. Express*, 16(26):21773–21792, Dec 2008.

[5] J. King Mapel. Organic photovoltaics and concentrators. Thesis (Ph. D.), Massachusetts Institute of Technology, Dept. of Electrical Engineering and Computer Science, 2008.

[6] R. Reisfeld. New developments in luminescence for solar energy utilization. *Optical Materials*, 32(9):850 – 856, 2010.

[7] M.J. Currie et al. High-efficiency organic solar concentrators for photovoltaics. *Science*, 321(5886):226–228, 2008.

[8] J.S. Batchelder, A.H. Zewail, and T. Cole. Luminescent solar concentrators. 1: Theory of operation and techniques for performance evaluation. *Appl. Opt.*, 18(18):3090–3110, Sep 1979.

[9] V. Wittwer, W. Stahl, and A. Goetzberger. Fluorescent planar concentrators. *Solar Energy Materials*, 11(3):187 – 197, 1984.

[10] R. Kinderman et al. I-v performance and stability study of dyes for luminescent plate concentrators. *Journal of Solar Energy Engineering*, 129(3):277–282, 2007.

[11] R. Reisfeld, D. Shamrakov, and C. Jorgensen. Photostable solar concentrators based on fluorescent glass films. *Solar Energy Materials and Solar Cells*, 33(4):417 – 427, 1994.

[12] T. Dienel, C. Bauer, I. Dolamic, and D. Brühwiler. Spectral-based analysis of thin film luminescent solar concentrators. *Solar Energy*, 84(4):1366–1369, August 2010.

[13] W. Wu et al. Hybrid solar concentrator with zero self-absorption loss. *Solar Energy*, 84(12):2140 – 2145, 2010.

[14] A.A. Earp, G.B. Smith, P.D. Swift, and J. Franklin. Maximising the light output of a luminescent solar concentrator. *Solar Energy*, 76(6):655 – 667, 2004.

[15] M. Kennedy, S.J. McCormack, J. Doran, and B. Norton. Improving the optical efficiency and concentration of a single-plate quantum dot solar concentrator using near infra-red emitting quantum dots. *Solar Energy*, 83(7):978 – 981, 2009.

[16] B. Norton et al. Enhancing the performance of building integrated photovoltaics. *Solar Energy*, 85(8):1629 – 1664, 2011. Progress in Solar Energy 1.

[17] G. Blasse and B.C. Grabmaier. *Luminescent materials*. Springer-Verlag, 1994.

[18] E. Nakazawa. *Phosphor Handbook*. CRC Press, 2^{nd} edition, 2006. Fundamentals of luminescence.

[19] J.G. Bünzli, S. Comby, A. Chauvin, and C.D.B. Vandevyver. New Opportunities for Lanthanide Luminescence. *Journal of Rare Earths*, 25(3):257 – 274, 2007.

[20] N.W. Ashcroft and N.D. Mermin. *Solid State Physics*. Saunders, 1976.

[21] J.R. Hook and H.E. Hall. *Solid State Physics*. Wiley, 2nd edition, 1991.

[22] B.C. Rowan, L.R. Wilson, and B.S. Richards. Advanced Material Concepts for Luminescent Solar Concentrators. *Selected Topics in Quantum Electronics, IEEE Journal of*, 14(5):1312 –1322, sept.-oct. 2008.

[23] B.S. Richards and K.R. McIntosh. Ray-tracing simulations of luminescent solar concentrators containing multiple luminescent species. Dresden, Germany, 2006. 21^{th} European Photovoltaic Solar Energy Conference.

[24] W.G. Quirino, M.J.V. Bell, S.L. Oliveira, and L.A.O. Nunes. Effects of non-radiative processes on the infrared luminescence of Yb^{3+} doped glasses. *Journal of Non-Crystalline Solids*, 351(24-26):2042 – 2046, 2005.

[25] O.M. ten Kate, H.T. Hintzen, P. Dorenbos, and E. van der Kolk. Yb^{3+} doped $LaSi_3N_5$ and YSi_3N_5 with low energy charge transfer for near-infrared light-emitting diode and solar cell application. *Journal of materials chemistry*, 21(45):18289–18294, 2011.

[26] J.W.E. Wiegman. Down-conversion with $NaLaF_4$:1%RE^{3+},5%Yb^{3+} for efficiency improvement of the silicon solar cell. TU Delft, Bachelor's Thesis, May 2010.

[27] C. Görller-Walrand and K. Binnemans. Chapter 167 Spectral intensities of f-f transitions. volume 25 of *Handbook on the Physics and Chemistry of Rare Earths*, pages 101 – 264. Elsevier, 1998.

[28] B.A. Swartz, T. Cole, and A.H. Zewail. Photon trapping and energy transfer in multiple-dye plastic matrices: an efficient solar-energy concentrator. *Opt. Lett.*, 1(2):73–75, Aug 1977.

[29] E. Hecht. *Optics*. Addison Wesley Longman Inc., 4^{th} edition, 2002.

[30] N.J. Cronin. *Microwave and optical waveguides*. Institute of Physics Pub., 1995.

[31] R.R.A. Syms and J.R. Cozens. *Optical guided waves and devices*. McGraw-Hill, 1992.

[32] R. Reisfeld. Fluorescent Dyes in Sol-Gel Glasses. *Journal of Fluorescence*, 12:317–325, 2002. 10.1023/A:1021397422976.

[33] L.R. Wilson and B.S. Richards. Measurement method for photoluminescent quantum yields of fluorescent organic dyes in polymethyl methacrylate for luminescent solar concentrators. *Appl. Opt.*, 48(2):212–220, Jan 2009.

[34] J. Sansregret, J.M. Drake, W.R.L. Thomas, and M.L. Lesiecki. Light transport in planar luminescent solar concentrators: the role of dcm self-absorption. *Appl. Opt.*, 22(4):573–577, Feb 1983.

[35] T.A. Strasser and M.C. Gupta. Optical loss measurement of low-loss thin-film waveguides by photographic analysis. *Appl. Opt.*, 31(12):2041–2046, Apr 1992.

[36] P.K. Tien and R. Ulrich. Theory of prism-film coupler and thin-film light guides. *J. Opt. Soc. Am.*, 60(10):1325–1337, Oct 1970.

[37] M.D. Himel and U.J. Gibson. Measurement of planar waveguide losses using a coherent fiber bundle. *Appl. Opt.*, 25(23):4413–4416, Dec 1986.

[38] November 2011. National Renewable Energy Laboratory – Renewable Resource Data Center, `http://rredc.nrel.gov/solar/spectra/am1.5/`.

[39] E. Matioli et al. High internal and external quantum efficiency InGaN/GaN solar cells. *Applied physics letters*, 98(2), JAN 10 2011.

[40] S. Nishiwaki et al. Surface treatments and properties of CuGaSe2 thin films for solar cell applications. *Thin solid films*, 431:296–300, MAY 1 2003. Spring Meeting of the European-Materials-Research-Society (E-MRS), Strasbourg, France, June 18-21, 2002.

[41] B. Thaidigsmann, A. Wolf, and D. Biro. Accurate Determination of the IQE of Screen Printed Silicon Solar Cells by Accounting for the Finite Reflectance of Metal Contacts. *24th European Photovoltaic Solar Energy Conference, 21-25 September 2009, Hamburg, Germany*, 2009.

[42] J.A.M. AbuShama et al. Properties of ZnO/CdS/CuInSe2 solar cells with improved performance. *Progress in photovoltaics*, 12(1):39–45, JAN 2004.

[43] Bruker Optics. *Manual of VERTEX 80v FT-IR Spectrometer*. compact disk.

[44] P.R. Griffiths and J.A.D. Haseth. *Fourier transform infrared spectrometry*. Chemical analysis. Wiley-Interscience, 2007.

[45] November 2011. Department of Chemistry – Virginia Tech, `http://www.files.chem.vt.edu/chem-ed/optics/selector/spectrom.html`.

[46] G. Wünsch, A. Wennemer, and J.W. McLaren. On the design and performance of the Czerny-Turner monochromator in ICP-AES. *Spectrochimica Acta Part B Atomic Spectroscopy*, 46(11):1517 – 1531, 1991.

[47] A.J.J. Bos et al. Thermoluminescence excitation spectroscopy: A versatile technique to study persistent luminescence phosphors. *Journal of Luminescence*, 131(7):1465 – 1471, 2011.

[48] L.M. Bollinger and G.E. Thomas. Measurement of the Time Dependence of Scintillation Intensity by a Delayed-Coincidence Method. *Review of Scientific Instruments*, 32(9):1044–1050, 1961.

[49] W.W. Moses. A method to increase optical timing spectra measurement rates using a multi-hit TDC. *Nuclear Instruments and Methods in Physics Research Section A: Accelerators, Spectrometers, Detectors and Associated Equipment*, 336(1-2):253 – 261, 1993.

[50] J.E. Goell and R.D. Standley. Sputtered glass waveguide for integrated optical circuits. *Bell Syst. Tech. J.* , 48:3445–3448, 1969.

[51] P.K. Tien. Light waves in thin films and integrated optics. *Appl. Opt.*, 10(11):2395–2413, Nov 1971.

[52] November 2011. Metricon Corporation, `http://www.metricon.com/specs3.html`.

[53] M. Pravettoni et al. Classical behaviour of output light emitted by the edge of a luminescent solar concentrator. In *Photovoltaic Specialists Conference, 2008. PVSC '08. 33rd IEEE*, pages 1 –5, may 2008.

[54] A. Kaminskii et al. Mechanical and optical properties of lu2o3 host-ceramics for ln3+ lasants. *Laser Physics Letters*, 5:300–303, 2008.

[55] Z. Wang et al. Preparation and spectroscopic characterization of lu2o3:eu3+ nanopowders and ceramics. *Optical Materials*, 30(10):1484 – 1488, 2008.

[56] Z. Wang, W. Zhang, B. You, and M. Yin. Effects of precipitant on microstructure and luminescent properties of lu2o3:eu3+ nanopowders and ceramics. *Spectrochimica Acta Part A: Molecular and Biomolecular Spectroscopy*, 70(4):835 – 839, 2008.

[57] E. Zych, D. Hreniak, and W. Strek. Spectroscopic Properties of Lu_2O_3:Eu^{3+} Nanocrystalline Powders and Sintered Ceramics. *The Journal of Physical Chemistry B*, 106(15):3805–3812, 2002.

[58] A. Vasicek. *Optics of Thin Films*. North-Holland, Amsterdam, 1960.

[59] O. Medenbach et al. Refractive index and optical dispersion of rare earth oxides using a small-prism technique. *Journal of Optics A-pure and Applied Optics*, 3(3):174–177, MAY 2001.

[60] E.W. Barrera et al. Emission properties of hydrothermal yb^{3+}, er^{3+} and yb^{3+}, tm^{3+}-codoped lu_2o_3 nanorods: upconversion, cathodoluminescence and assessment of waveguide behavior. *Nanotechnology*, 22(7):075205, 2011.

Appendix A

Manuscript Solar energy

A big part of this work is used for a paper that is about to be submitted to 'Solar energy'. This is the official journal of the International Solar Energy Society, and is devoted exclusively to the science and technology of solar energy applications. The submitted version of this paper is included here.

Building integrated thin film luminescent solar concentrators: detailed efficiency characterisation and light transport modelling.

J.W.E. Wiegman & E. van der Kolk

Delft University of Technology, Luminescent Material Research Group, Mekelweg 15, 2629JB, Delft, the Netherlands

Abstract

An inorganic thin film luminescent solar concentrator (LSC) is characterized experimentally in detail in terms of all the separate light transport steps, which result in the concentration of sunlight. The results are discussed in the context of application as windows in buildings, called building integrated (BI) LSCs. A 3 μm thin film of Eu3+ doped Lu2O3 was chosen because of its large Stokes shift, which excludes all waveguide losses due to self-absorption and allowed to study losses caused by scattering at interfaces of the LSC. A model is presented that can be used to calculate the LSC light transport efficiency as a function of window size, which only needs the easily measured linear attenuation as input. Measurements show that the quantum efficiency (η_{QE}) of our LSC is 13%, which is less than ideal, mainly due to a 44% luminescence quantum efficiency and a 45% waveguide efficiency. Our modelling reveals that, in order to have building integrated LSCs, which can be used as a window simultaneously, the linear attenuation in the LSC should be higher than 1000 mm. This is in contrast to the values in the order of tens of millimetres, which has been measured for the LSC in this paper.

1. Introduction

One of the big aims in photovoltaic (PV) research is to make photovoltaic energy competitive in prize with conventional energy resources. Beside from making the PV-cells more efficient, there is a second option, namely concentration of the sunlight onto the PV-cells.

Luminescent solar concentrators (LSCs), dating back from the 1970s [1, 2], are a very attractive concept for a concentrating PV-module for numerous reasons: production can at low costs, the LSC can operate in diffuse light, therefore not needing expensive solar tracking devises, and, due to the luminescence, only 'cold' light will be collected by the PV-cells, resulting in higher PV efficiencies. In recent years there has been a renewed interest in LSCs due to the urgency of development of sustainable technology combined with new ideas on light trapping and new photo stable luminescent (nano) materials and dye molecules with broader absorption and less self-absorption. [3-6]

In general LSCs consist of a slab of dielectric material containing a luminescent material (organic dyes, quantum dots, or rare-earth complexes), with PV-cells connected to the perimeter of the slab. The luminescence centres absorb the sunlight incident on the face of the LSC, and isotropically emit light at a slightly lower energy. The major part of the emitted light is trapped inside the slab, and is guided to the solar cells at the perimeter. Two different types of LSCs can be identified. The first is the single plate concentrator, in which the luminescence centres are homogeneously spread throughout the plate. The second type, which is considered in this paper, is the thin film LSC. Such LSC consist of an optically passive glass- or polymer-based substrate coated with one or more luminescent layers.

Though the concept of LSCs is very promising, problems like photo-degradation [7-9], limited spectral sensitivity [10], or self-absorption losses [11], have so far prevented large scale use of LSCs.

All problems have been addressed individually, like Wu et al. [12], who reported rare earth complexes showing absorption in de VIS-spectrum and IR emission with zero self-absorption loss. Earp et al. [13] reported in 2004 an LSC with a light transport half-length of 1.2 m (corresponding to a waveguide attenuation length of about 1.7 m). Kennedy et al. [14] presented an LSC based on quantum dots, overcoming the problem of photo stability at the cost of lower luminescent quantum yield. Such limitations of the total LSC PV-module cause the application of LSCs to still remain a castle in the air.

An interesting application would be building integrated (BI) LSCs [15], in which the windows of e.g. office buildings are coated with an UV absorbing luminescent thin film, and can therefore act as (additional) power supplies for such buildings. As office buildings often have shaded glass, partial absorption in the visible part of the solar spectrum would be acceptable as well, yielding better usage of the available sunlight and increasing feasibility of the BI LSC.

The performance of an LSC is directly linked to its optical efficiency (η_{opt}), as defined in equation 1.1 [16].

$$\begin{aligned}\eta_{opt} &= \eta_{LHE}\eta_{LQE}\eta_{Stokes}\eta_{trap}\eta_{SA}\eta_{WG}\left(1-R\right) \\ &= \eta_{QE}\eta_{Stokes}\end{aligned} \qquad 1.1$$

The optical efficiency is given by the product of the light harvesting efficiency (η_{LHE}) [11], the luminescent quantum efficiency (η_{LQE}) [17], the Stokes' efficiency (η_{Stokes}), the light trapping efficiency (η_{trap}) [18], the self-absorption (η_{SA}) [19], the waveguide efficiency (η_{WG}) [13], and (1-*R*), in which *R* represents the Fresnel reflection coefficient of the LSC surface. In short it is given by the product of the quantum efficiency of the LSC (η_{QE}) and the Stokes' efficiency.

The light harvesting efficiency can be calculated for a given source spectrum and absorption spectrum [11]. In this research however, the source spectrum consists of only one wavelength, resulting in a light harvesting efficiency equalling the absorption at that wavelength.

Optical efficiencies of up to 12% have been reported for dye-polymer-based thin film LSCs by Dienel et al. [11]. A similar optical efficiency of up to 13.2% is predicted by Kennedy et al. [14] using a QD doped single plate concentrator. In both papers though, the waveguide efficiency η_{WG} is assumed to be unity, which, as is shown by Earp et al. [13], can deviate from unity significantly.

In the first part of this paper we will investigate the efficiencies of the various processes that are involved in the concentration of sunlight in the $Lu_2O_3:Eu^{3+}$ thin film luminescent solar concentrator. We quantify the specular reflection, the absorption efficiency, the luminescent quantum efficiency, the Stokes' efficiency, the calculated light trapping efficiency and the calculated waveguide efficiency, based on the linear attenuation length.
In the second part we will present a light transport model that considers the linear attenuation and the dimension of the waveguide. This model allows us to calculate the fraction of the trapped luminescence light, that reaches the perimeter of the LSC, under homogeneous illumination of the LSC. This allows for the calculation of the light transport efficiency $\eta_t = \eta_{SA}\,\eta_{WG}$ with an easy to perform measurement. Finally, we discuss the boundary conditions for light transport efficiency and window size for realizing a worthwhile building integrated thin film LSC.

2. Experimental procedures

The used LSC sample has been made by Boston Applied Technologies, Inc. The substrate of 250 µm Al3O2 (c-cut Sapphire) have been submerged into a solution of $Lu_2O_3:8\%Eu^{3+}$, depositing a film of 3 µm on the substrate.

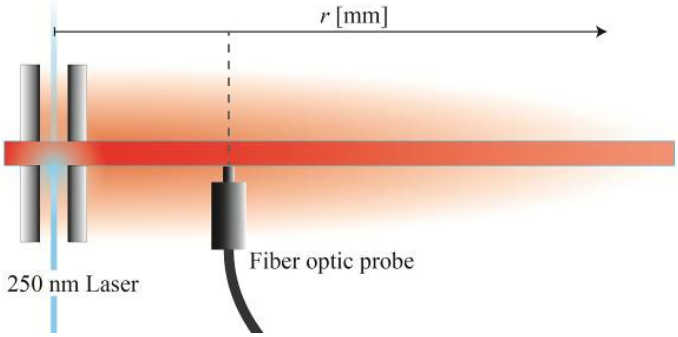

Figure 1. Schematic drawing of the experimental setup of the linear attenuation measurement.

The transmission measurements have been performed using an AvaLight-DHc light source, emitting in the UV-NIR spectral region, and an AvaSpec-3648 Czerny-Turner spectrometer.
The photo-luminescent excitation spectrum is taken using a 450 Watt Xenon-lamp, two monochromators, and photon counting detection techniques. A full setup description is given by Bos et al. [20].
The emission spectrum was measured with an Ocean Optics QE65000 Czerny-Turner spectrometer, after laser excitation at 250 nm in the CT-band of Eu^{3+}.
The time-resolved luminescence decay spectrum was measured using time correlated single photon counting (TCSPC), with a 50Hz pulsed Xenon lamp and a LeCroy 4208 multi-hit time-to-digital converter (TDC). A Jobin Yvon H10 monochromator was used to selects the orange-red 5D0 emission of Eu3+ and a channel photomultiplier was used as the photon detector.
The linear attenuation length, μ, quantifying the light transport efficiency, η_t, from the point of laser excitation to the point of detection, is measured with the setup shown in Figure 1.
The LSC was fixed between two hollow clamps, through which a 250 nm laser excites the LSC. The clamps prevent stray light induced at the laser spot from reaching the optical fibre probe. The probe is positioned very close to one face of the LSC, where it measures the intensity of scattered luminescence light escaping from the LSC under normal incidence. The intensity is monitored along r in Figure 1 and is assumed to be proportional to the amount of light lost from the LSC at that point, which in turn is proportional to the amount of light present in the LSC at that position [21, 22]. The edges have been painted black using Revell #8 matt black dye, to avoid measuring effects caused by internal reflections on the edge surfaces. This dye absorbs about 96% of the red light incident on the LSC-dye interface.

3. Results

In Figure 2 the transmission spectrum of our LSC is plotted in the UV-NIR spectral region. The spectrum immediately shows that our LSC is not intended to work as an efficient solar concentrating device as it is not capable of absorbing any sunlight. At wavelengths shorter than about 350 nm strong absorption is observed that reaches a maximum at about 215 nm.
A reflection of 10% at 250 nm is measured, which is caused by the relatively high index of refraction of Lu_2O_3 of 1.93. At this wavelength we measure a transmission of 12%, resulting, in combination with the reflection, in an absorption of 87% of the non-reflected light.
It can be concluded that LSCs based on luminescent materials with a charge transfer transition are very well capable of absorbing sufficient sunlight in two 3 µm thick layers, provided that the CT-band is shifted to the blue at lower energy, which has been shown for example by Ten Kate et al. [23].

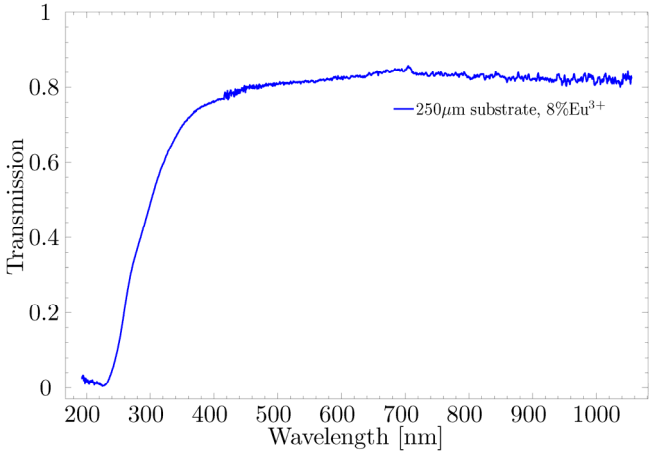

Figure 2. Transmission spectra of a 3 µm $Lu_2O_3:8\%Eu^{3+}$ thin film on a 250 µm Al_2O_3 substrate.

Figure 3 shows the luminescence excitation spectrum of the film monitoring the $^5D_0 \rightarrow {}^7F_2$ transition of Eu^{3+} at 611 nm. The spectrum is plotted on a log y scale, so that the weak parity forbidden 4f-4f transitions and the strong CT transition of Eu^{3+} can be observed simultaneously. The excitation spectrum reaches a maximum just below 250 nm. Both the laser and the Xenon lamp operate well at 250 nm, which motivates our choice to further characterize the LSC at 250 nm in the rest this paper.
Figure 4 shows the emission spectrum that is observed when the LSC is excited at this wavelength. The typical orange-red emission is observed from Eu^{3+}, when it is incorporated in the structure as a non-centrosymmetric crystallographic site. The strongest emission is at 611 nm, which is the $^5D_0 \rightarrow {}^7F_2$ emission peak of Eu^{3+} [24]. One should note the large Stokes' shift, which prevents any self-absorption.
The absence of self-absorption gives the opportunity to study losses due to scattering in the waveguide, a property often

neglected in former research, as already mentioned in the introduction.

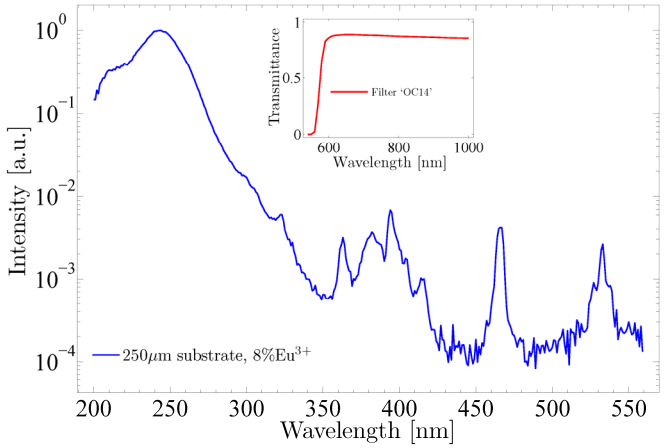

Figure 3. Excitation spectra of the 3 µm Lu_2O_3:8%Eu^{3+} thin films monitoring the 611 nm Eu^{3+} emission.

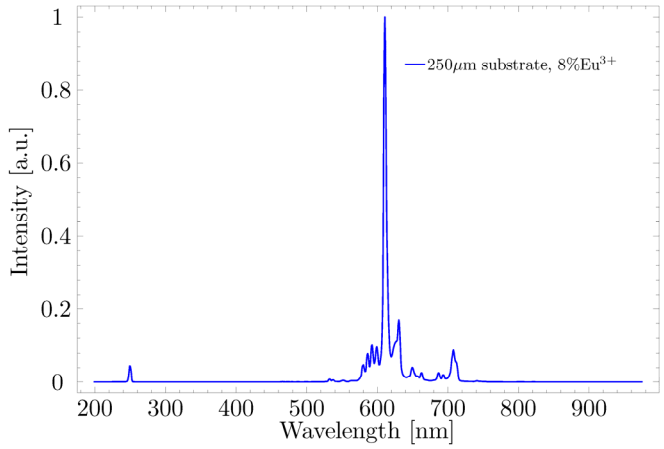

Figure 4. Emission spectrum of the Lu_2O_3:Eu^{3+} thin film, under 250 nm excitation.

Now we know the amount of reflection and absorption, it is important to know which fraction of the absorbed light is converted to luminescence.

The luminescent quantum efficiency η_{LQE} was estimated from the measured time-resolved spectrum shown in Figure 5. It shows a strongly non-exponential decay behaviour, which can be explained by concentration quenching. It is well known that, at concentrations as high as 8%, concentration quenching can already has a noticeable effect [25, 26]. Literature data on the decay time of Eu in Lu_2O_3 at very low Eu concentrations, at which concentration quenching can be excluded, reveal a decay time that is never higher than 1 ms [26].

If we compare our decay spectrum with an exponential decay of 1 ms by integrating the areas under the two spectra we conclude that the quantum efficiencies of our luminescent material is approximately 43.8% for the 8%Eu^{3+} doped film.

The next thing to know is how much of the emitted luminescence is actually trapped in the LSC. Figure 6 schematically depicts a cross-section of a thin film LSC with the luminescent thin films on both sides of the substrate. The red, yellow and green parts represent the three different possibilities for the light to travel.

Luminescence, emitted in the red part, directly escapes from the LSC through the so-called escape cone. It can easily be shown that an equal amount of light escapes from the LSC at the front and at the rear faces of the LSC. Light emitted in the green part is trapped in the thin film by total internal reflection at the film-air and film-substrate interfaces. Finally, light emitted in the yellow part is trapped in both the thin film and the substrate, by total internal reflection at the film-air interfaces. Formula 3.1 [11, 27], 3.2 [4] and 3.3 give the magnitudes of the light that is contained in the red, green and yellow parts respectively.

$$F_{lost} = 1 - \sqrt{\frac{n_{film}^2 - n_{air}^2}{n_{film}^2}} \qquad 3.1$$

$$F_{film} = \sqrt{\frac{n_{film}^2 - n_{sub}^2}{n_{film}^2}} \qquad 3.2$$

$$F_{film+sub} = \frac{1}{n_{film}} \left\{ \sqrt{n_{film}^2 - n_{air}^2} - \sqrt{n_{film}^2 - n_{sub}^2} \right\} \qquad 3.3$$

The formulas, which were derived from standard laws of optics describing reflection and refraction, show that the trapped light fractions only depend on the index of refraction of the film and the substrate. By filling in an index of refraction of 1.76 for our substrate and 1.93 for our film we find that 14% of light is lost through the escape cone, 41% of the luminescence is trapped in the thin film, and 45% of the light is trapped in the film-substrate-complex. We can conclude that from all luminescence light 86 % is initially trapped in the LSC.

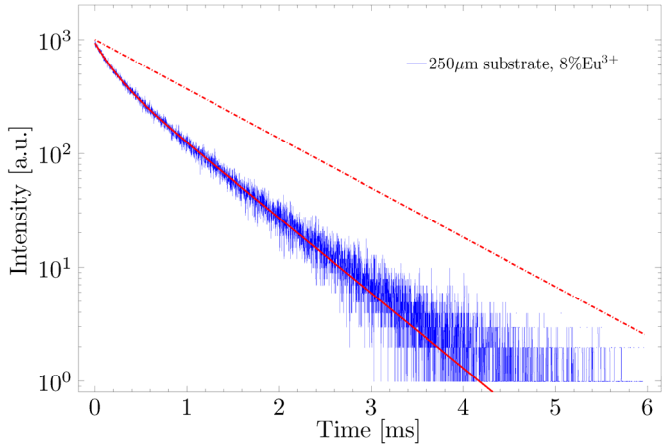

Figure 5. Time resolved spectrum of Lu_2O_3:Eu^{3+}, under 250 nm excitation.

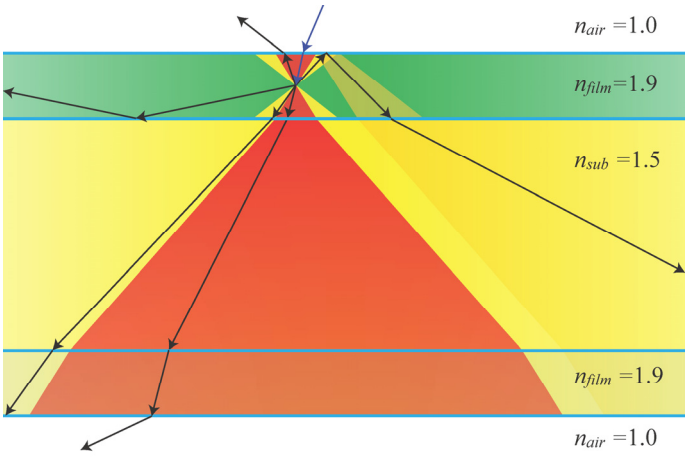

Figure 6. Schematic representation of a cross-section of a thin film LSC, with the escape cone (red), the light trapped only in the film

(green), and the light trapped in both the film and the waveguide (yellow).

In order to estimate the amount of trapped light that reaches the perimeter of the LSC the attenuation length is determined. In order to measure this, the LSC is illuminated with a focussed laser beam of 250 nm at a specific spot on the LSC. The amount of Eu emission that escapes from the LSC under normal incidence is measured as a function of distance away from the laser spot with the setup shown in Figure 1. Luminescence escaping is spectrally resolved by a fibre optic probe connected to a USB spectrometer, so that we are sure no other light is contributing to the intensity. As mentioned before, the intensity measured is proportional to the amount of light escaping from the LSC, which is in turn proportional to the amount of light present in the LSC.

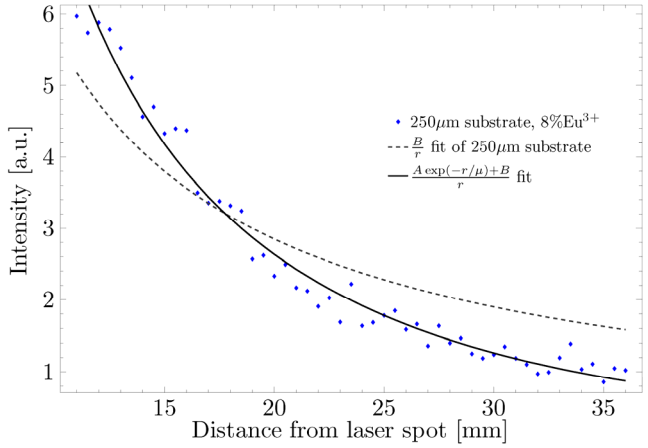

Figure 7. Attenuation as a function of distance from the laser spot due to cylindrical intensity spreading and waveguiding deficiency.

Figure 7 shows the recorded intensity (the blue dots show the 250 µm LSCs measurement) as function of distance r away from the laser spot. As light originates from a point and spreads out over a plane, we expect for an ideal slab waveguide a $1/r$ dependence, which is plotted as the dashed curve in Figure 7. It is clear that the experimentally recorded intensity drops faster than is expected based on the $1/r$ dependence, which is caused by loss of light in the LSC due to scattering. The loss can be modelled very well by an exponential loss factor [21, 22, 28] that contains the linear attenuation length μ, see equation 3.4.

$$I = \frac{A\exp\left(-r/\mu\right)+B}{r} \qquad 3.4$$

From the fits through the data a μ-value of 25 mm is obtained for our LSC. This value gives the typical length over which the intensity decreases. It therefore should be compared to the size of the LSC to be able to find the light transport efficiency of a specific sized LSC.

In the next part we connect the experimental parameter μ with the light transport efficiency, η_t, which represents the fraction of the trapped luminescence that reaches the LSCs perimeter in case of homogenous illumination of the entire LSC surface. In general $\eta_t = \eta_{SA}\,\eta_{WG}$. In our specific case however the self-absorption efficiency is unity, and therefore the light transport efficiency equals the waveguide efficiency.

4. Light transport modelling of thin film BI LSCs

Formula 4.1 gives $\eta_{t,rectangular}$ for a rectangular LSC with dimensions $H \times W$ (a formula for a circular LSC with diameter D is given by formula A.1 in APPENDIX A).

$$\eta_{t,rectangular} = \frac{1}{\pi HW}\int_0^H\int_0^W \int_{\arctan\left[\frac{H-y}{W-x}\right]}^{\arctan\left[\frac{x}{H-y}\right]+\frac{\pi}{2}} \exp\left\{-\frac{H-y}{\mu\sin\theta}\right\} d\theta\,dx\,dy + \frac{1}{\pi HW}\int_0^W\int_0^H \int_{\arctan\left[\frac{W-x}{H-y}\right]}^{\arctan\left[\frac{y}{W-x}\right]+\frac{\pi}{2}} \exp\left\{-\frac{W-x}{\mu\sin\theta}\right\} d\theta\,dy\,dx \qquad 4.1$$

The triple integral contains basically two parts. The first part, the integral over theta, sums over the radiation reaching one edge of the LSC emitted by an infinitesimal area, dydx, of the LSC. The $1/\pi$ in front is due to the cylindrical emission of dydx. The exponent, over which is integrated, simply is the exponential decay over the distance from the area dydx to the edge. The boundaries are offspring to the rectangular shape of the LSC.

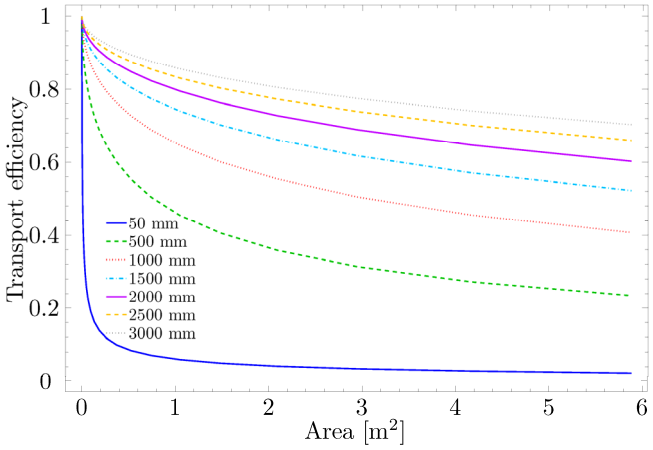

Figure 8. Light transport efficiency, ηt = ηSA ηWG, as a function of size of square LSCs for various linear attenuation length.

The second and third integral sum over the contributions of all area dydx, summing up to the total area H x W. Division by the total area gives us the final light transport efficiency η_t.

The integral can be evaluated numerically as a function of the parameters μ, W and H. The results of such calculations are shown in Figure 8 and Figure 9 for the special case of $W = H$.

Figure 8 shows the light transport efficiency η_t, or in the case of zero self-absorption the waveguide efficiency η_{WG}, as a function of the size of the LSC (or the size of the window) for various linear attenuation lengths μ. Figure 9 shows the light transport efficiency as a function of the linear attenuation length for various window sizes. Figure 8 correctly shows that for small waveguide dimension, the efficiency η_t approaches 100%. This is expected, as for small waveguides, light does not have to travel far to reach the perimeters of the LSC. The figure shows that for a typical window size of 2 m^2, a linear attenuation μ of more than 1000 mm is needed in order to have a waveguide light transport efficiency of more than 50%. This is in large contrast to the μ-value of 24 mm that was measured for our LSC. We will come back to this in the discussion section. Interestingly, Figure 8 shows that the efficiencies become more and more constant towards larger window sizes. We conclude that for larger window sizes only a certain edge

region, close to the perimeter, contributes to the total of emitted light that reaches the perimeters. The LSC regions to the centre of the waveguide do contribute much less, as most luminescence emitted there does not reach the perimeter anymore.

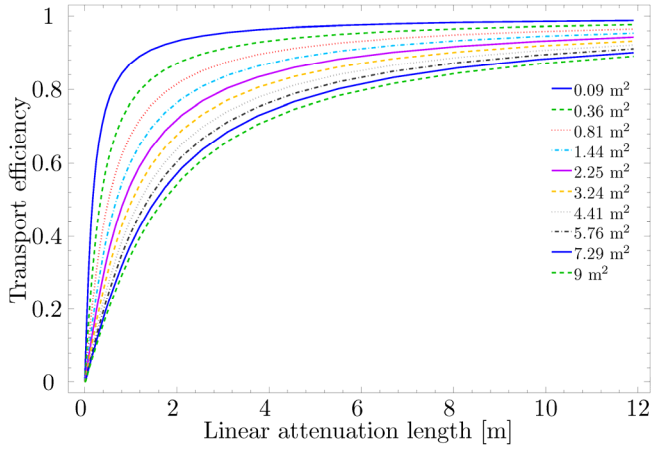

Figure 9. Light transport efficiency as a function of linear attenuation length for different sizes of square LSCs.

The data plotted in Figure 8 and Figure 9 can be merged into one graph shown in Figure 10. The dimensionless attenuation length La is defined for a square LSC by equation 4.2, in which $W \leq H$.

$$\mathrm{La} \equiv \mu / W \qquad 4.2$$

This way of presenting the data allows for showing the efficiencies not only for different LSC sizes, but also for different proportions of the LSCs.
In this way we simultaneously see that for $W >> \mu$ the light transport efficiency goes to zero, and for $W << \mu$ the light transport efficiency goes to unity.
We can conclude from our calculations that the dimensionless attenuation length La is an important parameter for an LSC, as this parameter represents the proportion between the LSC dimensions and the typical length over which the light escapes the LSC by parasitic processes. This ratio in turn determines the light transport efficiency η_t, representing the combination of the Stokes' efficiency and the waveguide efficiency.
The data in Figure 10 can be fitted with the empirical formula for the light transport efficiency given by equation 4.3.

$$\eta_t \approx \frac{\mathrm{La}^n}{K + \mathrm{La}^n} \qquad 4.3$$

In equation 4.3, K and n are valued respectively 0.547 and 1.117 for a square LSC. The inset in Figure 10 shows the residual error of the fit. As can be seen the error is maximally 0.6 percentage point, which is generally less than the uncertainty induced by the measurement of the linear attenuation length.
In Figure 10 it can be observed that for small linear attenuation lengths μ, compared to the dimensions of the LSC, the light transport efficiency goes down rapidly. However, because the efficiency is a function of the proportion between the size of the LSC and the linear attenuation length, the efficiency can still be fairly high for small values of μ. Our 250 µm sample for instance has an La-value of 0.48, if we however scale up our LSC to a size of one meter, its La-value would drop to 0.024, decreasing its transport efficiency η_t from 45% to only 2.8%.

Table 1. The various measured efficiencies of the $Lu_2O_3:Eu^{3+}$ thin film LSC.

	3 µm Lu_2O_3:8%Eu^{3+} on 250 µm Al_2O_3
1-R	90%
η_{LHE}	87%
η_{LQE}	43.8%
η_{SA}	100%
η_{Stokes}	41%
η_{trap}	86%
η_{WG}	45%
η_{QE}	13%

It is instructive to summarize the efficiencies of the various steps involved in the concentration of sunlight. In Table 1 it is shown that the loss due to reflection is 10%, the light harvesting efficiency is 87%, the luminescence quantum efficiency is 43.8%, the trapping efficiency is 86%, and the light transport efficiency 45%. One should note that the measured linear attenuation length μ and the calculated light transport efficiency were non-specific in the sense that it is a measurement of light transport in both the film and the film-substrate-complex.
When these efficiencies are multiplied a quantum efficiency, η_{QE}, of 13% follows at 250 nm excitation. The optical efficiency can be calculated by multiplying η_{QE} by the Stokes' efficiency of 0.4, since the 250 nm light is converted to 611 nm light of the Eu^{3+} ions. This energy efficiency value is not very useful, as our LSC was not intended to be a real solar concentrating device, but rather an LSC in which fundamental light transport can be studied without the well-known and studied self-absorption.[19]

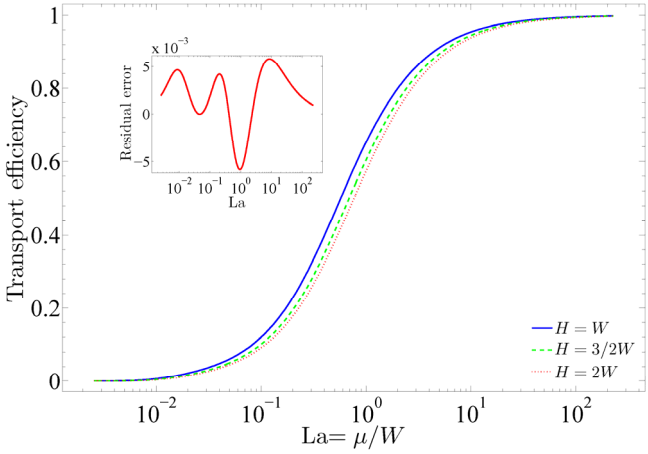

Figure 10. Calculated light transport efficiencies are plotted as a function of the dimensionless attenuation length La. The efficiencies are plotted for different proportions of the windows (blue, green and red), in which always $W \leq H$. The residual error of the empirical fit of equation 4.3 is shown in the inset.

5. Discussion

From Table 1 it becomes clear that the optical efficiency of the presented LSC is not 100%, mostly due to a low luminescent quantum efficiency of the luminescent material (43.8%) and the low light transport efficiency (45%). As the light transport in our thin film LSC is only controlled by the linear attenuation length that is not affected by self-absorption, the waveguide loss must be due to scattering at the various interfaces.
One way to improve the waveguide efficiency is to better match the refractive indices of the film and the substrate. In our LSC are, as follows from formulas 3.2 and 3.3, 41% and 45% trapped in respectively the film and the film-substrate-complex.

Matching the refractive indices will result in a larger fraction of light trapped inside the film-substrate-complex instead of in the film. Lowering the refractive index of the film however would result in a larger escape cone, as follows from formula 3.1, and should therefore be treated carefully.
A second way is to use a thicker substrate with a more realistic thickness for a window of 3 mm. Light trapped in the film-substrate-complex, in that case, has less interaction moments with the interfaces, while it zigzags along the LSC.
In order to have the highest possible trapping efficiency high index of refraction film is desired, as follows from formula 3.1. In that case it is important to investigate which physical parameters controls the waveguide efficiency, like surface roughness or perhaps low efficiency is caused by light confinement issues that are not considered in this work, e.g. limited waveguide modes.
For building integrated applications, where LSC sizes are typically large (>1 m^2), the linear attenuation should be in the order of 1000 mm in order not to lose too much energy, and have a light transport efficiency of about 50%.
As mentioned earlier for large LSCs only a certain edge region contributes to the total concentrated light at the perimeter. For large window sizes it is therefore a useful idea to only coat this edge region with a luminescent layer and leave the central region clear. This might not only save cost, but also opens up the possibility to apply luminescent coatings that absorb not only the UV spectral region, but also (part of) the visible region, hereby generating much more electricity. The near-edge regions of the window will then be coloured or even black, where the central region is clear serving as a window for daylight to enter the building.
Finally we present in Figure 11 the calculated power efficiencies of an LSC device as a function of absorption edge of the luminescent material. This is done for different LSC sizes and attenuation lengths.
The reflection at the surface of the LSC is chosen to be according the Fresnel equations, with an index of refraction of the film of 1.93.
For incident light of energies exceeding the absorption edge, the absorption by the luminescent material is taken 0.8 and zero for lower energies.
Furthermore the self-absorption is assumed to be zero. Therefore, the emission is shifted 10 nm outside the absorption region of the luminescent material.
This refractive index of the film determines the trapping efficiency, which is calculated with equations 3.2 and 3.3. Furthermore, a luminescent quantum efficiency is chosen of 0.8. And finally the source has been assumed to be a solar AM1.5 spectrum [29].
The internal quantum efficiency (IQE) curves of InGaN/GaN [30], CGS [31], Si [32], and CIS [33] have been used to calculate the power efficiency of the cells at the emission wavelength of the luminescent material.
From the calculations follow that for fully transparent glass (absorption up to 400 nm) a power efficiency of the order of only 2% is achievable, corresponding to 20 Wpm^{-2}. If, however, one would accept coloured glass, power efficiencies can go up significantly, for yellow or red glass to 5% and 10% respectively. One should note that for achieving such efficiencies when sunlight is collected at an area of the order of 1 m^2 an area of the order of only 0.01 m^2 of solar cell is needed. As the luminescent material was freely chosen, and is probably not available as such, Figure 11 only gives an indication of what efficiencies are possible to achieve.

6. Conclusion

We have identified the different loss processes in luminescent solar concentrating. The accompanying efficiencies have been determined for a thin film LSC, based on Eu^{3+} doped Lu_2O_3. The attenuation length has been determined, which is a measure for the losses due to self-absorption and scatter losses.
We have shown how to calculate the light transport efficiency of the LSC based on the easy to perform attenuation measurement.
The light transport efficiency has been fitted with an easy to calculate empirical formula, making calculation of the light transport efficiency for different sizes of LSCs comfortable.
The LSCs studied in this paper have shown to have low optical efficiencies, mainly due to due to a low luminescent quantum efficiency of the luminescent material and the low light transport efficiency.
Finally, achievable power efficiencies have been calculated for a variety of LSC dimensions and attenuation lengths using common photovoltaic cells, showing power efficiencies of up to 17%.

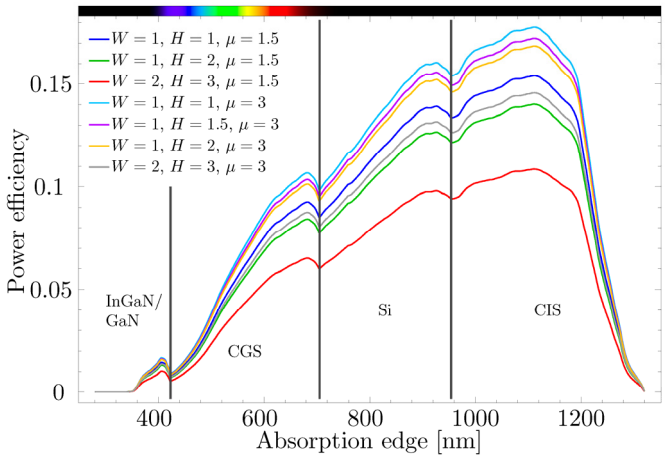

Figure 11. Calculated power efficiencies for LSCs connected to InGaN/GaN, CGS, cSi, and CIS solar cells. The efficiencies are plotted for different sizes and attenuation lengths of the LSC. For incident light of energies exceeding the absorption edge, the absorption by the luminescent material is taken to be 0.8 and zero for lower energies.

A. Light Transport efficiency for circular LSCs

Whereas equation 4.1 gives the light transport efficiency for a rectangular LSC, equation A.1 gives the equation for the light transport efficiency for circular LSCs. The function *d* gives the distance from the infinitesimal area $r dr d\theta$ to the perimeter of the LSC.

$$\eta_{t,\text{circular}} = \frac{2}{(D\pi)^2}\int_0^{2\pi}\int_0^{D/2}\int_0^{2\pi} r \exp\left\{-\frac{d(r,\theta,\xi)}{\mu}\right\} d\xi\, dr\, d\theta \qquad \text{A.1}$$

with

$$d(r,\theta,\xi) = \sqrt{\frac{D^2}{4} + r^2\left\{(\cos\xi\cos\theta + \sin\xi\sin\theta)^2 - 1\right\}} - r(\cos\xi\cos\theta + \sin\xi\sin\theta)$$

B. Light Transport efficiency coefficients

In Table 2 coefficients for calculation of the light transport efficiency using equation 4.3 are given for three different proportions of LSCs.

Table 2. *K* and *n* values for different proportions of LSCs.

W : *H*	K	n
1:1	0.547	1.117
2:3	0.673	1.113
1:2	0.760	1.106

Bibliography

1. Weber, W.H. and J. Lambe, *Luminescent greenhouse collector for solar-radiation.* Applied Optics, 1976. **15**(10): p. 2299-2300.
2. Goetzberger, A. and W. Greube, *Solar energy conversion with fluorescent collectors.* Applied Physics A: Materials Science & Processing, 1977. **14**(2): p. 123-139.
3. van Sark, W.G.J.H.M., et al., *Luminescent Solar Concentrators - A review of recent results.* Optics Express, 2008. **16**(26): p. 21773-21792.
4. King Mapel, J., *Organic photovoltaics and concentrators.* Massachusetts Institute of Technology, Dept. of Electrical Engineering and Computer Science, 2008.
5. Reisfeld, R., *New developments in luminescence for solar energy utilization.* Optical Materials, 2010. **32**(9): p. 850-856.
6. Currie, M.J., et al., *High-efficiency organic solar concentrators for photovoltaics.* Science, 2008. **321**(5886): p. 226-228.
7. Batchelder, J.S., A.H. Zewail, and T. Cole, *Luminescent solar concentrators. 1: Theory of operation and techniques for performance evaluation.* Appl. Opt., 1979. **18**(18): p. 3090-3110.
8. Wittwer, V., W. Stahl, and A. Goetzberger, *Fluorescent planar concentrators.* Solar Energy Materials, 1984. **11**(3): p. 187-197.
9. Kinderman, R., et al., *I-V performance and stability study of dyes for luminescent plate concentrators.* Journal of Solar Energy Engineering-Transactions of the Asme, 2007. **129**(3): p. 277-282.
10. Reisfeld, R., D. Shamrakov, and C. Jorgensen, *Photostable solar concentrators based on fluorescent glass-films.* Solar Energy Materials and Solar Cells, 1994. **33**(4): p. 417-427.
11. Dienel, T., et al., *Spectral-based analysis of thin film luminescent solar concentrators.* Solar Energy, 2010. **84**(8): p. 1366-1369.
12. Wu, W., et al., *Hybrid solar concentrator with zero self-absorption loss.* Solar Energy, 2010. **84**(12): p. 2140-2145.
13. Earp, A.A., et al., *Maximising the light output of a Luminescent Solar Concentrator.* Solar Energy, 2004. **76**(6): p. 655-667.
14. Kennedy, M., et al., *Improving the optical efficiency and concentration of a single-plate quantum dot solar concentrator using near infra-red emitting quantum dots.* Solar Energy, 2009. **83**(7): p. 978-981.
15. Norton, B., et al., *Enhancing the performance of building integrated photovoltaics.* Solar Energy, 2011. **85**(8): p. 1629-1664.
16. Reisfeld, R. and C.K. Jorgensen, *Luminescent solar concentrators for energy-conversion.* Structure and Bonding, 1982. **49**: p. 1-36.
17. Wilson, L.R. and B.S. Richards, *Measurement method for photoluminescent quantum yields of fluorescent organic dyes in polymethyl methacrylate for luminescent solar concentrators.* Applied Optics, 2009. **48**(2): p. 212-220.
18. Grande, M., et al., *The application of thin-film wavelengt-shifting coatings of perspex to solar-energy collection.* Journal of Physics D-Applied Physics, 1983. **16**(12): p. 2525-2535.
19. Sansregret, J., et al., *Ligth transport in planar luminescent solar concentrators - the role of DCM self-absorption.* Applied Optics, 1983. **22**(4): p. 573-577.
20. Bos, A.J.J., et al., *Thermoluminescence excitation spectroscopy: A versatile technique to study persistent luminescence phosphors.* Journal of Luminescence, 2011. **131**(7): p. 1465-1471.
21. Tien, P.K. and R. Ulrich, *Theory of prism-film coupler and thin-film light guides.* Journal of the Optical Society of America, 1970. **60**(10): p. 1325-&.
22. Himel, M.D. and U.J. Gibson, *Measurement of planar wave-guide losses using a coherent fiber bundle.* Applied Optics, 1986. **25**(23): p. 4413-4416.
23. ten Kate, O.M., et al., *Yb(3+) doped LaSi(3)N(5) and YSi(3)N(5) with low energy charge transfer for near-infrared light-emitting diode and solar cell application.* Journal of Materials Chemistry. **21**(45): p. 18289-18294.
24. Blasse, G. and B.C. Grabmaier, *Luminescent materials*. 1994: Springer-Verlag.
25. Zych, E., D. Hreniak, and W. Strek, *Spectroscopic Properties of \LuOEu Nanocrystalline Powders and Sintered Ceramics.* The Journal of Physical Chemistry B, 2002. **106**(15): p. 3805-3812.
26. Wang, Z., et al., *Preparation and spectroscopic characterization of Lu2O3:Eu3+ nanopowders and ceramics.* Optical Materials, 2008. **30**(10): p. 1484-1488.
27. Reisfeld, R., *Fluorescent Dyes in Sol-Gel Glasses.* Journal of Fluorescence, 2002. **12**(3): p. 317-325.
28. Goell, J.E. and R.D. Standley, *Sputtered glass waveguide for integrated optical circuits.* Bell Syst. Tech J., 1969. **48**: p. 3445-3448.
29. 2011 November, Available from: National Renewable Energy Laboratory - Renewable Resource Data Center: http://rredc.nrel.gov/solar/spectra/am1.5/.
30. Matioli, E., et al., *High internal and external quantum efficiency InGaN/GaN solar cells.* Applied physics letters, 2011. **98**(2).
31. Nishiwaki, S., et al., *Surface treatments and properties of CuGaSe2 thin films for solar cell applications.* Thin solid films, 2003. **431**: p. 296-300.
32. Thaidigsmann, B., A. Wolf, and D. Biro, *Accurate determination of the IQE of screen printed silicon solar cells by accounting for the finite reflectance of metal contacts.* 24th European Photovoltaic Solar Energy Conference, 21-25 September 2009, Hamburg, Germany, 2009.
33. AbuShama, J.A.M., et al., *Properties of ZnO/CdS/CuInSe2 solar cells with improved performance.* Progress in photovoltaics, 2004. **12**(1): p. 39-45.

Appendix B

Refraction of escape cone

The angle of the escape cone of the film-air interface is given by equation 2.10.

$$\zeta_{c,film,air} = \arcsin\left(\frac{n_{air}}{n_{film}}\right) \tag{B.1}$$

The 'c' denotes that the angle is the critical angle, 'film,air' denotes that the incoming light ray travels from the film to the air. Using the Snell's law, equation 2.9, the angle of the refracted beam in the substrate A is determined to obey equation B.2.

$$A = \arcsin\left[\frac{n_{film}}{n_{sub}}\sin\alpha\right] \tag{B.2}$$

As α equals $\zeta_{c,film,air}$, equations B.1 and B.2 result in an equation describing the angle of the refracted beam, equation B.3.

$$\begin{aligned} A &= \arcsin\left[\frac{n_{film}}{n_{sub}}\sin\left\{\arcsin\left(\frac{n_{air}}{n_{film}}\right)\right\}\right] \\ &= \arcsin\left[\frac{n_{air}}{n_{sub}}\right] \\ &= \zeta_{c,sub,air} \end{aligned} \tag{B.3}$$

From equation B.3 we see that the refracted critical beam of the film exactly corresponds to the critical angle of the substrate.

Appendix C

FT-IR data

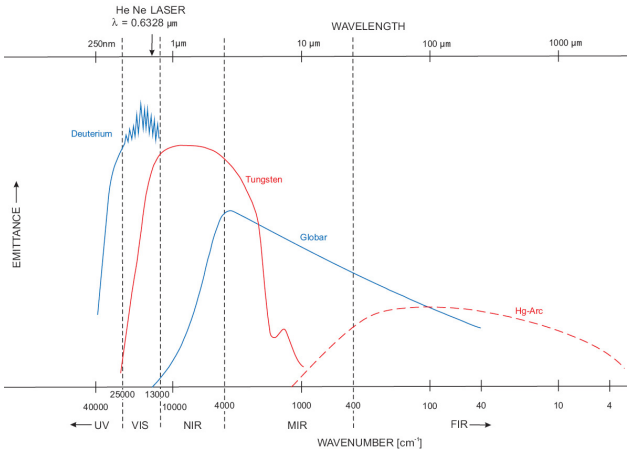

Figure C.1: Emittance of the Bruker sources in FT-IR spectrometry. [43]

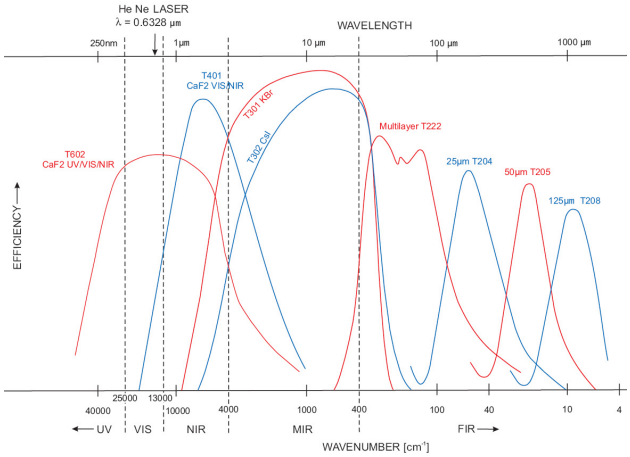

Figure C.2: Efficiency of the Bruker beam splitters in the interferometer. [43]

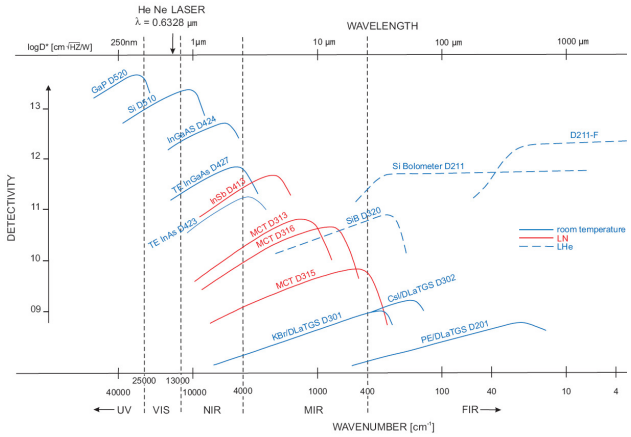

Figure C.3: Detectivity of the Bruker detectors during FT-IR spectrometry. [43]

Appendix D

Energy distribution

Obviously a photon trapped inside the film, if no losses are considered, will eventually reach the side of the LSC without entering the substrate. But it is less self-evident in which layer to find a photon trapped in both layers. So consider such photon from the yellow part of figure 2.9. When the photon is incident on the interface between the film and the substrate, there is a certain chance the photon reflects and one minus that chance that it is transmitted into the substrate. Suppose it is reflected, then it will reflect at the top surface (the face), as it was trapped inside the waveguide system. After this reflection the photon will again hit the interface of the film and substrate. And this process goes on and on. So the chance the photon has never been in the substrate after n reflections is R^n.

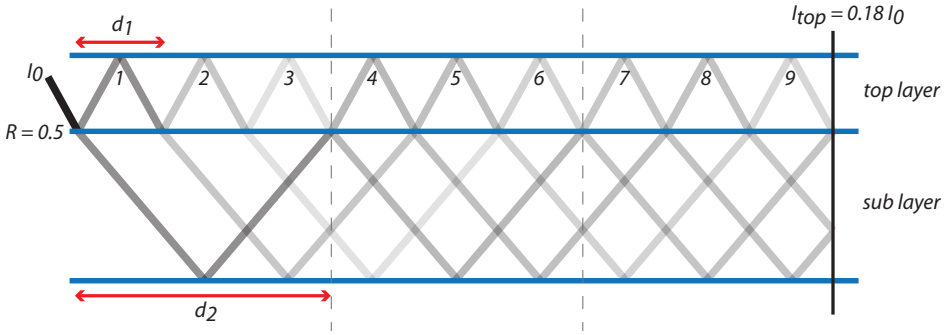

Figure D.1: Energy distribution over the film and the substrate of light emitted by a luminescent center in an LSC. The light is emitted such that it is trapped in the two layers combined. Due to multiple reflections in the film per reflection in the thick substrate, the energy is located more and more in the substrate. In this figure the reflection between the film and the substrate is taken to be 0.5. The gray shades give the intensity of the light beams.

Now suppose we have two emitted photons, with same angles of incidence on the interface, for which the chance is half[1] for being reflected. Assume that one is reflected, and the other is transmitted. Now, due to the fact that the thickness of the luminescent layer is very small compared to that of the substrate, the reflected photon will reach the interface closer than

[1]The chance of one half is arbitrary, but gives insight in the process.

the transmitted photon, see for example figure D.1. So the reflected photon again has chance one half of being transmitted. Repeating this a few times will lead to the highest chance to find both photons in the substrate. For very thin films, this process goes fast, resulting in a negligible part in the thin film, and therefore all in the substrate.

Of course this can all be expressed mathematically. Suppose, for simplicity, that the distance traveled parallel to the LSC in the sub layer per reflection on the sub interface, d_2 in figure D.1, is a whole number times the distance traveled parallel to the LSC in the film per reflection on the top interface, d_1 in figure D.1. That ratio, N, is given by equation D.1.

$$N = \frac{d_2}{d_1} \tag{D.1}$$

With this ratio one can determine an expression for the intensity at point n in the film, which is given by equation D.2.

$$I_n = RI_{n-1} + (1-R)^2 \sum_{i=0}^{\frac{n-1}{N}-1} R^i I_{n-((i+1)N+1)} \tag{D.2}$$

Writing out a few terms of this expression for the case of figure D.1, with ratio N is three, may give an understanding that this is indeed the correct expression. Choosing I_0 unity, and all I before are defined zero, gives at position 1 for the intensity $I_1 = R$, just as expected. At position 2, $I_2 = RI_1$, which equals, as expected, R^2. This goes on till the first transmitted ray comes back to the substrate-film interface. One expects an additional term, next to the power term, equal to the transmitted part squared, $(1-R)^2$, as the light had to transit the interface twice. Filling in the equation gives indeed

$$\begin{aligned} I_4 &= RI_3 + (1-R)^2 \sum_{i=0}^{\frac{3}{3}-1} R^i I_{3i} \\ &= R^4 + (1-R)^2 \end{aligned}$$

The term I_{3i} equals unity, as i equals zero.

To give more insight in this equation values are plotted in figure D.3. In this calculation the thickness of the film was taken 3 μm, with optical properties similar to Lu_2O_3:Eu^{3+}, the substrate was 250 μm thick, and had properties of Al_2O_3. The reflectivity is calculated with the Fresnel equations 2.27. The intensity I_0 is taken unity. The data displayed is for an angle of 50 degrees incidence in the film. With this settings the figure gives the part of the light 'located' in the film.

In the figure one sees periodically sharp peaks, these peaks correspond to multiples of distance d_2, see figure D.1. Every distance d_2 part of the light in the substrate is transmitted in the film, resulting in an increase of light in the film, thus in an increase of the part in the film.

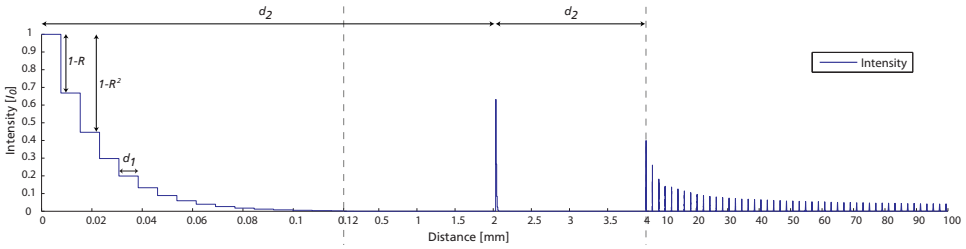

Figure D.2: Intensity in film plotted according equation D.2 as a function of distance. Thickness film is 3 μ**m, thickness substrate is** 250 μ**m. The refractive indices are** 1.9 **and** 1.5 **for respectively the film and the substrate. The data is plotted for an angle of incidence of** 50 **degrees on the film-substrate interface.**

The data given in figure D.2 is for one point source. In reality there are many more, giving rise to averaging out the sharp peaks. This is done in figure D.3. In this figure the mean intensity as function of size is plotted for different angles of incidence in the film of size of the LSC. Of course close to zero the intensity goes to unity, but for clarity this exponential drop in the first tenth of a millimeter has not been plotted. The behaviour of the mean intensity for changing angle for an LSC size of ten cm is displayed in the inset. One sees that at most a fraction of a percent of the light is located in the film.

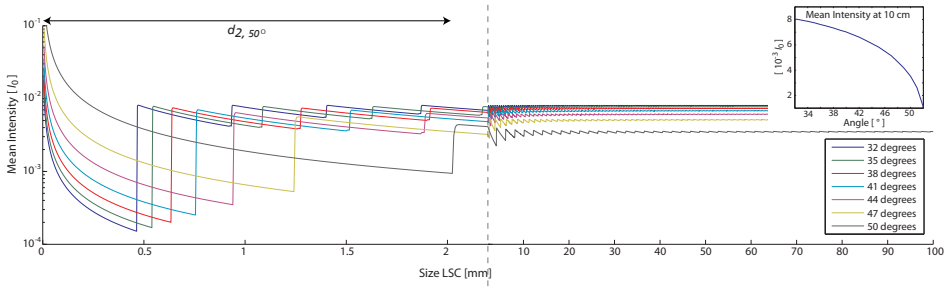

Figure D.3: Mean intensity in the film as function of size of the LSC. Plotted for different angles. Inset: Mean intensity as function of angle for a size of 10 **cm.**

Appendix E

3D directional output function

$I_{film}(\phi,\theta)$ = (1 / 4) * P0 * (1-cos(phi)^2 * n2^2 * sin(theta)^2 / n1^2)^(1 / 2) * (abs(sin(phi) * (n2^2 * sin(theta)^2 / n1^2)^(1 / 2) * (sin(phi) * n2^2 * sin(theta) * cos(theta) / ((n2^2 * sin(theta)^2 / n1^2)^(1 / 2) * (1-cos(phi)^2 * n2^2 * sin(theta)^2 / n1^2)^(1 / 2) * n1^2)+sin(phi) * (n2^2 * sin(theta)^2 / n1^2)^(1 / 2) * cos(phi)^2 * n2^2 * sin(theta) * cos(theta) / ((1-cos(phi)^2 * n2^2 * sin(theta)^2 / n1^2)^(3 / 2) * n1^2)) / ((1-cos(phi)^2 * n2^2 * sin(theta)^2 / n1^2)^(1 / 2) * (1-sin(phi)^2 * n2^2 * sin(theta)^2 / (n1^2 * (1-cos(phi)^2 * n2^2 * sin(theta)^2 / n1^2)))^(1 / 2)))+abs(cos(phi) * n2^2 * sin(theta) * cos(theta) * (cos(phi) * (n2^2 * sin(theta)^2 / n1^2)^(1 / 2) / (1-cos(phi)^2 * n2^2 * sin(theta)^2 / n1^2)^(1 / 2)-sin(phi)^2 * (n2^2 * sin(theta)^2 / n1^2)^(1 / 2) * cos(phi) * n2^2 * sin(theta)^2 / ((1-cos(phi)^2 * n2^2 * sin(theta)^2 / n1^2)^(3 / 2) * n1^2)) / ((n2^2 * sin(theta)^2 / n1^2)^(1 / 2) * n1^2 * (1-cos(phi)^2 * n2^2 * sin(theta)^2 / n1^2)^(1 / 2) * (1-sin(phi)^2 * n2^2 * sin(theta)^2 / (n1^2 * (1-cos(phi)^2 * n2^2 * sin(theta)^2 / n1^2)))^(1 / 2)))) / (Pi * sin(theta))

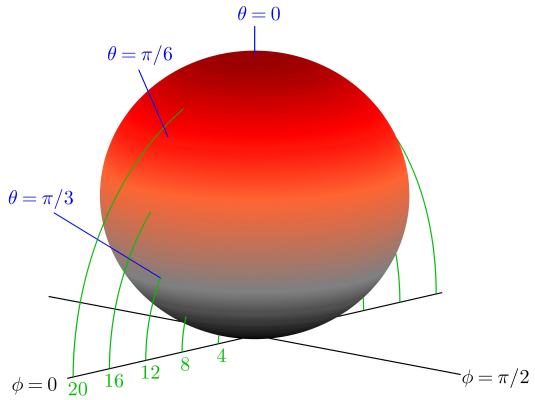

Figure E.1: The intensity emitted from the film as function of θ and ϕ

$I_{sub}(\phi, \theta)$ = (1 / 4) * P0 * n0 * (1-cos(phi)^2 * n2^2 * sin(theta)^2 / n0^2)^(1 / 2) * (abs(cos(phi) * n2^2 * sin(theta)^2 * sin(phi) * (sin(phi) * n2^2 * sin(theta) * cos(theta) / ((n2^2 * sin(theta)^2 / n0^2)^(1 / 2) * (1-cos(phi)^2 * n2^2 * sin(theta)^2 / n0^2)^(1 / 2) * n0^2)+sin(phi) * (n2^2 * sin(theta)^2 / n0^2)^(1 / 2) * cos(phi)^2 * n2^2 * sin(theta) * cos(theta) / ((1-cos(phi)^2 * n2^2 * sin(theta)^2 / n0^2)^(3 / 2) * n0^2)) / (n0 * n1 * (1-cos(phi)^2 * n2^2 * sin(theta)^2 / n0^2)^(1 / 2) * (1-n0^2 * (1-cos(phi)^2 * n2^2 * sin(theta)^2 / n0^2) / n1^2)^(1 / 2) * (1-sin(phi)^2 * n2^2 * sin(theta)^2 / (n0^2 * (1-cos(phi)^2 * n2^2 * sin(theta)^2 / n0^2)))^(1 / 2)))+abs(cos(phi)^2 * n2^2 * sin(theta) * cos(theta) * (cos(phi) * (n2^2 * sin(theta)^2 / n0^2)^(1 / 2) / (1-cos(phi)^2 * n2^2 * sin(theta)^2 / n0^2)^(1 / 2)-sin(phi)^2 * (n2^2 * sin(theta)^2 / n0^2)^(1 / 2) * cos(phi) * n2^2 * sin(theta)^2 / ((1-cos(phi)^2 * n2^2 * sin(theta)^2 / n0^2)^(3 / 2) * n0^2)) / (n0 * n1 * (1-cos(phi)^2 * n2^2 * sin(theta)^2 / n0^2)^(1 / 2) * (1-n0^2 * (1-cos(phi)^2 * n2^2 * sin(theta)^2 / n0^2) / n1^2)^(1 / 2) * (1-sin(phi)^2 * n2^2 * sin(theta)^2 / (n0^2 * (1-cos(phi)^2 * n2^2 * sin(theta)^2 / n0^2)))^(1 / 2)))) / (Pi * n1 * sin(theta))

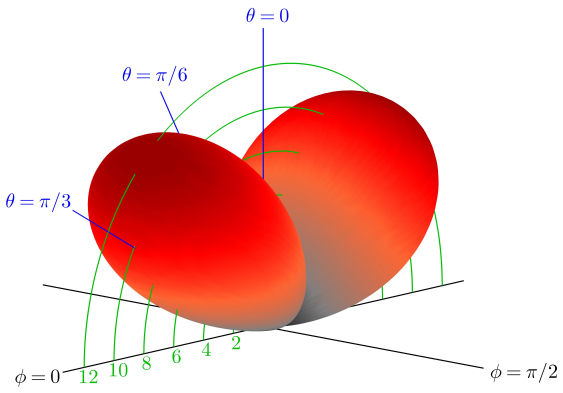

Figure E.2: The intensity emitted from the substrate as function of θ and ϕ

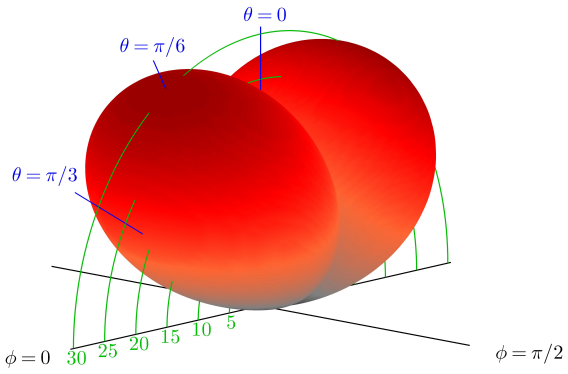

Figure E.3: The intensity emitted from the film and the substrate combined as function of θ and ϕ

Appendix F

Directional output fit

In this chapter both the equations for the ideal and the extended model are given. Both were given in a compact form in equations 2.53 and 2.56. The equations in the sections F.1 and F.2 are given in a form compatible with the mathematical program 'Maple'. Table F.1 shows the meaning of the parameters occuring in the fitting formulas given in this chapter.

Table F.1: Descriptions of the parameters in the directional output models.

Fitting parameters	**Description**
A	intensity factor of the substrate profile
B	intensity factor of the film profile
C	$\Delta\theta$ correcting for an offset in θ
mu1	$1/\tilde{\mu}_{sub}$
mu2	$1/\tilde{\mu}_{film}$

Known parameters	**Description**
n0	n_{sub}, refractive index substrate
n1	n_{film}, refractive index film
n2	n_{air}, refractive index air

F.1 Ideal model fit

$I_{ideal}\,(\phi = 0, \theta = x)$ = (1 / 4) * abs(A * n0 * (1-n2^2 * sin(x+C)^2 / n0^2)^(1 / 2) * abs(n2^2 * sin(x+C) * cos(x+C) * (n2^2 * sin(x+C)^2 / n0^2)^(1 / 2) / (n0 * n1 * (1-n2^2 * sin(x+C)^2 / n0^2) * (1-n0^2 * (1-n2^2 * sin(x+C)^2 / n0^2) / n1^2)^(1 / 2))) / (n1 * sin(x+C))) / Pi+(1 / 4) * abs(B * (1-n2^2 * sin(x+C)^2 / n1^2)^(1 / 2) * abs(n2^2 * sin(x+C) * cos(x+C) / (n1^2 * (1-n2^2 * sin(x+C)^2 / n1^2))) / sin(x+C)) / Pi

F.2 Extended model fit

$I_{ext}\left(\phi = 0, \theta = x\right)$ = (1 / 4) * abs(A * exp(-4.000000000 * mu1 / abs(n0 * (1-n2^2 * sin(x+C)^2 / n0^2)^(1 / 2) / (n2 * sin(x+C)))) * n0 * (1-n2^2 * sin(x+C)^2 / n0^2)^(1 / 2) * abs(n2^2 * sin(x+C) * cos(x+C) * (n2^2 * sin(x+C)^2 / n0^2)^(1 / 2) / (n0 * n1 * (1-n2^2 * sin(x+C)^2 / n0^2) * (1-n0^2 * (1-n2^2 * sin(x+C)^2 / n0^2) / n1^2)^(1 / 2))) * (2 * n0 * (1-n2^2 * sin(x+C)^2 / n0^2)^(1 / 2) * n2 * cos(x+C) / (n2 * cos(x+C)+n0 * (1-n2^2 * sin(x+C)^2 / n0^2)^(1 / 2))^2+2 * n0 * (1-n2^2 * sin(x+C)^2 / n0^2)^(1 / 2) * n2 * cos(x+C) / (n0 * cos(x+C)+n2 * (1-n2^2 * sin(x+C)^2 / n0^2)^(1 / 2))^2) / (n1 * sin(x+C))) / Pi+(1 / 4) * abs(B * exp(-166.6666667 * mu2 / abs(n1 * (1-n2^2 * sin(x+C)^2 / n1^2)^(1 / 2) / (n2 * sin(x+C)))) * (1-n2^2 * sin(x+C)^2 / n1^2)^(1 / 2) * abs(n2^2 * sin(x+C) * cos(x+C) / (n1^2 * (1-n2^2 * sin(x+C)^2 / n1^2))) * (2 * n1 * (1-n2^2 * sin(x+C)^2 / n1^2)^(1 / 2) * n2 * cos(x+C) / (n2 * cos(x+C)+n1 * (1-n2^2 * sin(x+C)^2 / n1^2)^(1 / 2))^2+2 * n1 * (1-n2^2 * sin(x+C)^2 / n1^2)^(1 / 2) * n2 * cos(x+C) / (n1 * cos(x+C)+n2 * (1-n2^2 * sin(x+C)^2 / n1^2)^(1 / 2))^2) / sin(x+C)) / Pi